RELATIVE PERMEABILITY OF OIL-WATER SYSTEMS IN FRACTURES

A Dissertation

by

DANTE RENE GUERRA

Submitted to the Office of Graduate and Professional Studies of
Texas A&M University
in partial fulfillment of the requirements for the degree of

DOCTOR OF PHILOSOPHY

Chair of Committee,	Ding Zhu
Committee Members,	A. Daniel Hill
	Michael Pope
	Kan Wu
Head of Department,	A. Daniel Hill

December 2017

Major Subject: Petroleum Engineering

ABSTRACT

The objective of this study was to develop an understanding of the relative permeability of oil-water systems in fractures. Presently, two-phase flow behavior through propped and unpropped fractures is poorly understood, and due to this fact, reservoir modeling using numerical simulation for the domain that contains fractures typically makes use of straight-line relative permeability and zero capillary pressure in the fractures; however there have been several studies demonstrating that both viscous and capillary-dominated flow can be expected in naturally fractured reservoirs, where non-linear fracture relative permeabilities must be used to accurately model these reservoirs.

The experimental measurements conducted in this study were done using downhole core from the Wolfcamp Shale formation in the Permian Basin. The core sections used for this study consisted of two-thirds slabbed, four inch diameter core. Test specimens were then cut from each core specimen and subsequently fractured or saw cut to generate a fracture along each sample. The samples were then conditioned in formation oil at reservoir temperature for 30 days prior to any testing.

The oil-water relative permeability was measured following the steady state method. Formation oil and reconstituted brine with and without surfactants were used as the test fluids. All measurements were conducted at reservoir temperature and at representative effective fracture closure stress. Instantaneous measurements of pressure, flow rate and density were recorded throughout the entire duration of each experiment. Fluid saturations within the fracture were calculated using the mass continuity equation.

The data from the experimental measurements was analyzed using Darcy's law, and a clear relationship between relative permeability and saturation was observed. The calculated relative permeability curves closely follow the generalized Brooks-Corey correlation for oil-water systems. Furthermore, there was a significant difference in the relative permeability curves between the oil-water only systems and the oil-water-surfactant systems.

The calculated relative permeability curves were then used as inputs to a numerical simulation model constructed in Eclipse Reservoir Simulator from Schlumberger. The domain represents a small symmetry section within a stimulated reservoir volume of a hydraulically fractured well consisting of 450 cubic feet containing a natural fracture joint set as well as a propped hydraulic fracture section.

Results from the numerical simulation indicate the potential for surfactant additives to significantly improve initial oil production rates as well as 500 day cumulative oil production by as much as 36% and 16% respectively.

DEDICATION

"The heights by great men reached and kept

Were not attained by sudden flight,

But they, while their companions slept,

Were toiling upward in the night."

- Henry Wadsworth Longfellow

I would like to dedicate this work to my parents, Juan Carlos Guerra and Dana Marie Tierney, and to my brother Jesse Guerra. This and all my academic achievements would never have been possible without their great many sacrifices in raising me. Their hard work, continued support, and unconditional love built the foundation for the person I have become today.

Obtaining my Ph.D. had always been a lifelong dream of mine, and even though there have been several years at a time that I was away from my family during this odyssey, I always felt like they were there by my side.

ACKNOWLEDGEMENTS

I would like to express my deepest gratitude to Dr. Ding Zhu and Dr. A. Daniel Hill for giving me the opportunity to join their research group. I feel honored to have learned so much from both Dr. Zhu and Dr. Hill, in and out of the classroom, and I am sure I will continue to learn from them in the future.

I would like to thank Dr. Kan Wu for all the discussions regarding my research and incorporating the findings with numerical simulation of naturally fractured reservoirs, and I look forward to continuing those conversations.

I would also like to thank Dr. Michael Pope for serving as member on my committee. I learned a great deal from Dr. Pope and built many lasting memories during multiple field trips to collect outcrop samples.

I would like to give a special appreciation to both Jesse Guerra and Ryan Winner for their timely support during trying times in and out of the laboratory. I would also like to thank the other members of the fracture conductivity research group that I had the pleasure of working with: Cody Kainer, Ashley Knorr, Omar Enriquez Tenorio, Bill Foran, Mark McGinley, Paola Perez, Tim Jansen, James Guzek, Kathryn Briggs, and Junjing Zhang.

I would also like to thank John Maldonado, Sr., and Don Conlee for their indispensable help in locating, installing, and calibrating all the laboratory instrumentation and equipment.

I would like to extend a special acknowledgement to my team in Corporate Engineering at Pioneer Natural Resources. Specifically Anthony Quinn for his help and guidance in using Eclipse Reservoir Simulator and reminding me that the purpose of computing is insight, not numbers. I would like to thank Paul Leonard for all his continued guidance and mentorship and for reminding me that it's not just about getting something right, but getting it right and on time. I would like to thank Gary Schein for all his guidance on fracturing fluid additives and their role in enhanced oil recovery. Last but not least, I would like to thank Perry Richmond for all the late evening conversations which have inspired a great many ideas.

CONTRIBUTORS AND FUNDING SOURCES

Contributors

This work was supervised by a dissertation committee consisting of Professor Ding Zhu, primary advisor, Professor A. Daniel Hill, co-advisor, and Professor Kan Wu of the Harold Vance Department of Petroleum Engineering; and Professor Michael Pope of Department of Geology and Geophysics.

The data analyzed for Section 2.3.3 was provided by student Kan Han Park under the supervision of Professor David Schechter of the Harold Vance Department of Petroleum Engineering.

The work described in Section 2 was completed by the student, in collaboration with student Ryan Winner of the Harold Vance Department of Petroleum Engineering.

All other work conducted for the dissertation was completed by the student independently.

Funding Sources

Graduate study was supported in part by a graduate research assistantship from Texas A&M University.

This work was made possible in part by Pioneer Natural Resources under TEES project number 28-406990-00001. Its contents are solely the responsibility of the authors and do not necessarily represent the official views of Pioneer Natural Resources.

NOMENCLATURE

t	Time, t, (min)
T	Temperature, °C
μ	Fluid viscosity, $ML^{-1}t^{-1}$, cP
ρ	Fluid density, ML^{-3}, (g/cm^3)
L_c	Core length, L, (cm)
w_f	Fracture width, L, (cm)
a_f	Fracture aperture, L, (cm)
A_f	Fracture cross-sectional area, L^2, (cm^2)
P	Pressure, $ML^{-1}t^{-2}$, (psig)
ΔP_{ss}	Differential pressure at steady state, $ML^{-1}t^{-2}$, (psig)
F_o	Oil fraction, fraction
F_w	Water fraction, fraction
S_w	Water saturation, fraction
S_{wi}	Initial water saturation, fraction
S_{wcr}	Critical water saturation, fraction
S_{wirr}	Irreducible water saturation, fraction
S_{orw}	Residual oil saturation to water, fraction
$\dot{m}$	Mass flow rate, Mt^{-1}, (g/min)
Q	Volumetric flow rate, L^3t^{-1}, (mL/min)

C_o	Corey exponent for oil
C_w	Corey exponent for water
k	Absolute permeability, L^2, (md)
k	Absolute permeability, L^2, (md)
k_{eo}	Effective permeability to oil, L^2, (md)
k_{ew}	Effective permeability to water, L^2, (md)
k_{ro}	Relative permeability to oil, fraction
k_{rw}	Relative permeability to water, fraction

TABLE OF CONTENTS

Page

LIST OF FIGURES

Page

LIST OF TABLES

Page

1. INTRODUCTION

1.1 Background

Permeability is the property that describes the ability for fluids to flow in a porous medium. The concept of permeability was introduced by Darcy (1856). The publication by Darcy is a classic experimental work from which both petroleum engineering and ground water hydrology have benefited greatly as stated by Economides et al. (2012). Darcy determined that the flow rate of a fluid was linearly proportional to the cross-sectional area of the porous medium through which the fluid passes, as well as linearly proportional to the pressure differential divided by the length of the porous medium (the hydraulic gradient), and inversely proportional to the fluid viscosity. This relationship is called Darcy's Law:

$$Q = -(kA)\left(\frac{\Delta P}{L}\right)\left(\frac{1}{\mu}\right) = -\frac{kA\Delta P}{\mu L} \quad \text{.....(1-1)}$$

In the above equation, the constant (k) that satisfies the equality of the relationship is defined as permeability in the petroleum industry.

When describing multiphase flow in porous media, the relative permeability (k_r) of a phase is a dimensionless ratio of the effective permeability (k_e) of that phase to the absolute permeability (k) of the porous media:

$$k_r = \frac{k_e}{k} \quad \text{.....(1-2)}$$

By definition, the sum of the relative permeabilities of each phase in a two phase system will be smaller or equal to one. When the sum of the relative permeabilities is equal

to one, a straight line relative permeability curve (also referred to as a stick curve, or X-curve) is obtained, indicating a linear relationship of the relative permeability with respect to phase saturation as well as no flow interference between phases. Alternatively, if the sum of the relative permeabilities is less than one, this indicates there is flow interference between the phases and the resulting relative permeability curve will not have a linear relationship with respect to fluid saturations.

Although relative permeability in porous media has been well studied, there is limited published work investigating the relative permeability in fractures, and presently, two-phase flow behavior through propped and unpropped fractures is poorly understood.

Reservoir modeling using numerical simulation for the physical system that contains fractures typically makes use of straight-line relative permeability and zero capillary pressure in the fractures. This straight-line relative permeability curve approach originated with a publication by Romm (1966). His findings were based on the experiments of flow between two parallel glass plates, which showed a linear dependence between phase relative permeability and phase saturation, as well as zero capillary pressure. The experiments did not examine the effects of fracture aperture and roughness. Rossen and Kumar (1992) demonstrated that both viscous and capillary-dominated flow can be expected in naturally fractured reservoirs, where non-linear fracture relative permeabilities must be used in order to accurately model these reservoirs. Furthermore, de la Porte et al. (2005) showed that using straight-line relative permeabilities can lead to predicted oil-recovery errors as high as 70% in oil-water systems and to underestimation of oil production times in some gas-oil systems by as much as a factor of three.

The studies demonstrated that both viscous and capillary-dominated flow can be expected in naturally fractured reservoirs, indicating that non-linear fracture relative permeabilities must be used to accurately model these reservoirs.

1.2 Literature Review

This section presents a literature review of a body of work that was compiled related to the nature of relative permeability measurements, and more specifically to the measurement of relative permeability behavior in fractures. This includes the background information on classical relative permeability measurements, the different methods available for its measurement, and the evolution of the applications of these measurement methods to determine relative permeability behavior in fractures.

The relative permeability of porous media has been widely studied and detailed procedures on the measurement techniques have been published. There are two widely accepted relative permeability measurement methods, namely the steady state method and the unsteady state method as described by Abaci et al. (1992), Glover (2010), Honarpour and Mahmood (1988), Johnson et al. (1959), and Richardson et al. (1952).

1.2.1 Unsteady State Relative Permeability

Laboratory measurements of relative permeability that are made by displacing one phase by another are called unsteady state tests. The specific measurement procedure for unsteady state tests as well as the calculation of the parameters required to generate the relative permeability curves was presented by Glover (2010).

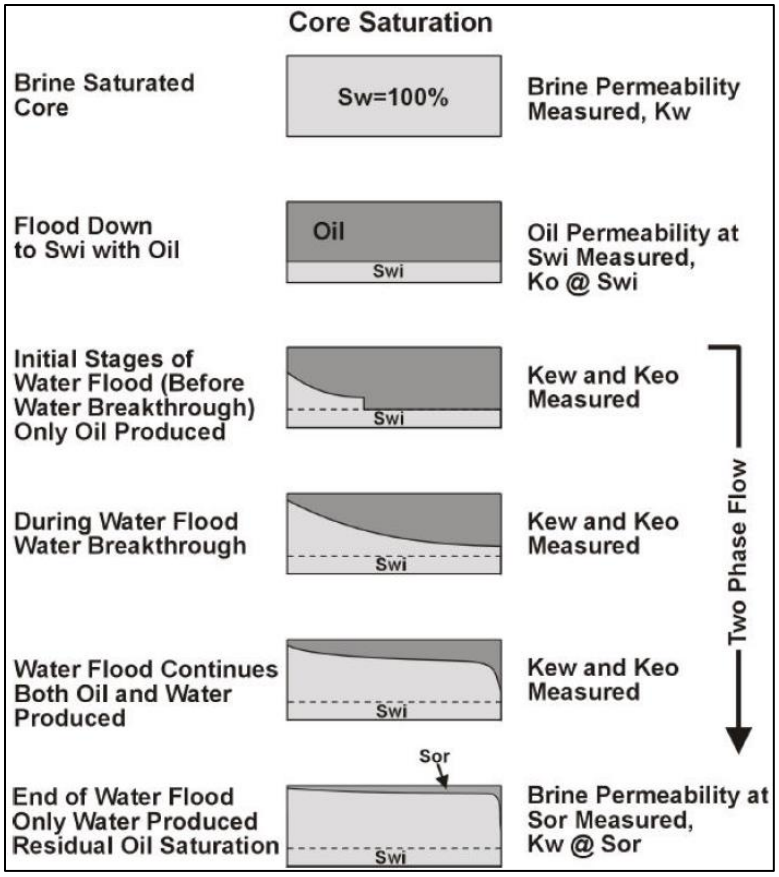

Fig. 1.1 – Unsteady State Relative Permeability Waterflood Procedure Reprinted from Glover (2010).

The general measurement procedure for conducting unsteady state relative permeability measurements as illustrated in **Fig. 1.1** is as follows:

1. Age fractured core in formation oil
2. Flood core with brine, measure k_w at $S_w = 1$.
3. Inject oil and flood down to S_{wirr} at suitable differential pressure.
4. Measure k_o at S_{wirr}.
5. Carry out waterflood, recording pressure differential, incremental oil production, and water production.

6. Use the equations from Johnson, Bossler & Naumann (JBN analysis) to calculate k_{eo}, k_{ew}, k_{ro}, and k_{rw} for various S_{wout} and S_{wav}.
7. Measure k_{ew}, and calculate k_{rw} at S_{or}.

Once an unsteady state relative permeability test has been carried out, the calculation of the relative permeability for this method is done using the procedure described by Johnson, Bossler and Naumann published by Johnson et al. (1959), and is commonly referred to as the JBN analysis.

The data required for the application of the JBN analysis generally recorded from the experimental measurements as described in Glover (2010) includes the quantity of displacing phase injected (Q_i), pressure differential (ΔP), pressure differential at initial conditions (ΔP_i), volume of oil produced (Q_o), volume of water produced (Q_w), oil viscosity (μ_o), and water viscosity (μ_w).

The JBN analysis consists of three calculation stages. The first stage is to determine the ratio of the relative permeability to oil (k_{ro}) with respect to the relative permeability to water (k_{rw}).

In order to determine this ratio (k_{ro}/k_{rw}), the average water saturation (S_{wav}) is plotted against the quantity of displacing fluid injected (Q_i). The inflection point on this plot indicates the moment of water breakthrough. It can also be shown that the fractional flow of oil at the core outlet is given by:

$$f_{o,out} = \frac{dS_{wav}}{dQ_i} \quad \text{.....(1-3)}$$

Together with:

$$f_{o,out} = \frac{1}{1+\left(\frac{k_{rw}\mu_o}{k_{ro}\mu_w}\right)} \quad \text{.....(1-4)}$$

With these two expressions and all quantities known from the recorded experiment data, the ratio k_{ro}/k_{rw} is solved for from **Eq. 1-3** and **Eq. 1-4**.

The second stage of calculation is to determine the relative permeability to oil (k_{ro}). For this purpose, the ratio ($\Delta P/\Delta P_i$) of the instantaneous pressure differential with respect to the pressure differential at initial conditions is plotted against the quantity of displacing phase injected (Q_i). This plot is used to calculate the injectivity ratio (I_R), which is given by:

$$I_R = \frac{\Delta P_i}{\Delta P}\frac{1}{Q_i} \quad \text{.....(1-5)}$$

Using the expression for the injectivity ratio, a plot is then created by plotting the inverse of the product of the quantity of displacing fluid injected and the injectivity ratio ($1/Q_i\, I_R$) against the inverse of the quantity of displacing fluid injected ($1/Q_i$). It can then be shown that:

$$k_{ro} = f_{o,out}\frac{1}{\frac{d(1/Q_i I_R)}{d(1/Q_i)}} \quad \text{.....(1-6)}$$

Once the relative permeability to oil has been determined from (**Eq. 1-3**, **Eq. 1-4**), then (k_{rw}) can easily be determined. Finally, the correction presented by Welge (1952) is used to convert average saturations to outlet face saturations:

$$S_{w,out} = S_{wav} - f_{o,out}Q_i \quad \text{.....(1-7)}$$

Now, the normal relative permeability curve can be generated by plotting each phase relative permeability as a function of the outlet face saturation as shown in **Fig. 1.2**.

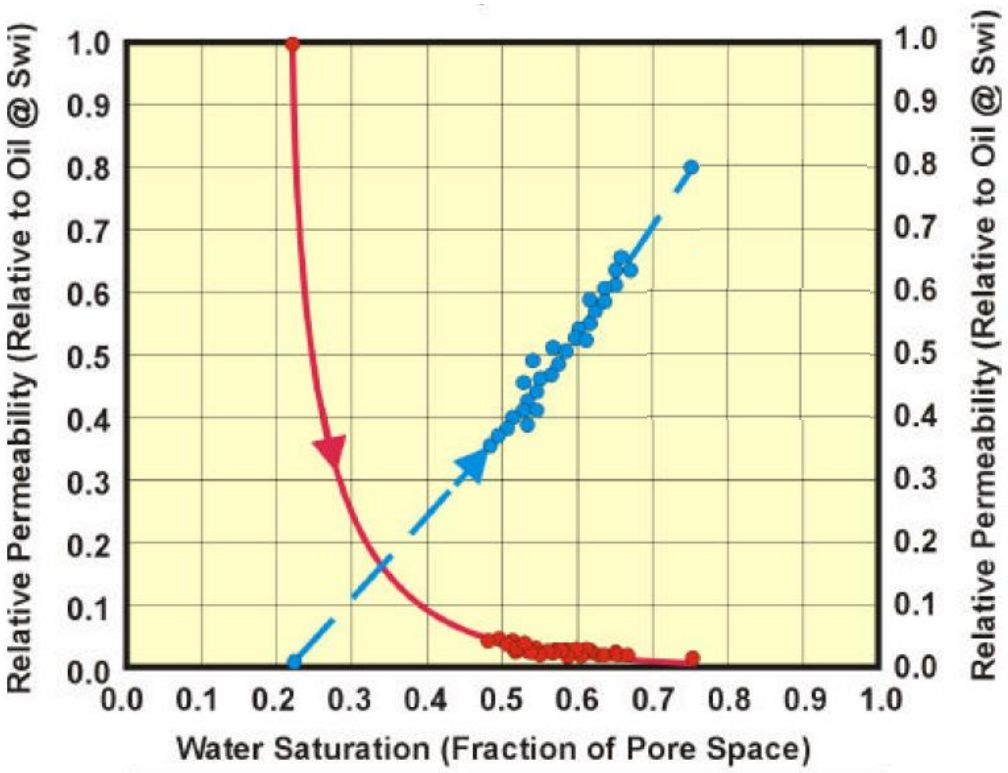

Fig. 1.2 – Unsteady State Oil-Water Relative Permeability Low Rate Flood Example for an Oil-Wet Core Reprinted from Glover (2010).

It is important to note several key advantages of using the steady state relative permeability measurement method, which include the ability of this method to obtain even saturations of each fluid present, much shorter time required to complete the experiment when compared to the steady state method, and there is no need to scan the core to obtain in-situ saturations. It is also important to note that the unsteady state method presents some noteworthy disadvantages, which include the need to estimate the average water saturation rather than directly measure it, which might lead to significant errors, and the inability to fully define the shape of the relative permeability curve as shown in **Fig. 1.2**.

1.2.2 Steady State Relative Permeability

Laboratory measurements of relative permeability using the steady state method differ from the unsteady state method in that oil and brine are flowed simultaneously through the test medium at a fixed ratio until there is no change in the measurements of pressure and outlet fractional flow rates with respect to time, as described in work done by Glover (2010). The specific measurement procedure for steady state tests as well as the calculation of the parameters required to generate the relative permeability curves is outlined in this subsection. **Fig. 1.3** shows the flow chart of the steady state method for relative permeability measurement.

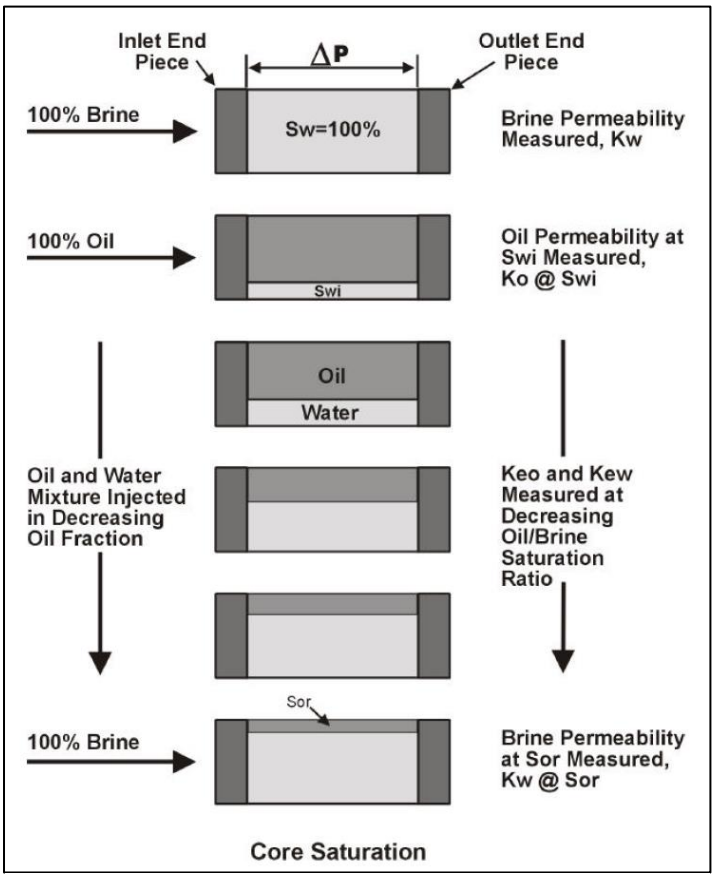

Fig. 1.3 – Steady State Relative Permeability Waterflood Procedure Reprinted from Glover (2010).

The measurement procedure for conducting steady state relative permeability measurements as illustrated in **Fig. 1.3** is as follows:

1. Condition fractured core in formation oil
2. Flood core with brine, measure k_o at $S_w = 1$.
3. Inject oil and flood down to S_{wirr} at suitable differential pressure.
4. Measure k_{eo} at S_{wirr}.
5. Begin flowing oil and brine at fixed ratios until a constant ΔP is obtained at each ratio.
6. Repeat step 5 with various oil/brine ratios (increasing S_w).
7. Inject brine and flood down to S_{or}.
8. Calculate effective permeabilities using Darcy's Law.

The work done by Muskat et al. (1937) under the assumption that Darcy's Law is valid for each fluid, showed that the volumetric flow rate (Q) for each respective phase can be written as:

$$Q_i = \frac{k\, k_{ri}\, A\, \Delta P_i}{\mu_i\, L} \quad \text{.....(1-8)}$$

where (Q_i) is the oil or water volumetric flow rate, (k) is the absolute permeability, (k_{ri}) is the oil or water relative permeability, (A) is the flow cross-sectional area, (ΔP_i) is the differential pressure, (μ_i) is the water or oil viscosity, and (L) is the length of the medium through which the flow is occurring. The phase saturations must then be determined for each steady state measurement (each injected phase ratio). The determination of the phase saturations can be very difficult; however, there are several methods that have proven to be successful for monitoring the saturations during the

steady state experiments as described by Glover (2010). These methods include Gamma Attenuation Saturation Monitoring (GASM), X-Radiometry, CT Scanning, and NMR Scanning.

The steady state tests have the advantage that a more complete relative permeability curve can be generated when compared to the unsteady state method with measurements being possible across a wider range of saturations as shown in **Fig. 1.4**. Furthermore, the steady state method is considered the most accurate test available, and it can be applied to any saturation ratios. The main disadvantage of this method is the length of time required for each flow ratio to equilibrate and to reach steady state, along with the need to determine saturations via advanced and often costly methods.

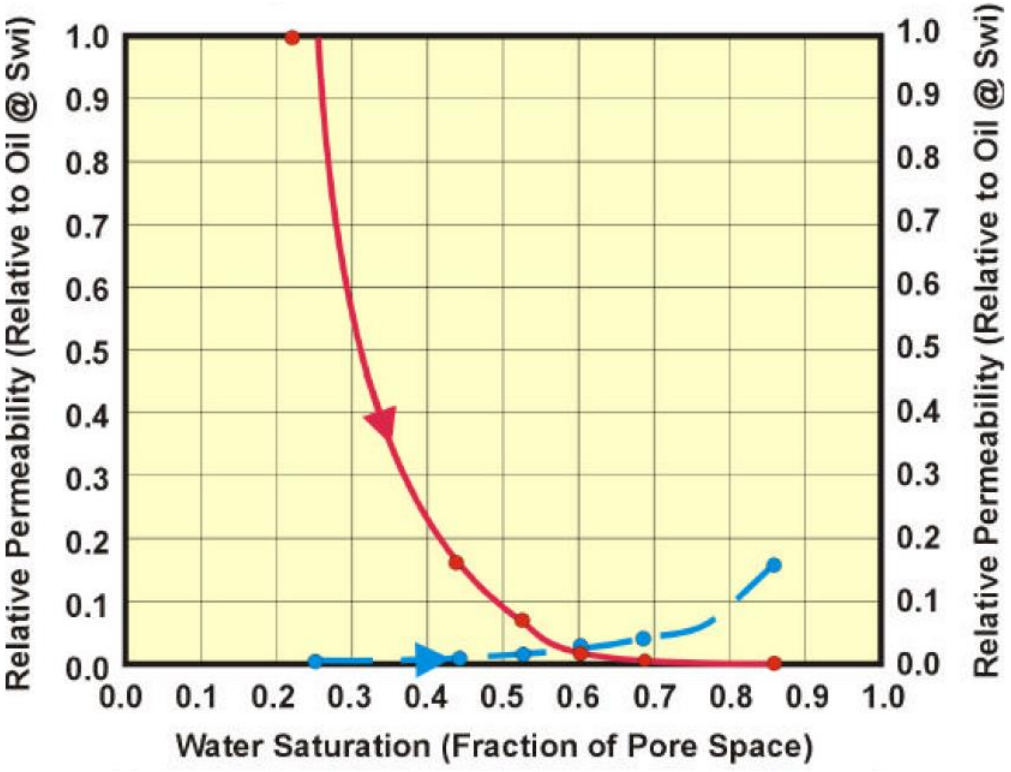

Fig. 1.4 – Steady State Water-Oil Relative Permeability Example for an Intermediate-Wet Core Reprinted from Glover (2010).

1.2.3 Relative Permeability Measurements in Fractures

The experiments conducted by Romm (1966) is the first published laboratory investigation of multiphase flow in a single fracture. In this study, artificial parallel-plate fractures were used to flow water and kerosene and the relative permeability of each phase was calculated. Results indicated a linear dependence of permeability on saturation.

Pieters and Graves (1994) repeated Romm's experiment using the same fluids, however, they used a high resolution camera to record the fluid saturations behind a glass plate. They determined that there is in fact a non-straight line relative permeability behavior and highlighted the importance of accurately representing the fluid saturations.

There have been several experimental studies demonstrating the non-straight line relative permeability behavior in fractures represented by parallel plates as described in work conducted by Diomampo et al. (2001), Pan et al. (1996) and Diomampo et al. (2001); Pan et al. (1996); Speyer et al. (2007). Further studies have attempted to measure fracture relative permeability, however, these studies by Huo and Benson (2016) and Izadi et al. (2012) use synthetic fluids at room temperature, and create the fracture by means of a saw cut.

The most realistic study conducted to date used a 2" core, with an induced fracture. However, decane and water were used as the test fluids, and the test was conducted at room temperature. They found a straight line relationship at high fracture apertures, and close agreement to the Corey model at very small apertures and high closure stress as described in work done by Sakurai et al. (2013).

The importance of using reservoir fluids at reservoir conditions was outlined by Mungan (1972). He demonstrated the differences in relative permeability of a matrix between synthetic fluids and actual reservoir fluids.

There is a vast number of studies that present analytically and simulation-derived models to approximate the relative permeability behavior in fractures as a function of fracture dimensions, surface roughness, and fluid properties; however, these models have not been verified with experimental data as described in work by Aguilera (1982), Akin (2001), de la Porte et al. (2005), Gilman and Kazemi (1983), Kasiri (2011), Morris and Pyrak-Nolte (1999), Rossen and Kumar (1992), and Aguilera (1982); Akin (2001); de la

Porte et al. (2005); Gilman and Kazemi (1983); Kasiri (2011); Morris and Pyrak-Nolte (1999); Rossen and Kumar (1992); Tsang (1989).

Romm's linear relationship has been widely accepted by petroleum engineers and is still widely used in the simulation of fractured reservoirs to this present day as stated in publications by Gilman and Kazemi (1983), and Kasiri (2011).

1.3 Objective

The objective of this study is to experimentally measure the fracture relative permeability behavior of the Wolfcamp core under representative reservoir temperature and effective fracture closure stress, as well as using actual reservoir fluids (formation brine, formation oil, and surfactant laden fracturing fluid). The effect of wettability alteration and interfacial tension reduction on the resulting relative permeability of fractures is also investigated. The main goal is to build a better understanding of two phase (oil-water) flow within fractures and apply it to reservoir simulation of fractured reservoirs.

2. EXPERIMENTAL DESIGN

2.1 Introduction

This section presents a description of the downhole core test samples, test fluids (formation oil, reconstituted brine, and surfactant additives), experimental equipment and laboratory procedure used for the experimental measurements to calculate the oil-water relative permeability in fractures.

All tests were done at representative reservoir conditions (effective fracture closure stress and representative reservoir temperature) using the steady state relative permeability measurement method.

2.2 Shale Test Samples

A downhole core section provided by Pioneer Natural Resources was used for all tests. The 4 in. diameter cores as received had been slabbed at 2/3 of the diameter, and spans a length of 38 ft. ranging in depth from 9612 – 9650 ft. (TVD). The core section lies within the Wolfcamp Shale Formation.

Given the state of the cores, the intact sections suitable for test specimen cutting had to be selected. Intervals having an intact length greater than 6 in. were selected. The subsections of the core selected for the test sample cutting along with their corresponding depth are listed in **Table 2.1** and graphically plotted in **Fig. 2.1**.

Table 2.1 – Wolfcamp Core Data Summary.

Core Details				Sample Details					
Core No.	Box No.	Top Depth (ft)	Bottom Depth (ft)	Sample No.	Max Length (in)	Top Depth (ft)	Bottom Depth (ft)	Mean Depth (ft)	(+/-) (ft)
1	60/109	9612.30	9614.00	1	7.50	9612.30	9612.93	9612.61	0.31
1	61/109	9614.00	9616.00	2	7.50	9615.38	9616.00	9615.69	0.31
1	67/109	9638.00	9640.00	3	7.50	9624.65	9625.15	9624.90	0.25
1	67/109	9624.00	9626.00	4	7.50	9625.15	9625.77	9625.46	0.31
1	71/109	9631.30	9632.30	5	7.00	9633.45	9634.03	9633.74	0.29
1	74/109	9636.00	9638.00	6	7.00	9636.48	9637.01	9636.74	0.26
1	77/109	9640.97	9641.97	7	6.50	9641.43	9641.97	9641.70	0.27
1	79/109	9644.00	9646.00	8	6.25	9644.00	9644.52	9644.26	0.26
1	80/109	9646.00	9648.00	9	7.00	9646.00	9646.58	9646.29	0.29
1	82/109	9650.00	9650.94	10	7.50	9650.00	9650.63	9650.31	0.31

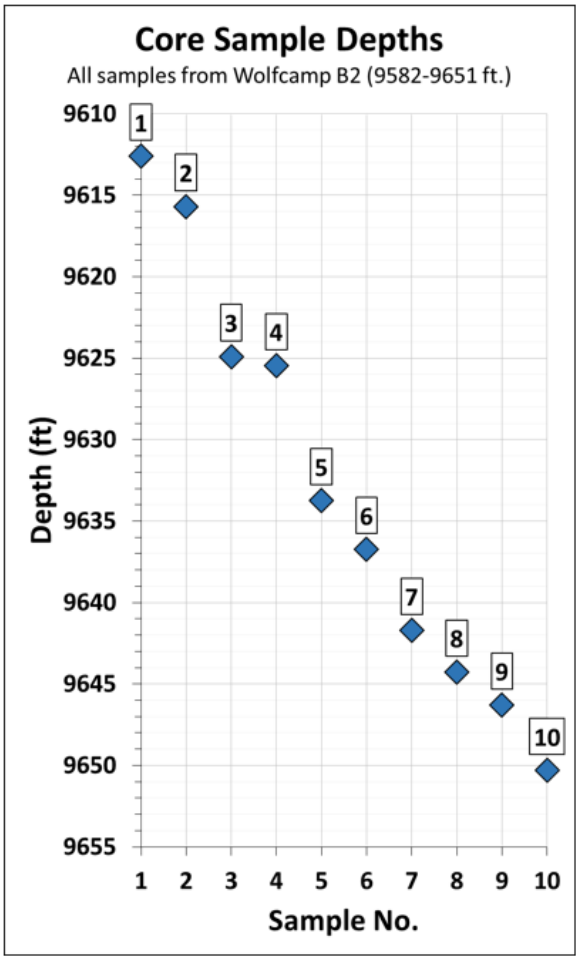

Fig. 2.1 – Wolfcamp Core Sample Depths (TVD).

2.2.1 Sample Mineralogy

The mineral content of each core interval selected for test specimen cutting was measured in order to classify each test sample.

A rather large sample (50 cm^3) from each depth interval was crushed, powdered, and sieved to a maximum particle size of 90 micrometers. The samples were taken from the carcass of the plugged core and captured several laminations in order to have a representative mineralogy for each depth interval.

The powdered samples were then tested using a BRUKER D8 ADVANCE Eco XRD. The results from the mineralogy testing corresponding to each test sample are listed in **Table 2.2**, and graphically presented in **Fig. 2.2**.

Table 2.2 – X-Ray Diffraction Mineral Data for Wolfcamp Core Samples.

		X-Ray Diffraction Mineral Data									
	Sample Number	1	2	3	4	5	6	7	8	9	10
	Sample Depth (ft)	9612.61	9615.69	9624.90	9625.46	9633.74	9636.74	9641.70	9644.26	9646.29	9650.31
Component %	Quartz	39.8	50.9	65.9	65.0	71.7	31.0	9.2	67.3	51.0	60.0
	Plagioclase/Oligoclase	13.7	33.6	14.4	16.7	12.8	13.1	13.8	15.1	14.6	11.4
	K-Feldspar	-	-	-	-	-	-	-	14.0	29.9	25.0
	Calcite	18.8	0.3	0.5	-	-	8.3	9.3	-	-	-
	Dolomite	21.0	3.3	2.7	1.6	1.6	38.4	65.3	1.9	1.4	1.5
	Pyrite	1.7	2.5	1.7	1.2	0.9	1.1	2.5	1.8	3.2	2.1
	Illite+Mica	4.7	9.5	14.8	15.6	13.0	8.2	-	-	-	-
	Smectite	0.3	-	-	-	-	-	-	-	-	-
	Totals	100.0	100.0	100.0	100.0	100.0	100.0	100.0	100.0	100.0	100.0

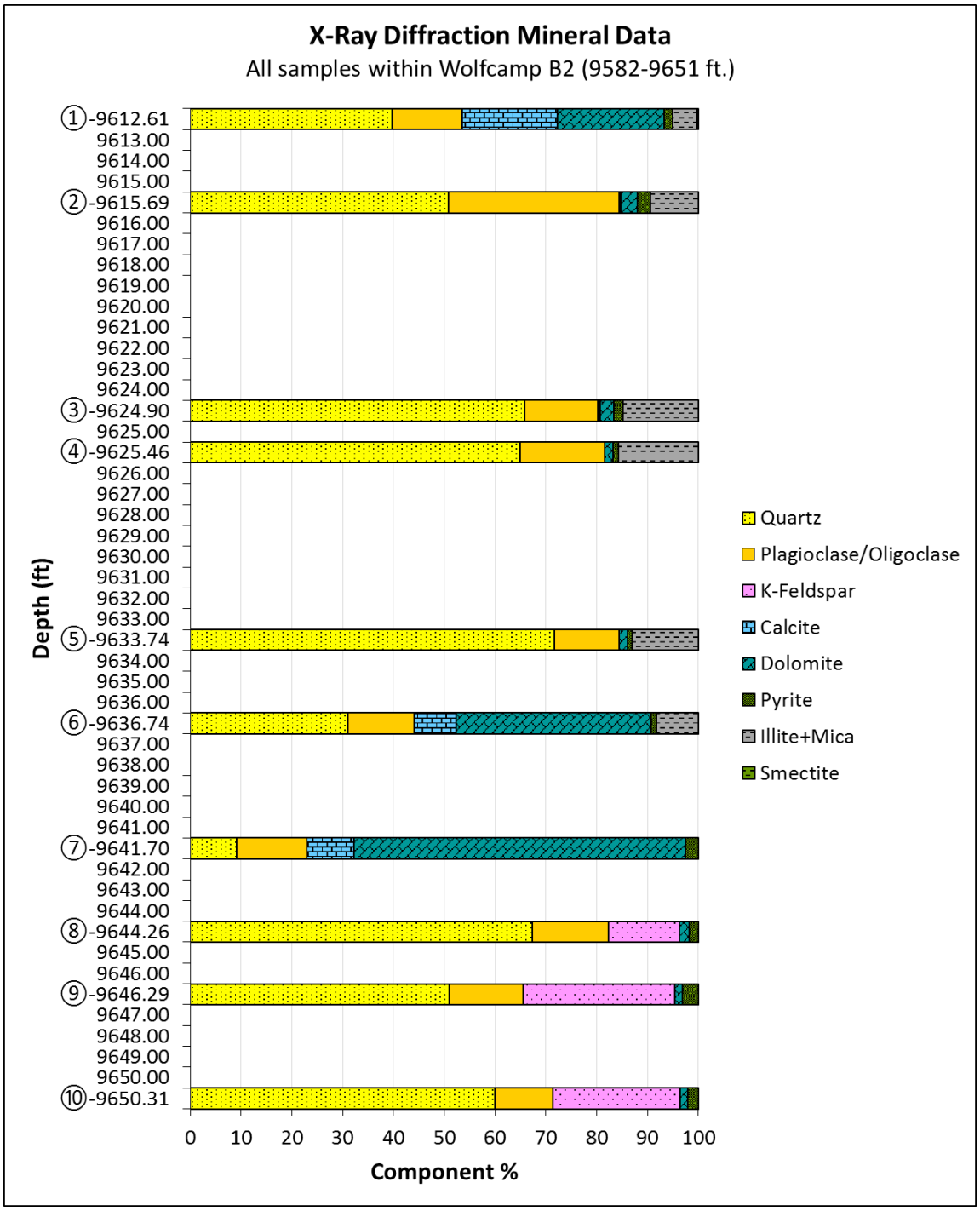

Fig. 2.2 – X-Ray Diffraction Mineral Data for Wolfcamp Core Samples Plotted by Depth (TVD).

2.2.2 Sample Preparation

The downhole core as received had been slabbed at 2/3 diameter. Each subsection of the slabbed core was cut into five test samples consisting of three small core plugs (1 in. diameter by 2 in. length) for contact angle measurements, and two large core plugs (1.5 in. diameter by 6 in. length) for oil-water relative permeability testing after fracturing. A drawing depicting the geometry of the as received slabbed core and resulting core plugs is depicted in **Fig. 2.3**.

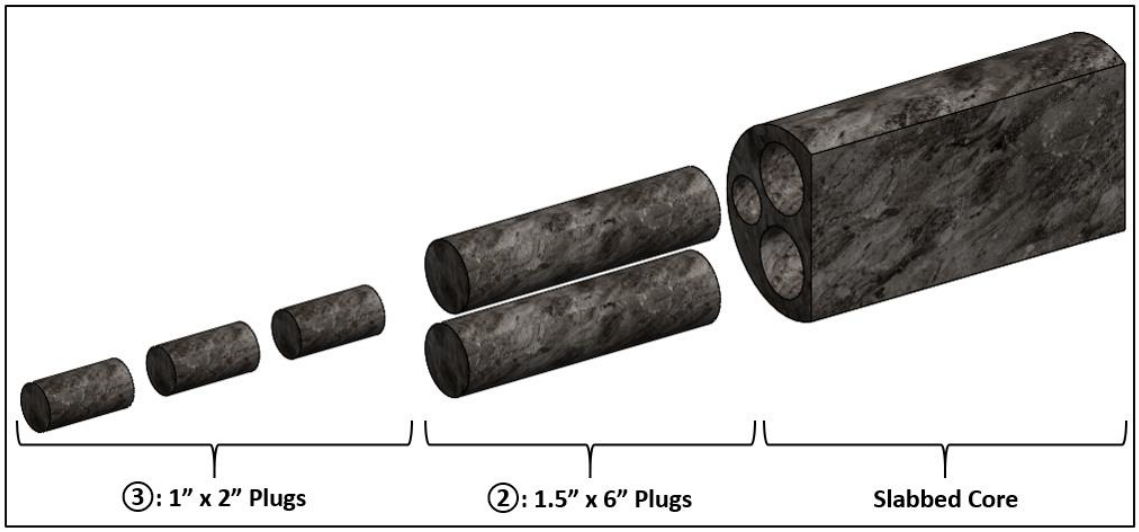

Fig. 2.3 – Drawing of Sample Test Specimen Cutting from Slabbed Core Section.

Two large core plugs were cut from each downhole core subsection in order to create a fracture via indirect tension loading, and in the event the core material was too fragile to create a uniform fracture along the length of the core, the second plug was then saw cut in order to create an artificial fracture for oil-water relative permeability testing.

2.2.2.1 Fractured Samples

Fracturing of one large core plug from each core interval was attempted. Fracturing of the core plugs was done using a modified indirect tension test fixture designed and manufactured specifically for the 1.5 in. by 6 in. diameter sample dimensions. The design of the special loading fixture was inspired by a study on optimal loading jaw geometry published by Erarslan and Williams (2012), as shown in **Fig. 2.4**.

Fig. 2.4 – Test Specimen Being Fractured by Means of Indirect Tension in a GCTS Hydraulic Load Frame.

The load frame used to fracture the samples is a GCTS FRM4-10000-50S four column vertical standing frame. The load frame has a 1,000 kN static compression load capacity and a 800 kN dynamic load capacity. The loading piston has a maximum stroke length of 5 mm and the maximum piston velocity is 80 mm per minute. A loading rate of 0.5 kN per minute was used to fracture the test samples.

Each sample was placed within a heat shrink sleeve to confine the fractured halves and any material generated during the fracturing process. The samples are then pre-loaded within the indirect tension test fixture loading jaws, then subsequently measured to ensure the sample was centered and parallel with respect to the loading jaws.

Once the sample was installed in the loading fixture, the fixture assembly was then placed within the load frame, and measured to ensure it was centered and perpendicular with respect to the loading piston. The sample was then loaded at a constant rate until failure. An example of a fracture created by the above means is shown in **Fig. 2.5**.

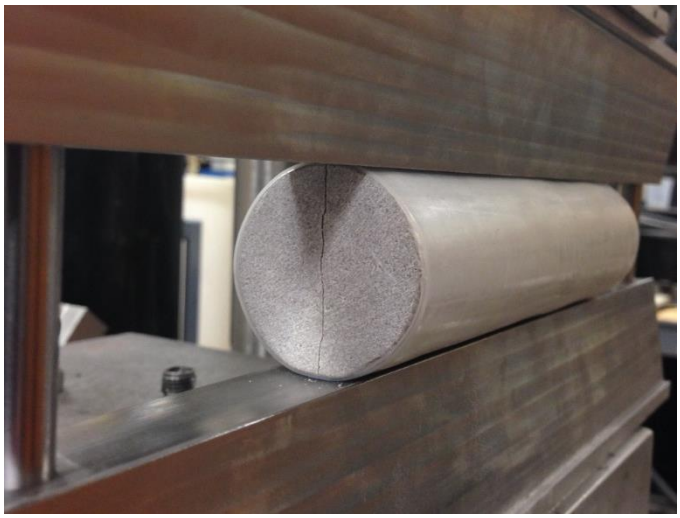

Fig. 2.5 – Close-up of Fracture Generated by Indirect Tension Test Loading.

Fracturing one test sample from each large core was attempted, however only two samples successfully generated a continuous fracture along the length of the sample. All other samples were destroyed during loading. The two successfully fractured samples corresponded to the same depth interval (Sample 7A and Sample 7B). Both samples were scanned using a Toshiba Aquilion RXL CT Scanner with 3D advanced visualization software. The CT scans were post-processed to visualize the resulting fracture void volume as shown in **Fig. 2.6** and **Fig. 2.7**.

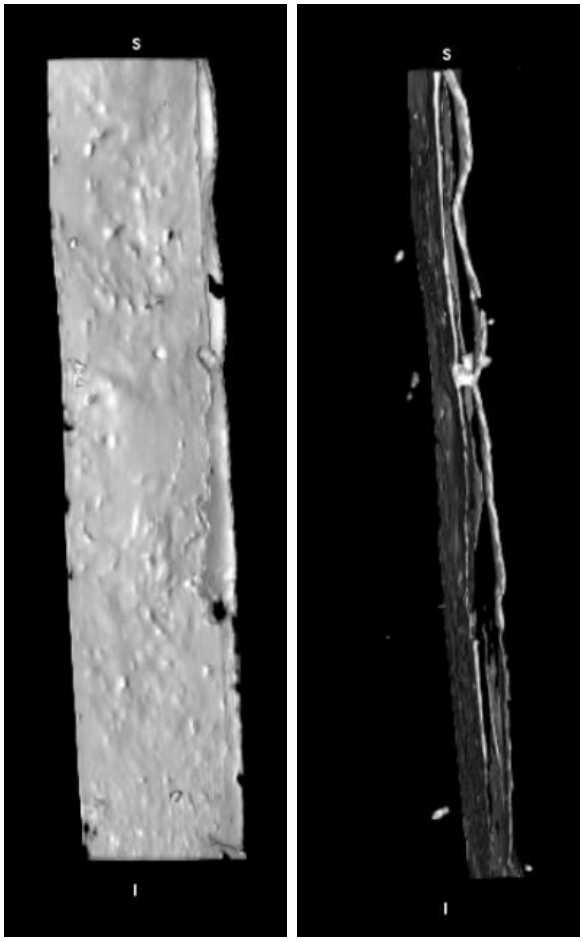

Fig. 2.6 – CT Scan of Sample 7A Fracture Void Space: (a) Side View; (b) Top View.

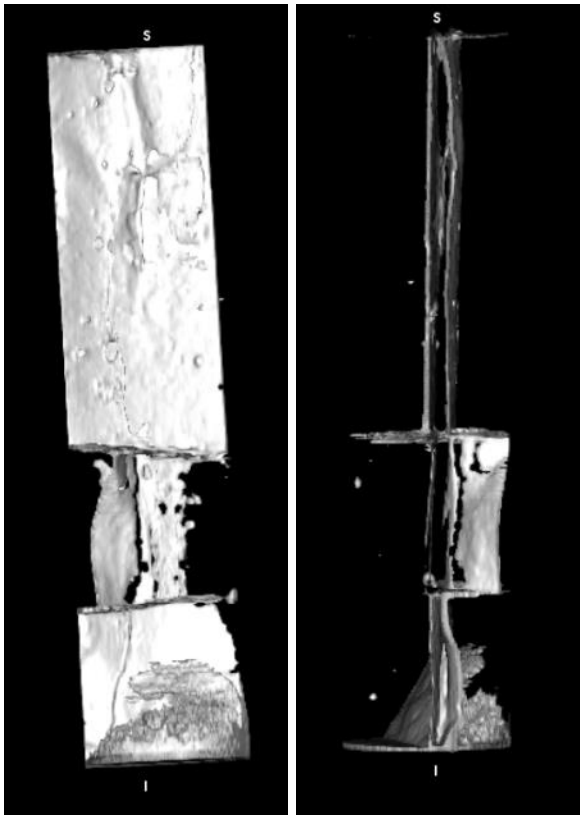

Fig. 2.7 – CT Scan of Sample 7B Fracture Void Space: (a) Side View; (b) Top View.

The CT scans of the fracture void volume show that both Sample 7A and Sample 7B generated a complex fracture along the length of each respective core sample. Sample 7A generated a set of two parallel fractures along the length of the core sample. Sample 7B on the other hand generated a far more complex fracture system comprised of two parallel longitudinal fractures intersected by two perpendicular fractures sectioning the core sample in three parts. Both fractured samples generated a fracture void volume interconnected from end to end of the core specimen, allowing the samples to be tested. The fracture aperture of both samples was measured to be 120 μm on average.

2.2.2.2 Saw-cut Samples

Core plug sample intervals where indirect tension test fracturing of one sample pair was unsuccessful were subsequently saw cut along the length of the remaining intact core plug sample. A 254-µm thick diamond coated rotary blade was used to cut the remaining core plug samples.

Each sample was cut in two equal halves along their longitudinal axis. The saw cut created some surface roughness on each fracture face. However, when the sample halves for each core plug were matched up, the resulting aperture was considerably less than that of the fractured samples described in Section 2.2.2.1.

In order to create a representative fracture aperture similar to that of the fractured samples, two stainless steel shims where placed along the outer edges of the saw cut halves parallel to the samples longitudinal axis. The stainless steel shims where cut from 100-µm thick shim stock and were cut into one-eighth inch wide strips, as shown in **Fig. 2.8**.

Fig. 2.8 – Example of Saw Cut Test Specimen with 100 µm Stainless Steel Shims to Control Fracture Aperture.

Once the shims were cut to length and placed on one half of the saw cut core plug sample, the remaining half was then placed on the top of the shims, taking care to match each half's orientation. Once both halves where mated together with the stainless steel shims in between, the mated halves where then placed within a Viton® heat shrink sleeve. Heat was then applied with a forced convection heat gun to shrink the Viton® sleeves around the core and hold the halves and stainless steel shims in place, in essence creating a fractured core plug test specimen cartridge as shown in **Fig. 2.9**.

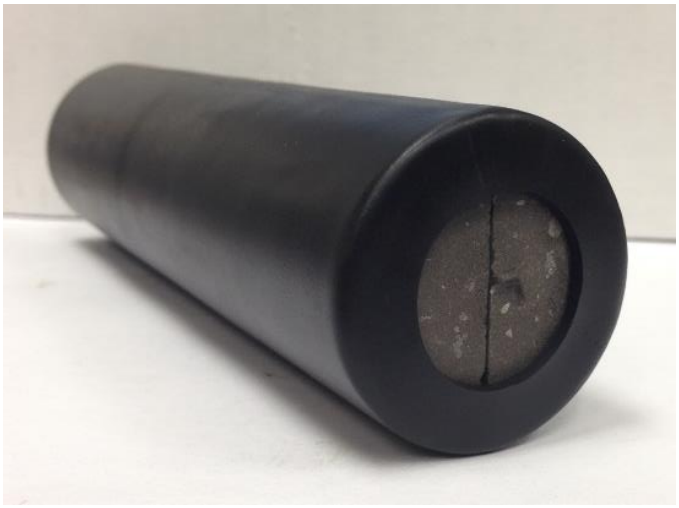

Fig. 2.9 – Example of Saw Cut Test Specimen Wrapped in Viton® Chemical Resistant Heat Shrink Sleeve.

Once the Viton® sleeve was heat-shrunk, it was then allowed to cool-off to room temperature. Once the core and sleeve temperature stabilized, both ends of the heat shrunk sleeve were trimmed off of the core plug ends to reveal the full core face and allow the entire fracture with to be exposed as shown in **Fig. 2.10**.

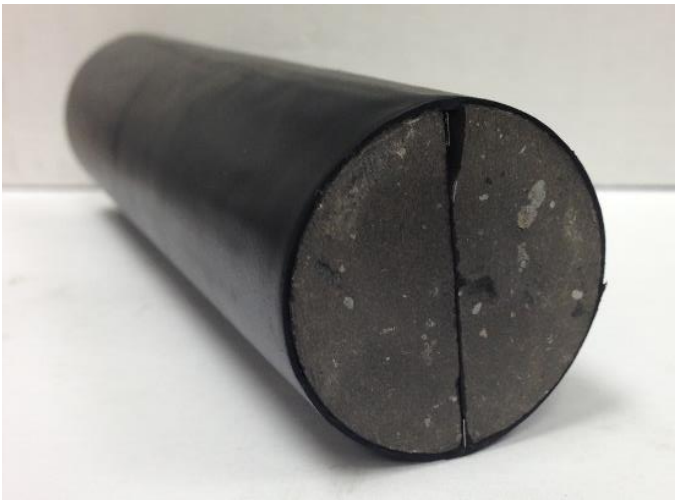

Fig. 2.10 – Example of Saw Cut Test Specimen Wrapped in Viton® Chemical Resistant Heat Shrink Sleeve, With Ends Trimmed for Testing.

2.3 Fracturing Fluid Water Composition

The representative fracturing water composition used to test the oil-water relative permeability in fractures was meant to represent a brine solution that might be used in the field. As commonly practiced in the field, surfactants for wettability alteration were added to the brine solution to create five different fracturing fluid compositions. The water salinity as well as the specific surfactants used are discussed in the following subsections.

2.3.1 Water Salinity

The brine solution used to test the oil-water relative permeability in fractures was reconstituted to reproduce a field brine composition that might be used as fracturing fluid. The specific composition was reproduced from a field sample water test report (report number 4607H-9H from 02/22/2016).

The total dissolved solids (TDS) for the representative oilfield brine solution is 26,805.70 PPM. In order to reconstitute this brine solution, five main compounds were used: calcium chloride ($CaCl_2$), sodium chloride (NaCl), magnesium chloride ($MgCl_2$), sodium bicarbonate ($NaHCO_3$), and sodium sulfate (Na_2SO_4).

The molecular weight of each ion within each corresponding compound was calculated as shown in **Table 2.3**. Using the molecular weight of each ion by compound, the weight percent concentration of each ion by compound was calculated as shown in **Table 2.4**. Using the weight percent ionic concentration by compound, the appropriate amount of each compound was calculated to result in the same ionic concentration as the target oilfield brine solution, with a final TDS of 26,810 PPM.

Table 2.3 – Molecular Weight of Individual Ions by Compounds Used to Re-constituted Formation Brine.

Frac Water Ionic Concentration		**Molecular Weight by Compound**				
Ion	g/L	**$CaCl_2$ - g/mol**	**NaCl - g/mol**	**$MgCl_2$ - g/mol**	**$NaHCO_3$ - g/mol**	**Na_2SO_4 - g/mol**
Calcium (as Ca)	0.481	40.078				
Magnesium (as Mg)	0.097			24.305		
Sodium (as Na)	9.704		22.990		22.990	45.980
Iron (as Fe)	0.016					
Chloride (as Cl)	15.995	70.900	35.450	70.900		
Sulfate (as SO_4)	0.363					96.056
Bicarbonate (as HCO_3)	0.150				61.016	
Total	26.806	110.978	58.440	95.205	84.006	142.036

Table 2.4 – As Prepared Ionic Concentration of Re-constituted Formation Brine.

Frac Water Ionic Concentration		**Ionic Concentration by Compound**					**Reconstituted Concentration (g/L)**
		$CaCl_2$ - (g/L)	**NaCl - (g/L)**	**$MgCl_2$ - (g/L)**	**$NaHCO_3$ - (g/L)**	**Na_2SO_4 - (g/L)**	
Ion	g/L	**1.33**	**24.35**	**0.38**	**0.21**	**0.54**	
Calcium (as Ca)	0.481	36.11%					0.480
Magnesium (as Mg)	0.097			25.53%			0.097
Sodium (as Na)	9.704		39.34%		27.37%	32.37%	9.811
Iron (as Fe)	0.016						0.000
Chloride (as Cl)	15.995	63.89%	60.66%	74.47%			15.904
Sulfate (as SO_4)	0.363					67.63%	0.365
Bicarbonate (as HCO_3)	0.150				72.63%		0.153
Total	26.806						**26.810**

2.3.2 Sample Conditioning and Surfactant Pairing

A total of ten large core plugs test samples with 1.5-in diameter by 6-in length where prepared. Of these ten samples, two were successfully fractured using the indirect tension test loading described in Section 2.2.2.1. The additional eight samples where fracturing was unsuccessful were saw cut as described in Section 2.2.2.2.

Given the wide variation in sample mineralogy as described in Section 2.2.1, all ten samples were divided into one of two categories: quartz rich samples and carbonate rich samples.

Samples selected for the quartz rich sample set had a volume fraction of quartz greater than 60%, and a volume of carbonate smaller than 3%. Samples selected for the carbonate rich sample set had a volume fraction of carbonate greater than 40% (where volume of carbonate was defined as the sum of calcite and dolomite in each sample).

Once subdivided into the aforementioned categories, the samples were then conditioned in formation oil at reservoir temperature (170 °F) for a duration of 30 days as shown in **Table 2.5**.

Table 2.5 – Summary of Sample Mineralogy and Sample Aging in Formation Oil.

	Mineralogy		Aging Dates		Aging
	Quartz	Carbonate	Date In	Date Out	Time (days)
Sample 5	72.0	2.0	4/10/17	5/10/17	30
Sample 7A	9.2	74.6	4/11/17	5/11/17	30
Sample 10	60.0	1.5	4/12/17	5/12/17	30
Sample 7B	9.2	74.6	4/13/17	5/13/17	30
Sample 3	65.9	3.0	4/14/17	5/14/17	30
Sample 2	51.0	40.0	4/15/17	5/15/17	30
Sample 4	65.0	2.0	4/16/17	5/16/17	30
Sample 1	40.0	51.0	4/17/17	5/17/17	30
Sample 8	67.3	1.9	4/18/17	5/18/17	30
Sample 6	31.0	46.0	4/19/17	5/19/17	30

With two different sample categories defined based on the dominant mineral composition of the samples, individual samples from each set (quartz rich and carbonate rich sample sets) were paired with one of four different fracturing fluid surfactant additives. These surfactant additives are actual additives presently used in the field. Each surfactant was given an arbitrary name: Surfactant A, Surfactant B, Surfactant C and Surfactant D.

The pairing of each surfactant additive with the corresponding test sample from each sample set is listed in **Table 2.6** and **Table 2.7**.

Table 2.6 – Pairing of Surfactant Type and Corresponding Quartz Rich Samples.

	Quartz Rich Samples		
Case	Sample No.	Quartz %	Carbonate %
No-Surfactant (Frac Fluid)	**5**	72.0	2.0
Surf. A	**10**	60.0	1.5
Surf. B	**3**	65.9	3.0
Surf. C	**4**	65.0	2.0
Surf. D	**8**	67.3	1.9

Table 2.7 – Pairing of Surfactant Type and Corresponding Carbonate Rich Samples.

	Carbonate Rich Samples		
Case	Sample No.	Quartz %	Carbonate %
No-Surfactant (Frac Fluid)	**7A**	9.2	74.6
Surf. A	**7B**	9.2	74.6
Surf. B	**2**	51.0	40.0
Surf. C	**1**	40.0	51.0
Surf. D	**6**	31.0	46.0

2.3.3 Surfactant Property Measurements

As discussed in Section 2.3.2, a total of five different brine solutions were prepared to be used as a test fluid for the measurement of oil-water relative permeability in fractures. These five distinct brine solutions were comprised of the brine solution prepared as described in Section 2.3.1, as well as the aforementioned brine with the addition of each surfactant additive at a concentration of one gallon per thousand gallons (1 gpt). These five brine solutions (No-Surfactant or "Frac Water", Surf. A, Surf. B, Surf. C, and Surf. D), were then each paired with a corresponding sample from each of the quartz rich sample set and the carbonate rich sample set, giving a total of ten different brine (with or without surfactant) and core plug test sample combinations as described in Table 2.6 and 2.7.

The contact angle (θ) of a single oil droplet surrounded by each respective brine solution (with or without surfactant) on the surface of a small rock chip from each test sample was measured at reservoir temperature (170 °F) to determine the wettability alteration provided by each surfactant additive, as shown in **Table 2.8** and **Fig. 2.11**.

Table 2.8 – Contact Angle Measurements for Each Sample and Surfactant Pairing.

Contact Angle Measurements (at 1 gpt)		
Surfactant	Core Sample	Contact Angle (°)
No Surfactant - QR	Sample 5	110.10
No Surfactant - CR	Sample 7A	116.00
Surf. A - QR	Sample 10	103.50
Surf. A - CR	Sample 7B	111.15
Surf. B - QR	Sample 3	91.55
Surf. B - CR	Sample 2	105.35
Surf. C - QR	Sample 4	81.25
Surf. C - CR	Sample 1	92.70
Surf. D - QR	Sample 8	63.10
Surf. D - CR	Sample 6	72.75

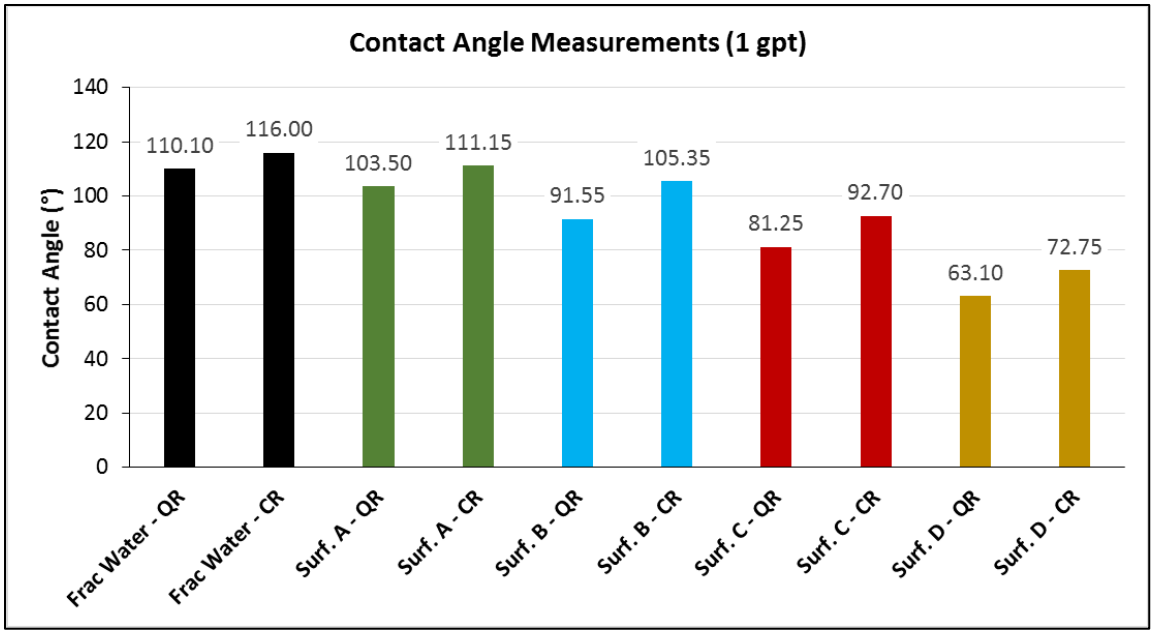

Fig. 2.11 – Contact Angle Measurements for Each Sample and Surfactant Pairing.

The measured contact angle indicates the resulting wettability of the rock surface which has been contacted by the brine solution (with or without surfactant). This contact angle can be divided into one of three categories to better describe the degree of surface wettability. The three categories include water-wet with a contact angle between 0 – 75°, intermediate-wet with a contact angle between 75 – 105°, and oil-wet with a contact angle between 105 – 180°.

It can be seen from Table 2.8 and Fig. 2.11 that the contact angle of the oil in the presence of brine without surfactant ("Frac Water") for both quartz rich and carbonate rich samples is mildly Oil-Wet. Each brine solution with a surfactant additive was then plotted in decreasing contact angle as shown in **Fig. 2.11**, indicating an increasing degree of wettability alteration ranging from Oil-Wet to Water-Wet (from left to right).

The oil-water interfacial tension (σ) was also measured between the formation oil and each of the brine (with or without surfactant) solutions. These measurements were also done at reservoir temperature (170 °F), using a capillary needle dispenser device. The measurement consists of dispensing a fixed volume oil droplet into the brine (with or without surfactant) and capturing a high resolution image which is then processed by a drop-shape-analysis software.

The interfacial tension measurements are not dependent of the rock sample, but only the two test fluids, namely formation oil and brine solution (with or without surfactant). The results of the interfacial tension measurements are listed in **Table 2.9** and plotted in **Fig. 2.12**.

Table 2.9 – Oil-Water Interfacial Tension Measurements for Each Surfactant.

Interfacial Tension (IFT) Measurements (at 1 gpt)	
Surfactant	IFT (mN/m)
Frac Water	21.78
Surf. A	10.45
Surf. B	8.58
Surf. C	10.68
Surf. D	1.65

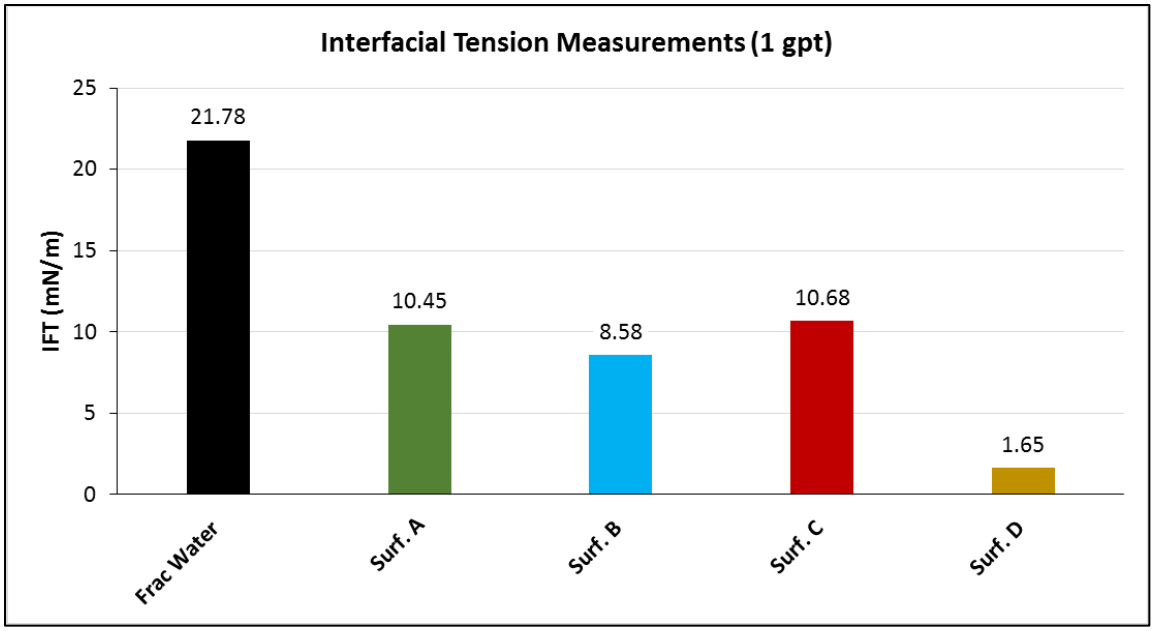

Fig. 2.12 – Oil-Water Interfacial Tension Measurements for Each Surfactant.

Each surfactant additive resulted in varying degrees of wettability alteration (contact angle reduction) and interfacial tension reduction. In order to capture the combined effect of both measured properties, a capillary pressure value was calculated for each brine solution and core plug sample combination.

The capillary pressure value was calculated using the following equation:

$$P_c = \frac{2\sigma \cos\theta}{r}$$

where σ is the oil-water interfacial tension, θ is the contact angle, and r is the pore radius. The resulting capillary pressure values for each test sample set is listed in **Table 2.10** and plotted in **Fig. 2.13**.

Table 2.10 – Calculated Capillary Pressure Value for Each Sample and Surfactant Pairing.

Capillary Pressure Value (at 1 gpt)		
Surfactant	Core Sample	P_c (mN/m/r)
Frac Water - QR	Sample 5	-14.97
Frac Water - CR	Sample 7A	-19.10
Surf. A - QR	Sample 10	-4.88
Surf. A - CR	Sample 7B	-7.54
Surf. B - QR	Sample 3	-0.46
Surf. B - CR	Sample 2	-4.54
Surf. C - QR	Sample 4	3.25
Surf. C - CR	Sample 1	-1.01
Surf. D - QR	Sample 8	1.49
Surf. D - CR	Sample 6	0.98

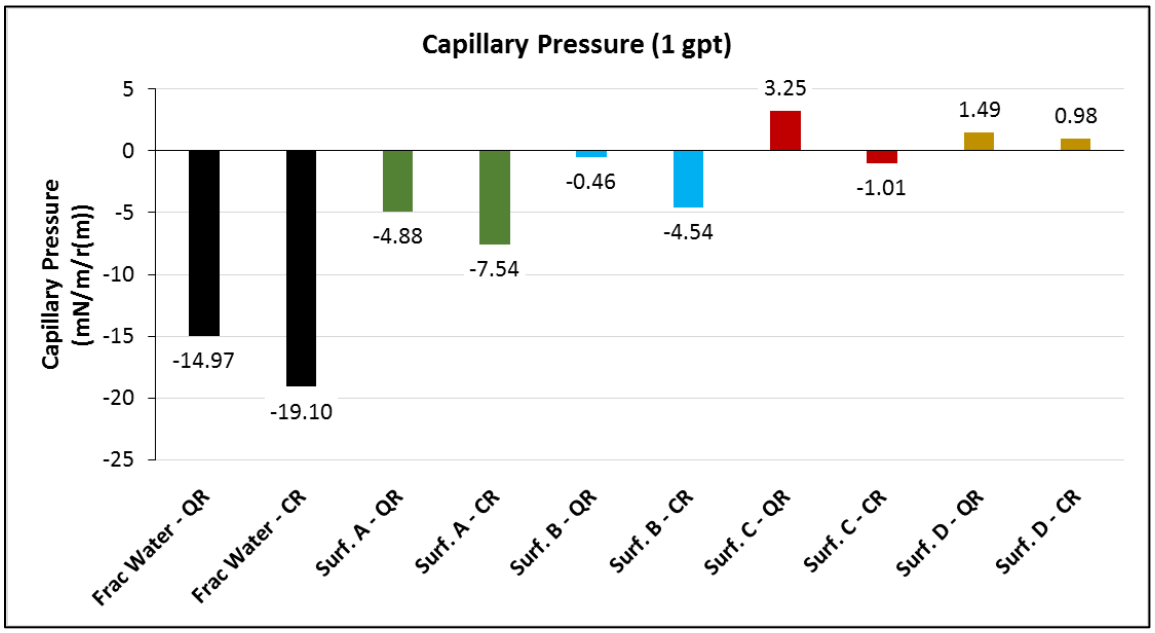

Fig. 2.13 – Calculated Capillary Pressure Value for Each Sample and Surfactant Pairing.

2.4 Experimental Equipment

A laboratory apparatus was constructed specifically for the measurement of oil-water relative permeability measurements in fractures. The apparatus is comprised by eight principal components: syringe pumps, hassler type core holder, confining pressure hydraulic pump, temperature controller, confining pressure transducer, differential pressure transducer, mass flow and density meter, and a back pressure regulator. The schematic of the experimental apparatus is shown in **Fig. 2.14**, and the functions of all components are discussed in the following subsections.

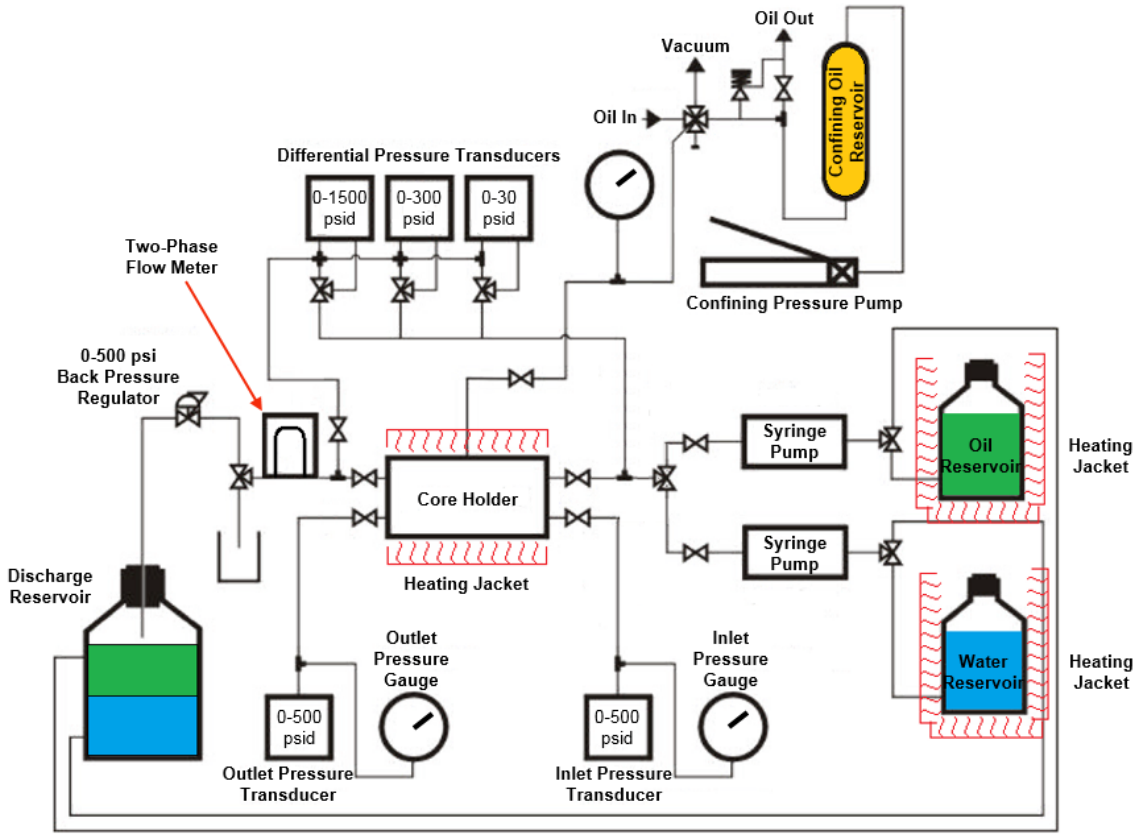

Fig. 2.14 – Schematic Representation of Experimental Equipment Set-up for Relative Permeability Measurement.

2.4.1 Syringe Pumps

Two syringe pumps were used to control the oil and water injected fractions respectively. The syringe pump used for oil injection was a Teledyne ISCO Model 500HP (Custom) with a capacity of 500 mL a pressure rating of 5,000 psig. The syringe pump used for water injection was a Teledyne ISCO Model 100DX with a capacity of 100 mL and a pressure rating of 10,000 psig.

Both syringe pumps were controlled simultaneously with a Teledyne ISCO D-Series Pump Controller which is capable of simultaneous control of up to four independent syringe pumps. The syringe pumps and controller are shown in **Fig. 2.15**.

Fig. 2.15 – Syringe Pumps and Pump Controller used for Oil and Water Injection.

2.4.2 Hassler Type Core Holder

The core holder used to provide the representative fracture closure pressure was a Phoenix Instruments Model TAM-HAS-1.5X20-3K-10 Hassler type core holder. The core holder body was fabricated from 17-4PH stainless steel, and all wetted parts are Hastelloy to prevent corrosion. The working pressure limit for this core holder is 3,000 psi, along with a working temperature of 300 °F. The core holder can accommodate cores with 1.5-in diameter and up to 20-in in length.

The core holder along with its components and various configurations is shown in **Fig. 2.16**, **Fig. 2.17**, **Fig. 2.18**, **Fig. 2.19** and **Fig. 2.20**.

The core holder was covered with a heating jacket around the main body, and two insulating jackets were used to insulate both inlet and outlet ports as depicted in **Fig. 2.16**.

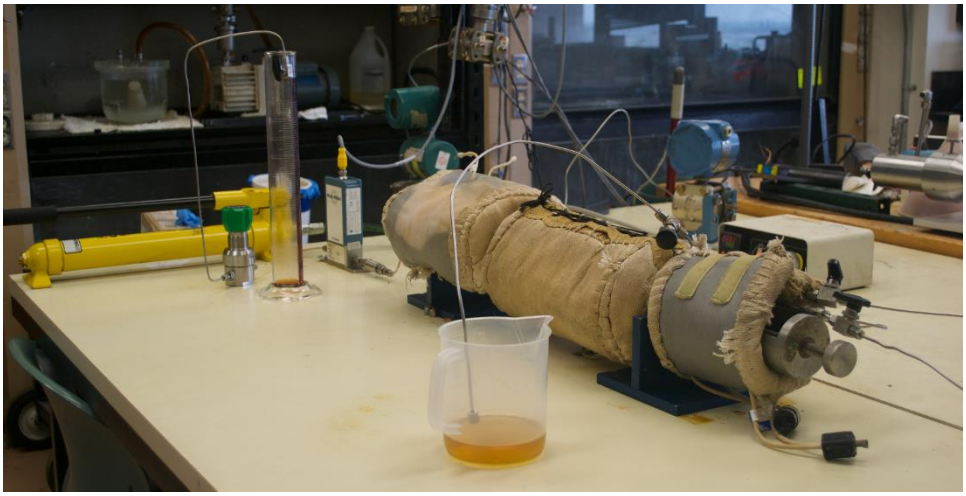

Fig. 2.16 – Experimental Equipment Setup showing Hassler Type Core Holder with Heating Jackets.

The core assembled core holder is depicted with the heating jacket and insulating jackets removed in order to view the main components as shown in Fig. 2.17 and Fig. 2.18. It can be seen in these two figures that the fractured core test specimen is located within the core holder body, within the first half of the inlet side, beneath the heating jacket.

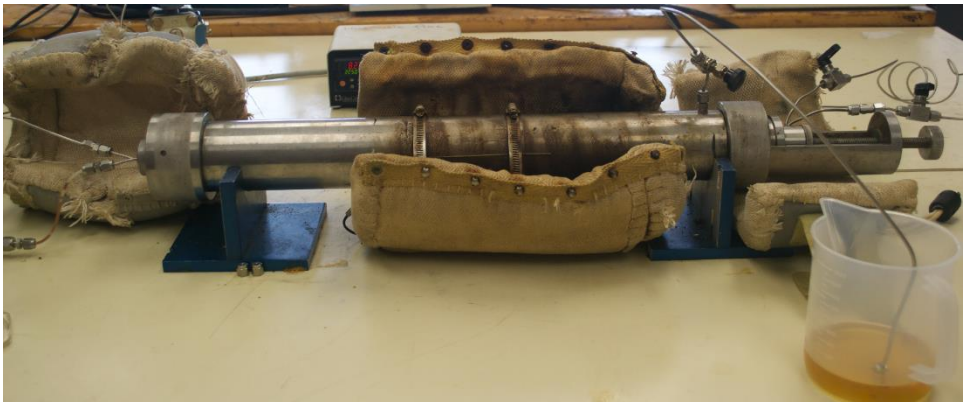

Fig. 2.17 – Hassler Type Core Holder with Heating Jackets Removed.

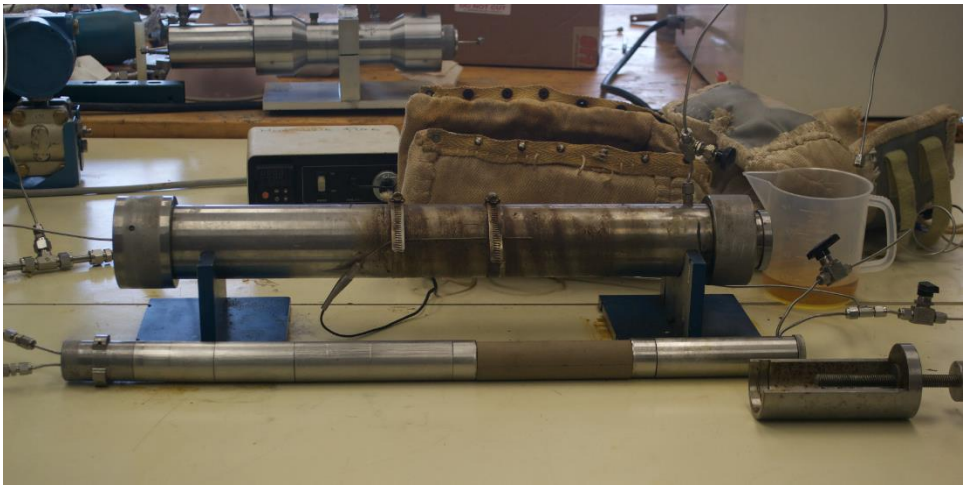

Fig. 2.18 – Disassembled Hassler Type Core Holder Showing Outlet End-piece Piston (left), Fractured Core Test Specimen (center), and Inlet End-piece Piston (right).

A close up image of the fractured core held in between the inlet and outlet end-piece pistons can be seen in **Fig. 2.19**. In this figure, the heat shrink sleeve has been removed to show the fracture within the sample.

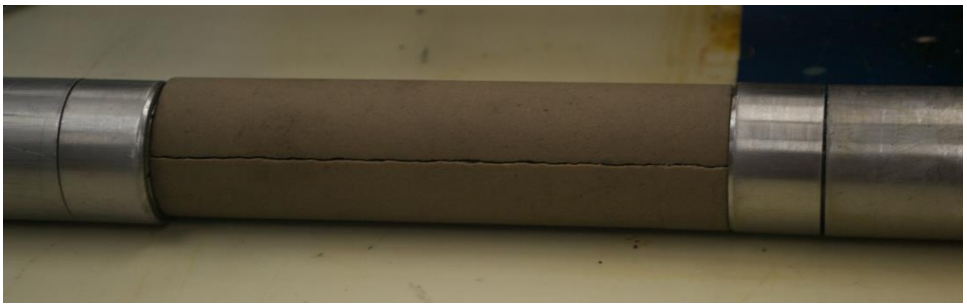

Fig. 2.19 – Close-up of Fractured Core Test Specimen in between Inlet and Outlet End-piece Pistons.

A close up image of the outlet end-piece piston face along with the edge of the fractured core sample can be seen in **Fig. 2.20**. Both inlet and outlet end-piece piston faces have small channels cut concentric to the circumference as well as channels cut in the radial direction to allow flow distribution over the entire face of the test specimen.

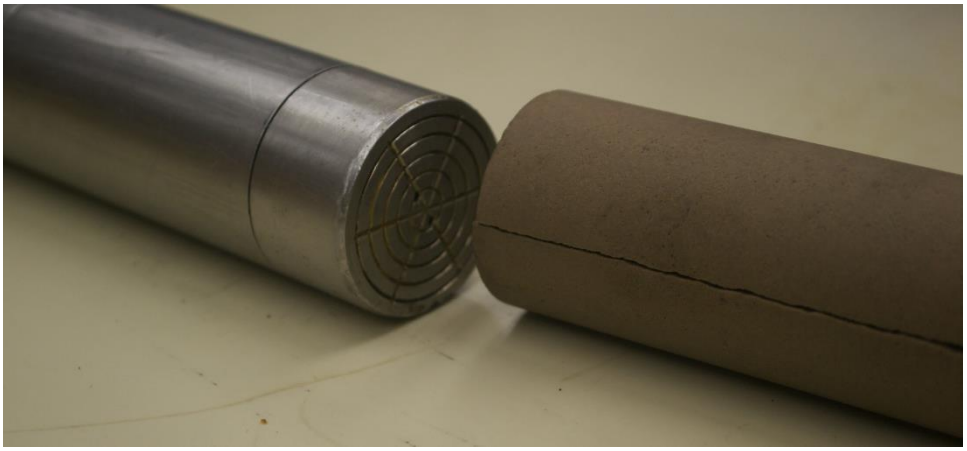

Fig. 2.20 – Close-up of Fractured Core Test Specimen and Outlet End-piece Piston Face.

2.4.3 Confining Pressure Hydraulic Pump

A hydraulic oil hand pump was used to provide confining pressure to the core holder. The hydraulic pump used was an Enerpac P39 hand pump, with a maximum working pressure of 10,000 psig.

2.4.4 Temperature Controller

The heating jacket was controlled by a Glas-Col DigiTrol II temperature controller. This temperature controller uses a type J thermocouple attached to the main body of the core holder (in between the core holder outer body and the heating jacket). The controller uses a proportional-integral-derivative controller (PID controller) to adjust power input to the heating jacket to reach and keep a temperature set-point determined by the user.

The hassler core holder does not have a port for a thermocouple in order to directly measure the temperature of the test specimen during a test. Therefore, the core holder was temporarily assembled with a fractured sample with a type J thermocouple placed at the center of the test sample in between both fracture halves. The heating jacket was then tested at various temperature set points to determine the corresponding temperature set point in order for the test sample to reach the desired representative reservoir temperature of 170 °F. Each heating experiment was recorded for 24 hours, beginning at room temperature. It was found that for the specific configuration being used, the corresponding temperature set point for the heating jacket was 225 °F, resulting in a steady state core temperature of 170 °F as shown in **Fig. 2.21**.

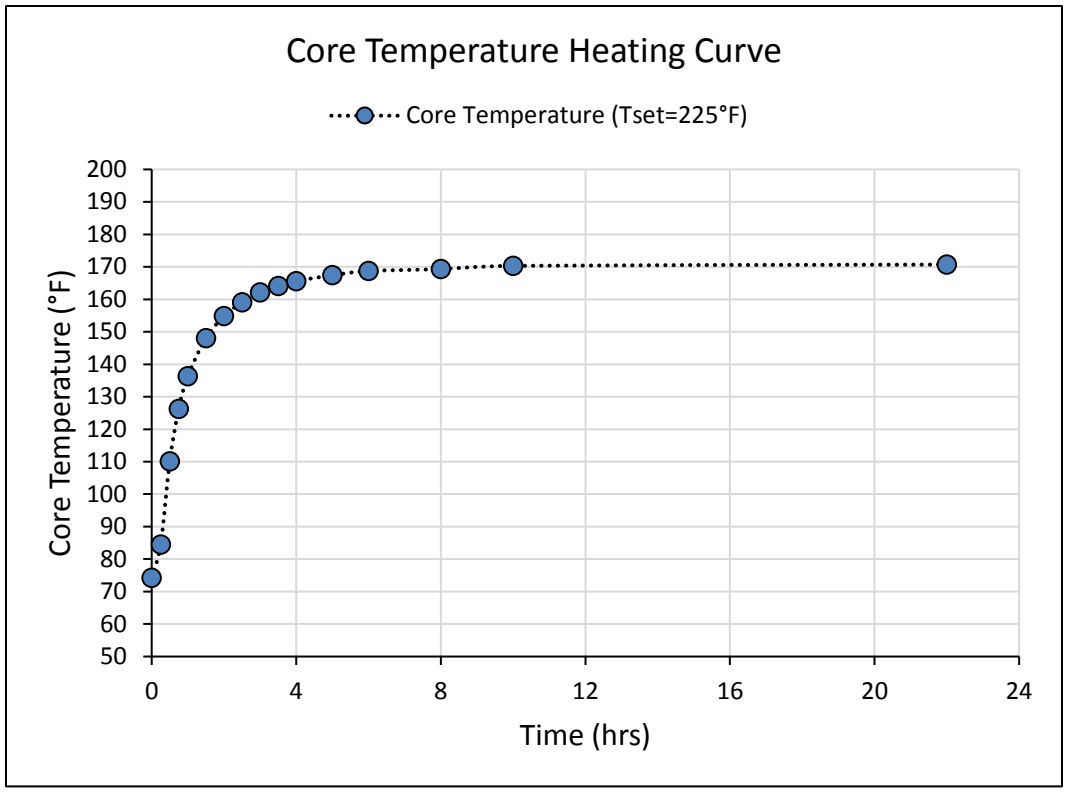

Fig. 2.21 – Transient Core Temperature Heating Curve Measured at the Center of the Fractured Core Test Specimen using a Type J Thermocouple.

2.4.5 Confining Pressure Transducer

The core holder confining pressure was monitored and recoded using a Rosemount Alpha-line Pressure Transducer. The pressure transducer has a maximum working pressure of 6000 psig. The digital output signal generated from the confining pressure transducer was calibrated using a dead weight tester in order to convert the milliamp output to a pressure value. The calibration curve for the confining pressure transducer is shown in **Fig. 2.22**.

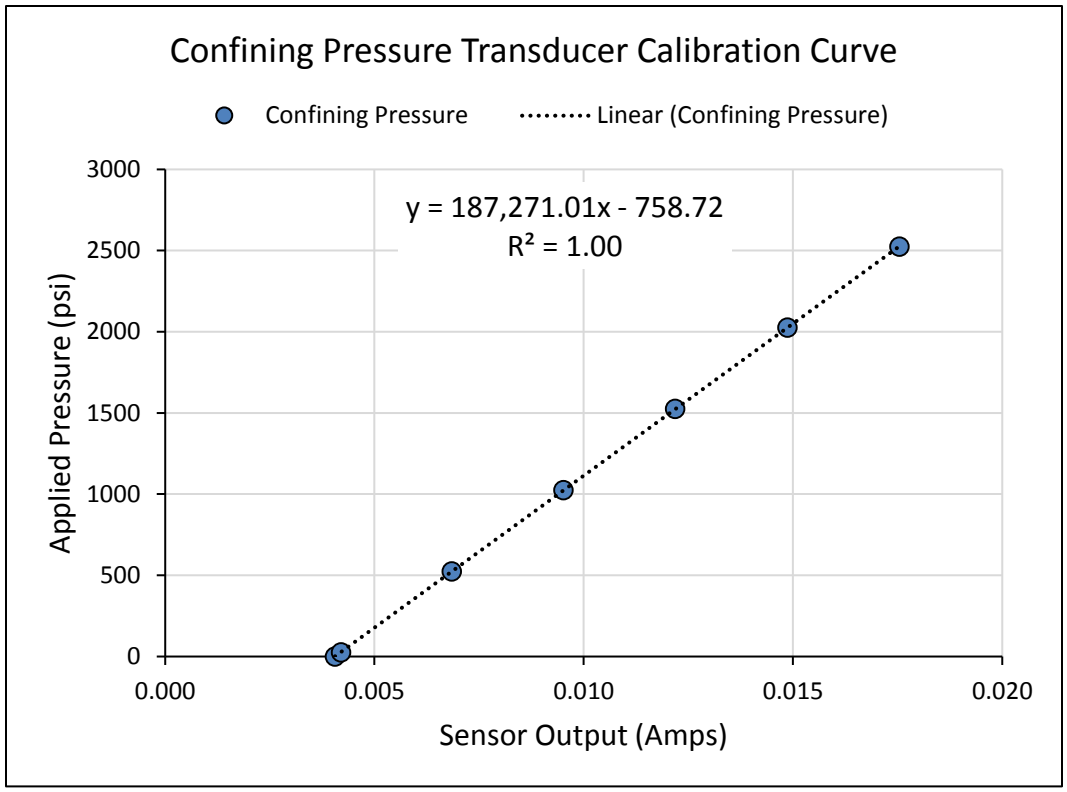

Fig. 2.22 – Confining Pressure Transducer Calibration Curve Using a Dead-Weight Calibration Device.

2.4.6 Differential Pressure Transducer

The differential pressure across the core was monitored using a Honeywell Model 41123-0011-13-07 differential pressure transducer. The differential pressure transducer has a maximum working pressure of 2000 psig. The digital output signal generated from the differential pressure transducer was calibrated using a dead weight tester in order to convert the milliamp output to a pressure value. The calibration curve for the differential pressure transducer is shown in **Fig. 2.23**.

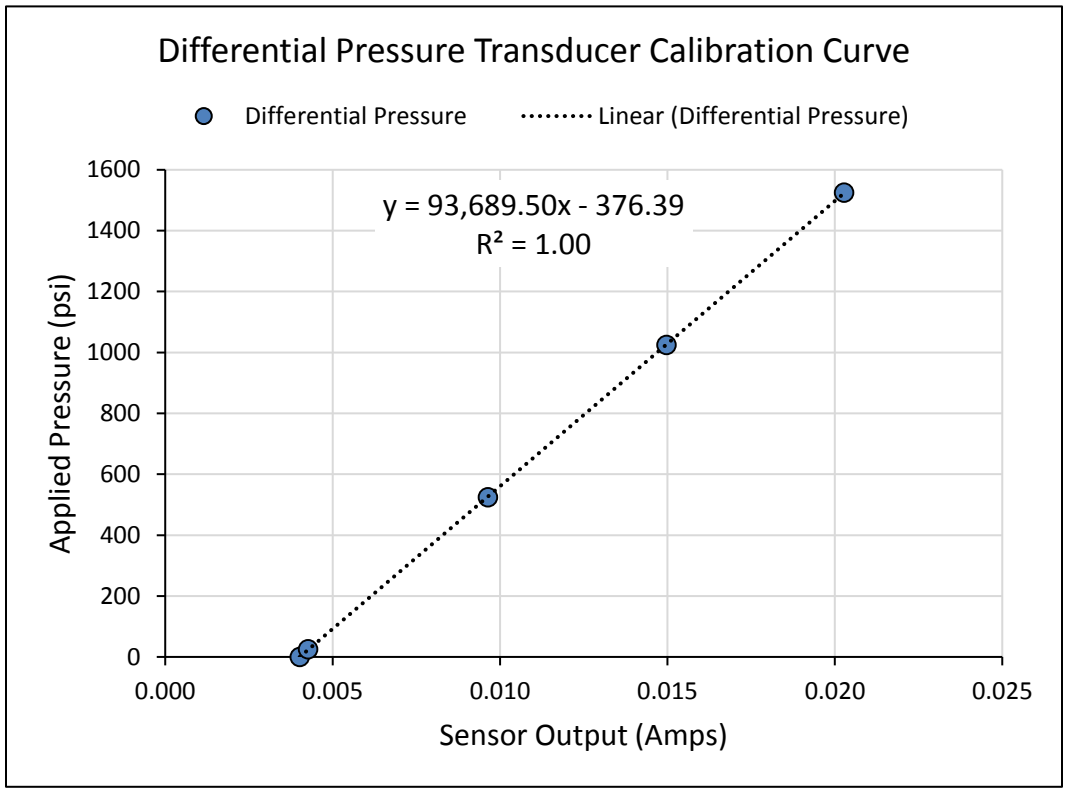

Fig. 2.23 – Differential Pressure Transducer Calibration Curve Using a Dead-Weight Calibration Device.

2.4.7 Mass Flow and Density Meter

The outlet of the core holder was connected to an ultra-low flow rate Coriolis mass flow and density meter. The mass flow rate and density meter used was a Micro Motion Model LF2M sensor. The mass flow rate range for this sensor is 0.2 – 5 g/min with a mass flow measurement accuracy of ±1% of the rate. The density range is 0 – 2 g/cm^3 with a density measurement accuracy of ±0.005 g/cm^3. The calibration curves for both mass flow rate and density measurements are shown in **Fig. 2.24** and **Fig. 2.25** respectively.

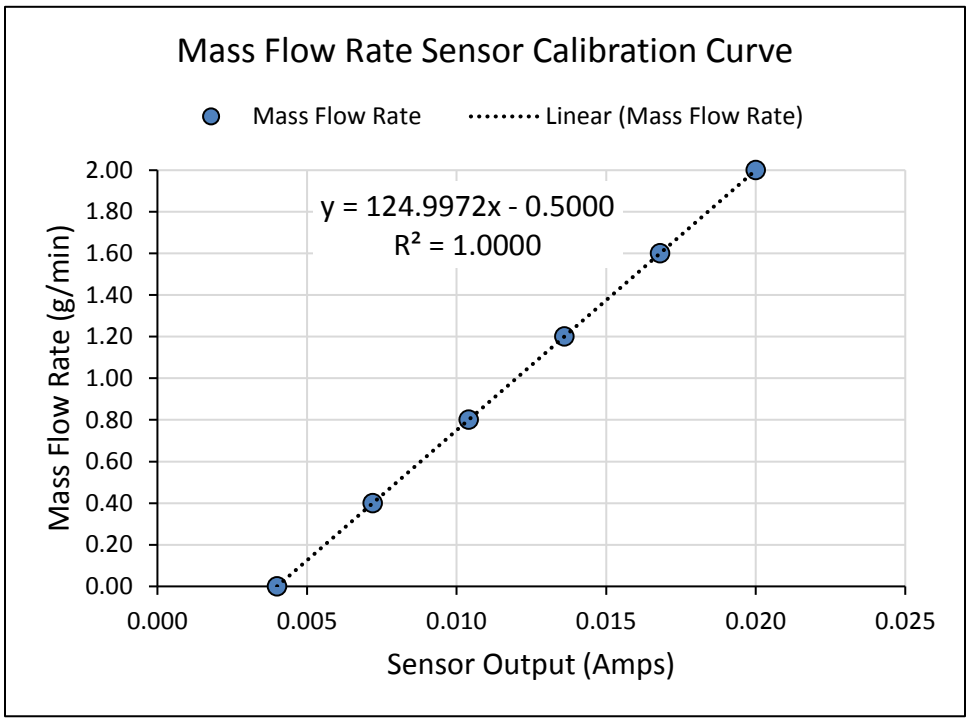

Fig. 2.24 – Mass Flow Rate Sensor Output Calibration Curve.

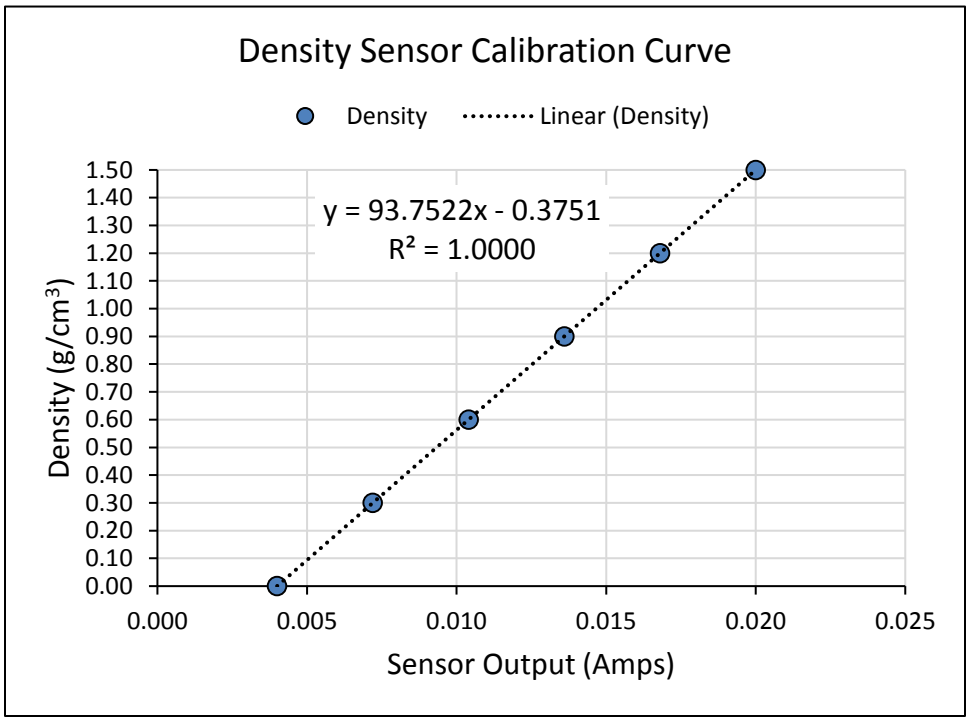

Fig. 2.25 – Density Sensor Output Calibration Curve.

2.4.8 Back Pressure Regulator

A back pressure regulator was used to control the outlet pressure of the core holder. The regulator used was a Swagelok Model P2000 inline backpressure regulator. The inlet pressure range for this regulator is 0 – 2,000 psi.

2.4.9 Digital Oil Bath

A heated oil bath was used to condition all fractured core samples in formation oil. The oil bath used was a LABNICS Equipment LOB – 100T Digital Oil Bath. The maximum heating temperature for this oil bath is 250 °F.

2.5 Experimental Procedure

The steady state relative permeability measurement procedure described in Section 1.2.2 was modified for the measurement of oil-water relative permeability in fractures using the laboratory apparatus and equipment described in Section 2.4.

First all fractured core samples where conditioned in formation oil for a duration of 30 days at reservoir temperature (170 °F). After the core sample is conditioned, the sample is then placed within the core holder and subsequent steady stat oil-water relative permeability testing is conducted.

The equipment setup procedure followed for all testing is described as follows:

1. Insert outlet end-piece piston into core holder.
2. Insert fractured or saw-cut sample into the core holder from the inlet end, aligning the fracture in a vertical orientation.
3. Insert inlet end-piece piston.
4. Attach inlet end-piece connector to secure inlet end-piece piston and hand tighten the piston and core assembly within the core holder to ensure proper mating of piston and core faces.
5. Connect inlet and outlet flow lines.
6. Connect inlet and outlet differential pressure lines.
7. Conduct a check of all connections ensuring proper torque has been applied to all threaded connections.
8. Attach heating jacket and insulating jackets on core holder.
9. Set heating jacket temperature controller to target temperature (225 °F).
10. Allow the core holder and core to reach target temperature.
11. Close the confining pressure outlet valve and apply desired confining stress (1,750 psig), and allow confining pressure to stabilize. Re-adjust if necessary.
12. Once confining pressure has stabilized, wait for a minimum of 8 hours to allow any creep that might occur at the fracture face.
13. Core holder assembly and test specimen are ready to begin the measurement procedure.

Once the experimental setup procedure has been completed, the steady state oil-water relative permeability measurement is conducted. There are 7 measurement steps used for each sample tested. The measurement procedure is summarized in **Table 2.11**.

Table 2.11 – Steady State Fracture Relative Permeability Measurement Procedure Summary.

Steady State Facture Relative Permeability Test Procedure						
Step	Procedure	Measured Value		End Point	Oil Injection Rate (mL/min)	Water Injection Rate (mL/min)
1	Flood core with oil, measure k_o @ $S_w = 0$	k_o			0.50	0.00
2	Inject oil and water ($F_w = 20\%$)	k_{eo}	k_{ew}		0.40	0.10
3	Inject oil and water ($F_w = 40\%$)	k_{eo}	k_{ew}		0.30	0.20
4	Inject oil and water ($F_w = 60\%$)	k_{eo}	k_{ew}		0.20	0.30
5	Inject oil and water ($F_w = 80\%$)	k_{eo}	k_{ew}		0.10	0.40
6	Flood core with water, measure k_{ew} @ S_{or}		$k_{ew\ @\ Sor}$	S_{or}	0.00	0.50
7	Flood core with oil, measure k_o @ S_{wirr}	$k_{eo\ @\ Swirr}$		S_{wirr}	0.50	0.00

An example pump schedule used for all testing is shown in **Table 2.12**. Each test stage was allowed 65 minutes to reach steady state. A total of 130 mL of oil and 97.5 mL of water was used in each test.

Table 2.12 – Steady State Fracture Relative Permeability Pump Schedule.

Steady State Facture Relative Permeability Test Pump Schedule							
Test Stage	Start Time (HH:MM:SS)	Oil (mL/min)	Water (mL/min)	Elapsed Time (sec)	Interval Time (min)	Cum. Oil (mL)	Cum. Water (mL)
Stage 1	10:00:00 AM	0.50	0.00	3900	65.00	32.50	0.00
Stage 2	11:05:00 AM	0.40	0.10	7800	65.00	58.50	6.50
Stage 3	12:10:00 PM	0.30	0.20	11700	65.00	78.00	19.50
Stage 4	1:15:00 PM	0.20	0.30	15600	65.00	91.00	39.00
Stage 5	2:20:00 PM	0.10	0.40	19500	65.00	97.50	65.00
Stage 6	3:25:00 PM	0.00	0.50	23400	65.00	97.50	97.50
Stage 7	4:30:00 PM	0.50	0.00	27300	65.00	130.00	97.50
END TIME	5:35:00 PM				Total Vol.	130.00	97.50
TOTAL TIME	7:35:00					227.50	

2.6 Steady-State Oil-Water Fracture Relative Permeability Determination

There are two sets of recorded data, the first set is comprised of all sensor data, namely mixture density (ρ_m) and mixture mass flow rate ($\dot{m}_m$) from the ultra-low-flow Coriolis mass flow and density meter, as well as the differential pressure (ΔP) and the confining pressure ($P_{confining}$) from each respective pressure transducer. The second set of recorded data consists of the syringe pump data, namely water injection rate ($Q_{w,in}$) and oil injection rate ($Q_{o,in}$). All sensor and pump data is recorded throughout the experiment at a time interval of one second.

The volumetric flow rate at the Coriolis mass flow and density meter is then calculated as follows:

$$Q_{m,out} = \dot{m}_m/\rho_m \quad \text{(2-1)}$$

with

$$\rho_m = \frac{\rho_o Q_{o,out} + \rho_w Q_{w,out}}{Q_{m,out}} \quad \text{(2-2)}$$

and

$$Q_{m,out} = Q_{o,out} + Q_{w,out} \quad \text{(2-3)}$$

therefore, using **Eq. 2-1**, **Eq. 2-2** and **Eq. 2-3** the volumetric flow rate of each respective phase can be calculated as shown in **Eq. 2-4** and **Eq. 2-5**:

$$Q_{o,out} = \left(\frac{\rho_m - \rho_w}{\rho_o - \rho_w}\right)\left(\frac{\dot{m}_m}{\rho_m}\right) \quad \text{(2-4)}$$

$$Q_{w,out} = \left(\frac{\rho_m - \rho_o}{\rho_w - \rho_o}\right)\left(\frac{\dot{m}_m}{\rho_m}\right) \quad \text{(2-5)}$$

Steady state at each stage is considered to be reached when there is no change in differential pressure (ΔP_{ss}) and no change in phase saturations ($Q_{i,in} = Q_{i,out}$).

The absolute permeability of the fracture is determined in the first stage of the experiment, when the fracture has 100% saturation of oil, and is calculated using Darcy's law as shown in **Eq. 2-6**:

$$k = -\frac{Q\,\mu\,L}{A\,\Delta P_{ss}} \quad \text{.....(2-6)}$$

Once the flow of both oil and water at fixed fractions through the fracture is finished, the respective effective permeabilities are calculated as by **Eq. 2-7**, and **Eq. 2-8**:

$$k_{eo} = -\frac{Q_o\,\mu_o\,L}{A\,\Delta P_{ss}} \quad \text{.....(2-7)}$$

$$k_{ro} = k_{eo}/k \quad \text{.....(2-8)}$$

The relative permeabilities are calculated as shown in **Eq. 2-9** and **Eq. 2-10**:

$$k_{ew} = -\frac{Q_w\,\mu_w\,L}{A\,\Delta P_{ss}} \quad \text{.....(2-9)}$$

$$k_{rw} = k_{ew}/k \quad \text{.....(2-10)}$$

Additionally, the oil and water saturations in the fracture are calculated throughout the experiment as shown in **Eq. 2-11** and **Eq. 2-12**:

$$S_w = \left(\sum Q_{w,in}t - \sum Q_{w,out}t\right)/V_{fracture} \quad \text{.....(2-11)}$$

$$S_o = \left(\sum Q_{o,in}t - \sum Q_{o,out}t\right)/V_{fracture} \quad \text{.....(2-12)}$$

Finally, a steady state relative permeability curve is generated by plotting the oil relative permeability and water relative permeability as a function of the water saturation. Furthermore, a check for laminar flow is conducted to ensure the validity of Darcy's law for the determination of the oil-water relative permeability.

The hydraulic diameter (D_h) is a term commonly used in flow problems dealing with non-circular tubes and channels as described by White (2011), and when analyzing the flow through fractures, the problem can be simplified as flow through parallel plates, which is a special case of flow through rectangular ducts. The hydraulic diameter for square ducts is shown in **Eq. 2-13** and defined as:

$$D_h = 4A/P_{wet} \quad \text{.....(2-13)}$$

where A is the cross-sectional area, and P_{wet} is the wetted perimeter in contact with the fluid. For the specific case of flow through parallel plates separated by an aperture (a_f) and having a width (w_f), the hydraulic diameter then becomes **Eq. 2-14**:

$$D_h = 4a_f w_f / 2\left(a_f + w_f\right) \quad \text{.....(2-14)}$$

Given that the width of the fracture is much greater than the aperture ($w_f \gg a_f$), the hydraulic diameter is simplified by taking the limit as the width tends to infinity as shown in **Eq. 2-15**:

$$D_h = \lim_{w_f \to \infty} 4a_f w_f / 2\left(a_f + 2w_f\right) = 2a_f \quad \text{.....(2-15)}$$

The Reynold's Number for fully developed flow in parallel plates having an aperture (a_f) is then calculated as shown in **Eq. 2-16** from White (2011):

$$Re = \rho v D_h / \mu \quad \text{.....(2-16)}$$

All tests were conducted using a total volumetric flow rate of 0.5 mL/min, which led to a Reynolds Number of 0.30 and 1.56 for oil and water respectively, which indicates laminar flow ($Re < 1000$) and therefore Darcy's Law is valid for all tests conducted.

3. FRACTURE OIL-WATER RELATIVE PERMEABILITY TEST RESULTS

3.1 Introduction

This section contains the results from all ten steady state oi-water relative permeability measurements in fractures. The experimental equipment, experimental procedure and the steady-state oil-water fracture relative permeability determination are discussed in Section 2.

This section presents all relevant experiment measurements which are presented in four sets of data. The first set consists of a figure in which the continuous sensor data is plotted, which includes differential pressure (ΔP) and confining pressure ($P_{confining}$), each plotted at one second intervals, as well as mixture density (ρ_m), and mixture volumetric flow rate (Q_m), each plotted as a moving average at fifty second intervals.

Presented as the second set of data is a table summarizing the recorded measurements from the preceding figure, showing the steady-state differential pressure for each injected fraction of oil and water.

The third set of data presented in each experiment is a table summarizing the calculated effective and relative permeabilities for both oil and water respectively, along with the calculated water saturation corresponding to each steady-state stage.

Finally, the last set of data presented is the resulting oil-water fracture relative permeability curve for each experiment, which is plotted as the calculated oil and water relative permeability as a function of calculated fracture water saturation along with a best fit generalized Brooks-Corey relation for each respective relative permeability.

3.2 Generalized Brooks-Corey Relations for Oil-Water Relative Permeability

The generalized Brooks-Corey relations where modified from the original Brooks-Corey Correlations for relative permeability published by Brooks and Corey (1966), to allow their application to a wider range of rock wettability characteristics. These generalized correlations for an oil-water systems can be used to change the endpoints of each respective relative permeability curve as well as adjusting the curvature, to allow a best fit to experimental data, and follow a power-law relationship.

The expressions used to fit the experimental data to the modified Brooks-Corey relations are:

$$k_{ro} = k_{ro(S_{w\,min})}\left[\frac{S_{w\,max} - S_w - S_{orw}}{S_{w\,max} - S_{wi} - S_{orw}}\right]^{C_o} \quad \text{.....(3-1)}$$

$$k_{rw} = k_{rw(S_{orw})}\left[\frac{S_w - S_{wcr}}{S_{w\,max} - S_{wcr} - S_{orw}}\right]^{C_w} \quad \text{.....(3-2)}$$

$$P_{cow} = P_{c(S_{wcr})}\left[\frac{S_{w\,max} - S_w - S_{orw}}{S_{w\,max} - S_{wcr} - S_{orw}}\right]^{C_p} \quad \text{.....(3-3)}$$

where k_{ro} and k_{rw} are the relative permeability to oil and water respectively, $k_{ro(S_{w\,min})}$ and $k_{rw(S_{orw})}$ are the endpoint relative permeabilities for oil and water respectively, P_{cow} is the capillary pressure for the oil-water system, $P_{c(S_{wcr})}$ is the capillary pressure at critical water saturation, $S_{w\,max}$ is the maximum water saturation, S_{wi} is the initial water saturation, S_{wcr} is the critical water saturation, and S_{orw} is the residual oil saturation. The Corey oil exponent C_o, Corey water exponent C_w, and Corey capillary pressure exponent C_p, each range in value from 1 to 6 and control the curvature of each curve.

3.3 Quartz Rich Sample Set Test Results

The quartz rich samples were tested in five different experiments. The first test conducted with no surfactant is shown in **Fig. 3.1** and summarized in **Table 3.1**, and a summary of the calculated relative permeabilities are shown in **Table 3.2** and **Fig. 3.2**.

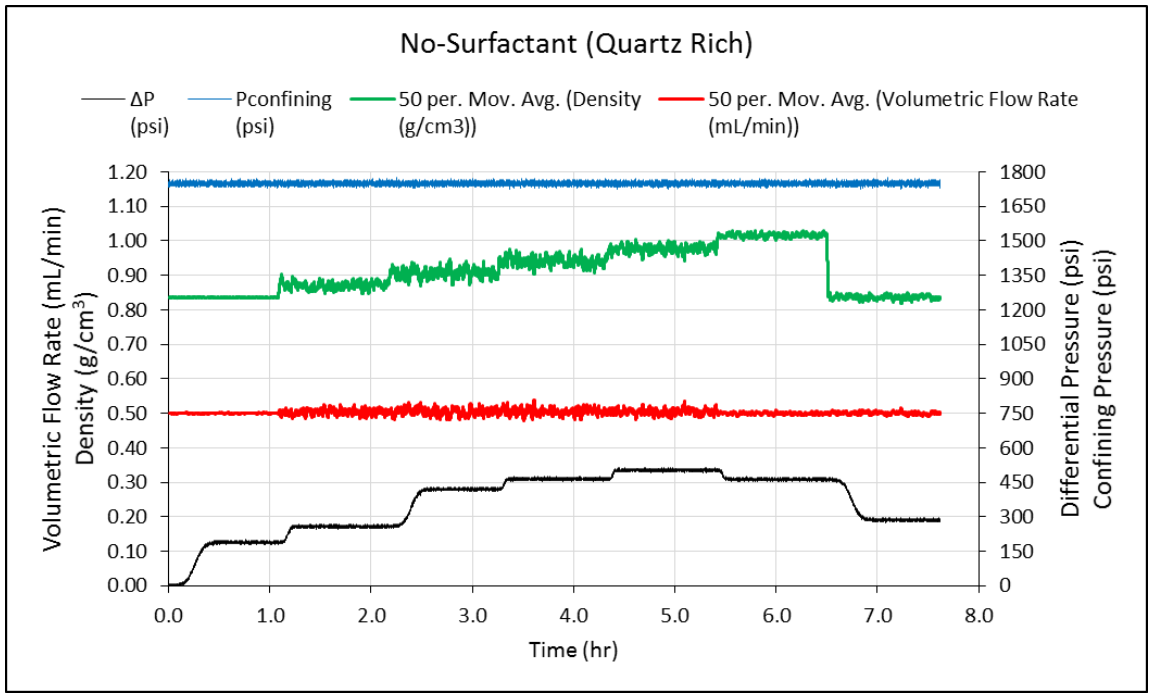

Fig. 3.1 – Recorded Data from Fracture Relative Permeability Test for No-Surfactant Quartz Rich Test Specimen Pairing.

Table 3.1 – Measured Fracture Relative Permeability Test Data for No-Surfactant Quartz Rich Test Specimen Pairing.

No-Surfactant (Quartz Rich) - Measured Data								
F_o	F_w	Q_{Total} (mL/min)	Q_{oil} (mL/min)	Q_{water} (mL/min)	P_{inlet} (psi)	ΔP_{ss} (psi)	P_{outlet} (psi)	P_{ave} (psi)
1.00	0.00	0.50	0.50	0.00	214	189	25	120
1.00	0.00	0.50	0.50	0.00	289	258	31	160
0.80	0.20	0.50	0.40	0.10	473	420	53	263
0.60	0.40	0.50	0.30	0.20	523	465	58	290
0.40	0.60	0.50	0.20	0.30	565	503	62	313
0.20	0.80	0.50	0.10	0.40	520	463	57	289
0.00	1.00	0.50	0.00	0.50	322	286	36	179

Table 3.2 – Calculated Fracture Relative Permeability Data for No-Surfactant Quartz Rich Test Specimen Pairing.

No-Surfactant (Quartz Rich) - Calculated Relative Permeability						
F_o	F_w	$S_{w\text{-}vol}$	K_{eo} (md)	K_{ew} (md)	K_{ro}	K_{rw}
1.00	0.00	0.00	308.91	0.00	1.00	0.00
1.00	0.00	0.13	210.91	0.00	0.68	0.00
0.80	0.20	0.34	90.95	20.43	0.29	0.07
0.60	0.40	0.43	59.88	36.91	0.19	0.12
0.40	0.60	0.52	36.09	51.19	0.12	0.17
0.20	0.80	0.62	20.08	74.15	0.06	0.24
0.00	1.00	0.83	0.00	150.04	0.00	0.49

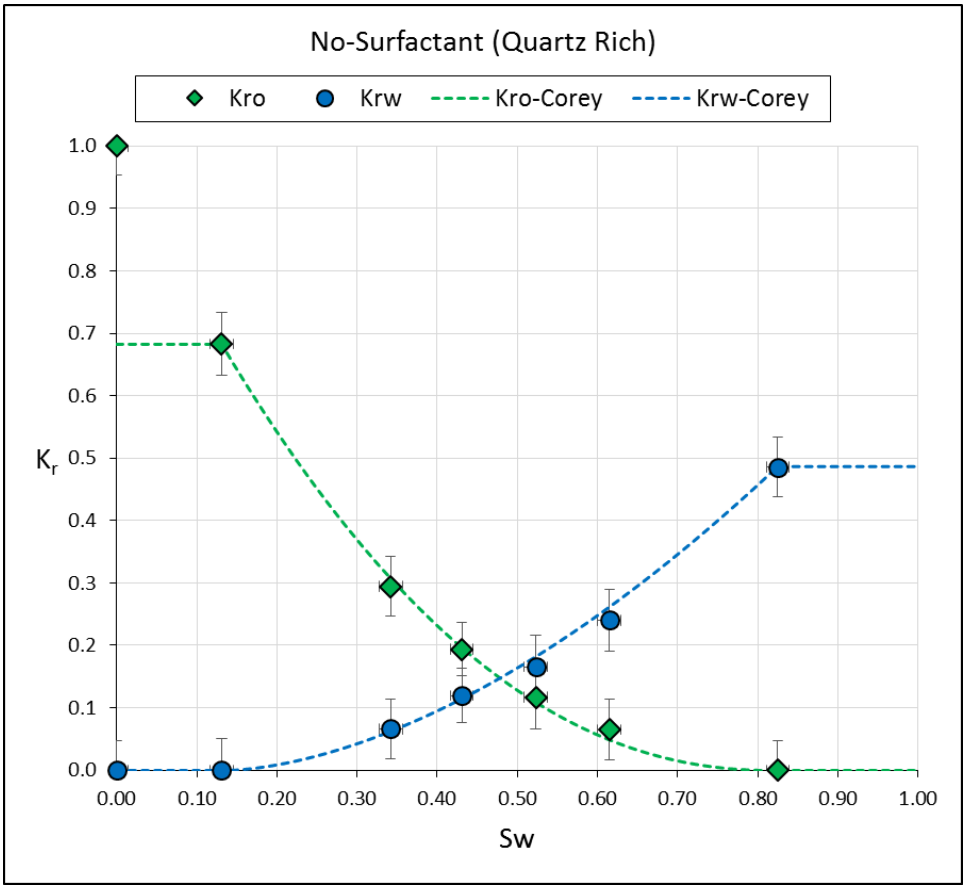

Fig. 3.2 – Calculated Fracture Relative Permeability Curve and Corey Fit for No-Surfactant Quartz Rich Test Specimen Pairing.

The second experiment for the quartz rich sample set was conducted using Surfactant A. The results are shown in **Fig. 3.3** and summarized in **Table 3.3**, and a summary of the calculated relative permeabilities are shown in **Table 3.4** and **Fig. 3.4**.

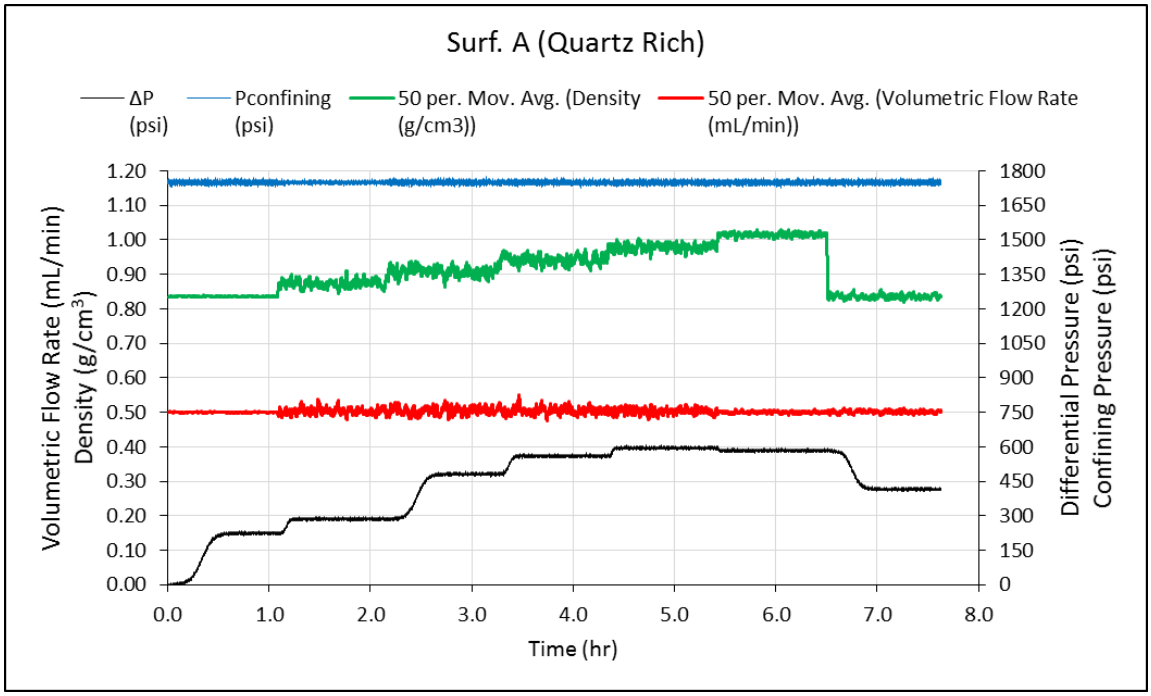

Fig. 3.3 – Recorded Data from Fracture Relative Permeability Test for Surf. A Quartz Rich Test Specimen Pairing.

Table 3.3 – Measured Fracture Relative Permeability Test Data for Surf. A Quartz Rich Test Specimen Pairing.

Surf. A (Quartz Rich) - Measured Data								
F_o	F_w	Q_{Total} (mL/min)	Q_{oil} (mL/min)	Q_{water} (mL/min)	P_{inlet} (psi)	ΔP_{ss} (psi)	P_{outlet} (psi)	P_{ave} (psi)
1.00	0.00	0.50	0.50	0.00	253	224	29	141
1.00	0.00	0.50	0.50	0.00	321	286	35	178
0.80	0.20	0.50	0.40	0.10	540	482	58	299
0.60	0.40	0.50	0.30	0.20	629	560	69	349
0.40	0.60	0.50	0.20	0.30	669	595	74	372
0.20	0.80	0.50	0.10	0.40	655	584	71	363
0.00	1.00	0.50	0.00	0.50	468	416	52	260

Table 3.4 – Calculated Fracture Relative Permeability Data for Surf. A Quartz Rich Test Specimen Pairing.

Surf. A (Quartz Rich) - Calculated Relative Permeability						
F_o	F_w	$S_{w\text{-}vol}$	K_{eo} (md)	K_{ew} (md)	K_{ro}	K_{rw}
1.00	0.00	0.00	250.67	0.00	1.00	0.00
1.00	0.00	0.13	185.28	0.00	0.74	0.00
0.80	0.20	0.41	76.34	17.81	0.30	0.07
0.60	0.40	0.51	47.03	30.65	0.19	0.12
0.40	0.60	0.62	28.95	43.27	0.12	0.17
0.20	0.80	0.69	14.86	58.78	0.06	0.23
0.00	1.00	0.85	0.00	103.15	0.00	0.41

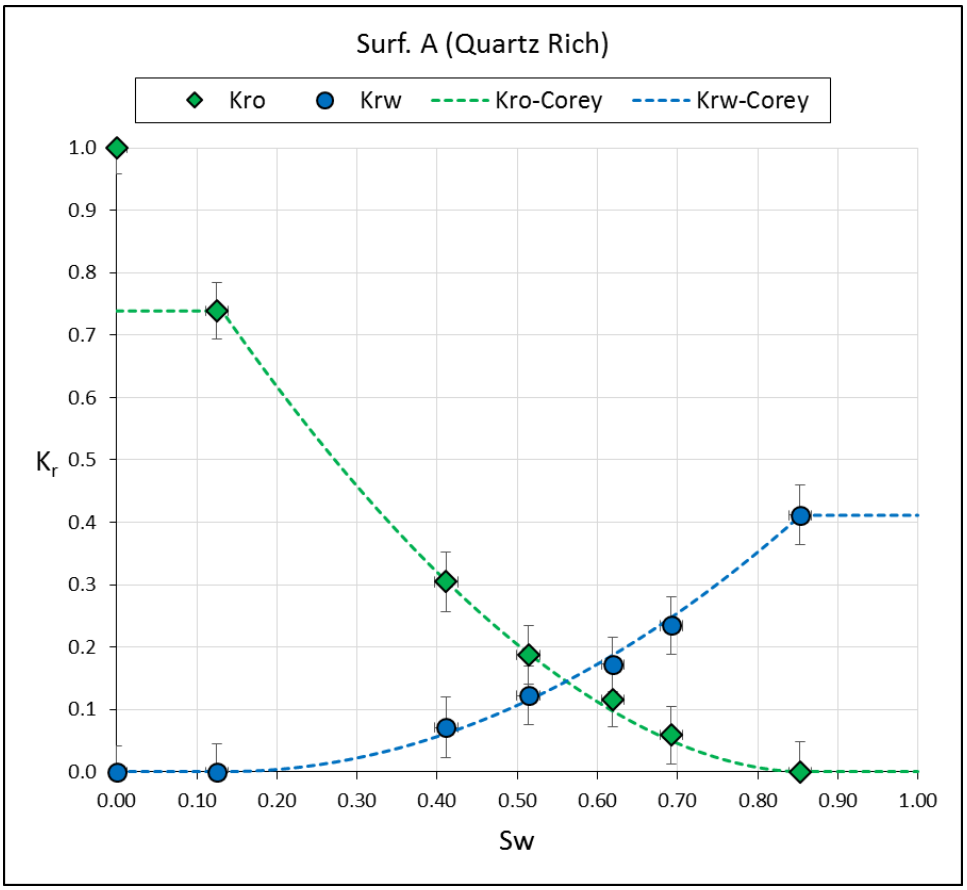

Fig. 3.4 – Calculated Fracture Relative Permeability Curve and Corey Fit for Surf. A Quartz Rich Test Specimen Pairing.

The third experiment for the quartz rich sample set was conducted using Surfactant B. The results are shown in **Fig. 3.5** and summarized in **Table 3.5**, and a summary of the calculated relative permeabilities are shown in **Table 3.6** and **Fig. 3.6**.

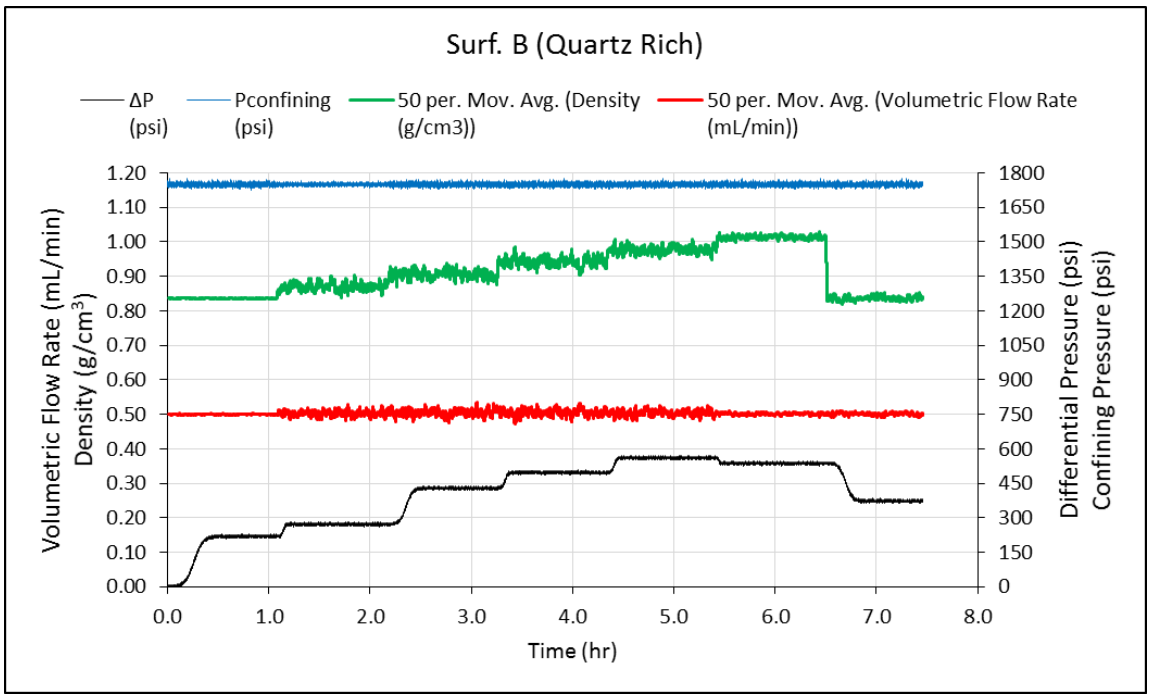

Fig. 3.5 – Recorded Data from Fracture Relative Permeability Test for Surf. B Quartz Rich Test Specimen Pairing.

Table 3.5 – Measured Fracture Relative Permeability Test Data for Surf. B Quartz Rich Test Specimen Pairing.

Surf. B (Quartz Rich) - Measured Data								
F_o	F_w	Q_{Total} (mL/min)	Q_{oil} (mL/min)	Q_{water} (mL/min)	P_{inlet} (psi)	ΔP_{ss} (psi)	P_{outlet} (psi)	P_{ave} (psi)
1.00	0.00	0.50	0.50	0.00	246	219	27	136
1.00	0.00	0.50	0.50	0.00	305	272	33	169
0.80	0.20	0.50	0.40	0.10	483	429	54	268
0.60	0.40	0.50	0.30	0.20	559	497	62	311
0.40	0.60	0.50	0.20	0.30	629	561	68	349
0.20	0.80	0.50	0.10	0.40	602	537	65	334
0.00	1.00	0.50	0.00	0.50	420	373	47	233

Table 3.6 – Calculated Fracture Relative Permeability Data for Surf. A Quartz Rich Test Specimen Pairing.

Surf. B (Quartz Rich) - Calculated Relative Permeability						
F_o	F_w	$S_{w\text{-}vol}$	K_{eo} (md)	K_{ew} (md)	K_{ro}	K_{rw}
1.00	0.00	0.00	258.63	0.00	1.00	0.00
1.00	0.00	0.12	197.36	0.00	0.76	0.00
0.80	0.20	0.37	88.53	20.01	0.34	0.08
0.60	0.40	0.47	54.92	34.54	0.21	0.13
0.40	0.60	0.58	31.32	45.90	0.12	0.18
0.20	0.80	0.67	16.58	63.93	0.06	0.25
0.00	1.00	0.85	0.00	115.05	0.00	0.44

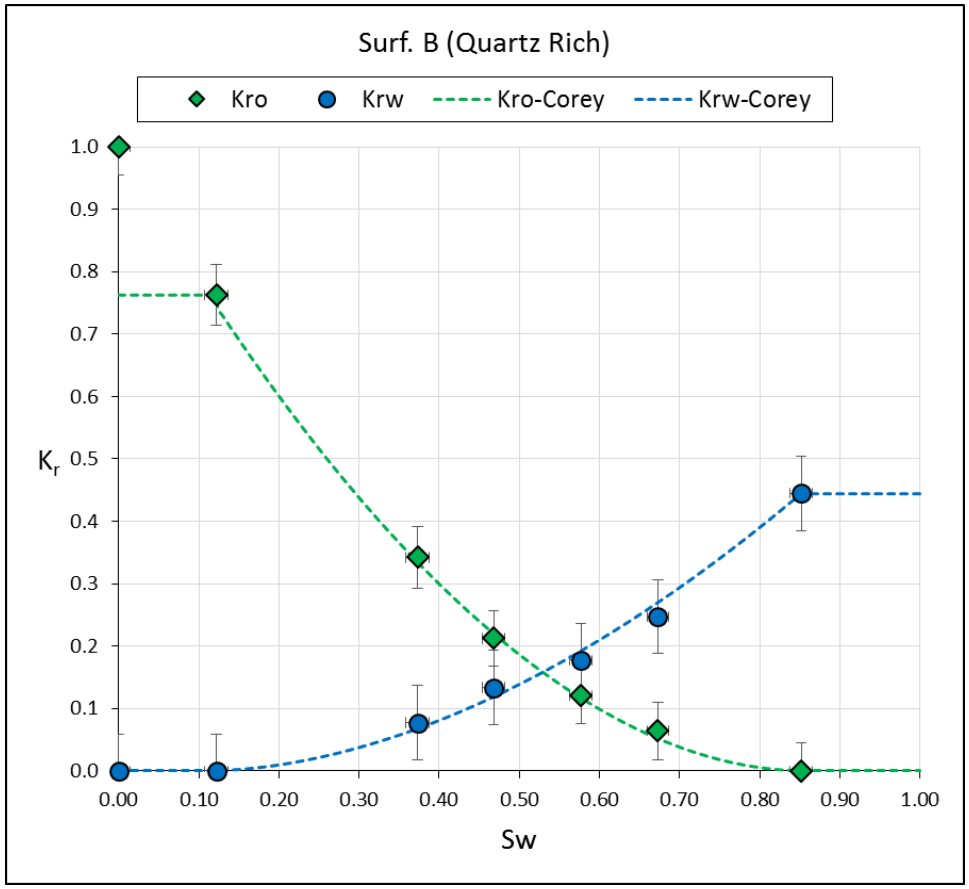

Fig. 3.6 – Calculated Fracture Relative Permeability Curve and Corey Fit for Surf. B Quartz Rich Test Specimen Pairing.

The fourth experiment for the quartz rich sample set was conducted using Surfactant C. The results are shown in **Fig. 3.7** and summarized in **Table 3.7**, and a summary of the calculated relative permeabilities are shown in **Table 3.8** and **Fig. 3.8**.

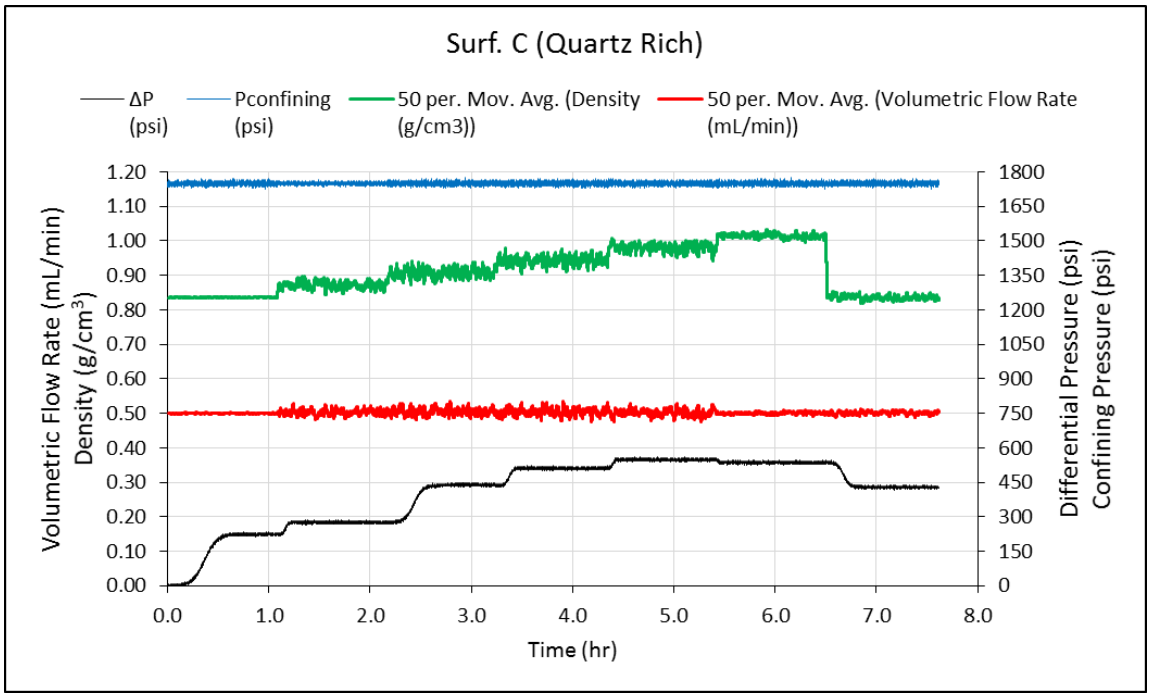

Fig. 3.7 – Recorded Data from Fracture Relative Permeability Test for Surf. C Quartz Rich Test Specimen Pairing.

Table 3.7 – Measured Fracture Relative Permeability Test Data for Surf. C Quartz Rich Test Specimen Pairing.

Surf. C (Quartz Rich) - Measured Data								
F_o	F_w	Q_{Total} (mL/min)	Q_{oil} (mL/min)	Q_{water} (mL/min)	P_{inlet} (psi)	ΔP_{ss} (psi)	P_{outlet} (psi)	P_{ave} (psi)
1.00	0.00	0.50	0.50	0.00	251	224	27	139
1.00	0.00	0.50	0.50	0.00	311	276	35	173
0.80	0.20	0.50	0.40	0.10	494	439	55	275
0.60	0.40	0.50	0.30	0.20	575	511	64	320
0.40	0.60	0.50	0.20	0.30	617	549	68	343
0.20	0.80	0.50	0.10	0.40	601	536	65	333
0.00	1.00	0.50	0.00	0.50	481	429	52	266

Table 3.8 – Calculated Fracture Relative Permeability Data for Surf. C Quartz Rich Test Specimen Pairing.

Surf. C (Quartz Rich) - Calculated Relative Permeability						
F_o	F_w	$S_{w\text{-}vol}$	K_{eo} (md)	K_{ew} (md)	K_{ro}	K_{rw}
1.00	0.00	0.00	251.48	0.00	1.00	0.00
1.00	0.00	0.13	193.36	0.00	0.77	0.00
0.80	0.20	0.43	85.92	19.55	0.34	0.08
0.60	0.40	0.54	52.96	33.59	0.21	0.13
0.40	0.60	0.63	32.17	46.90	0.13	0.19
0.20	0.80	0.74	16.62	64.05	0.07	0.25
0.00	1.00	0.85	0.00	100.03	0.00	0.40

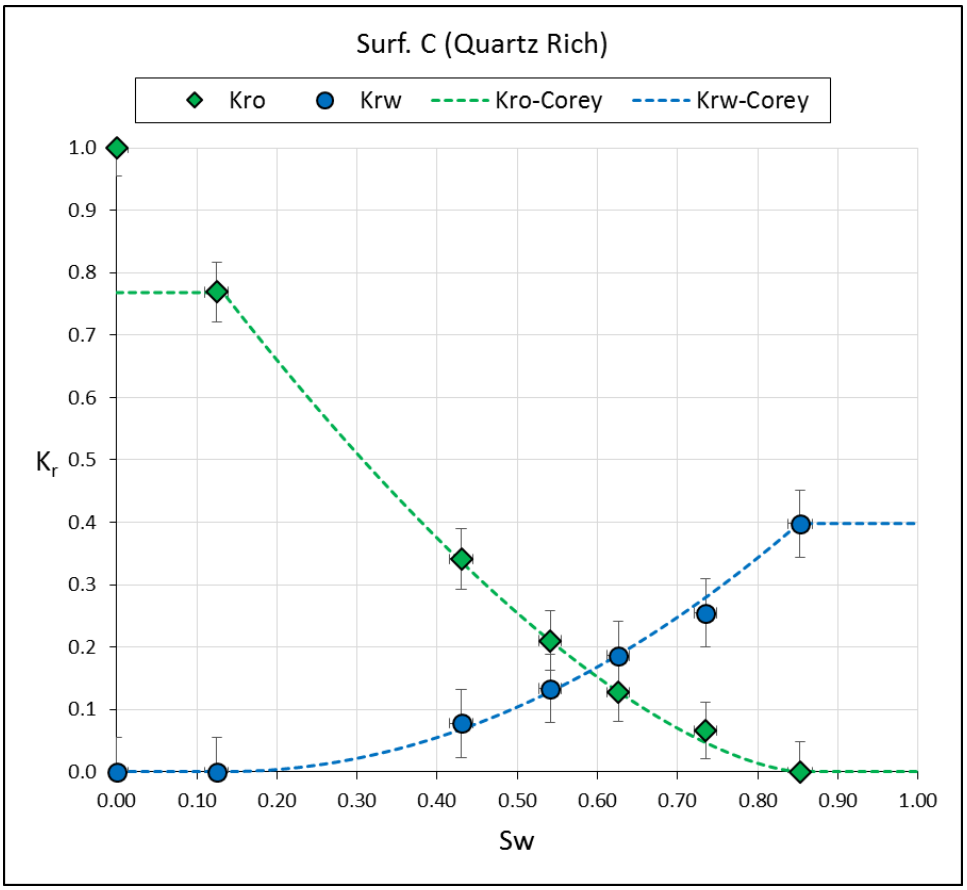

Fig. 3.8 – Calculated Fracture Relative Permeability Curve and Corey Fit for Surf. C Quartz Rich Test Specimen Pairing.

The fifth experiment for the quartz rich sample set was conducted using Surfactant D. The results are shown in **Fig. 3.9** and summarized in **Table 3.9**, and a summary of the calculated relative permeabilities are shown in **Table 3.10** and **Fig. 3.10**.

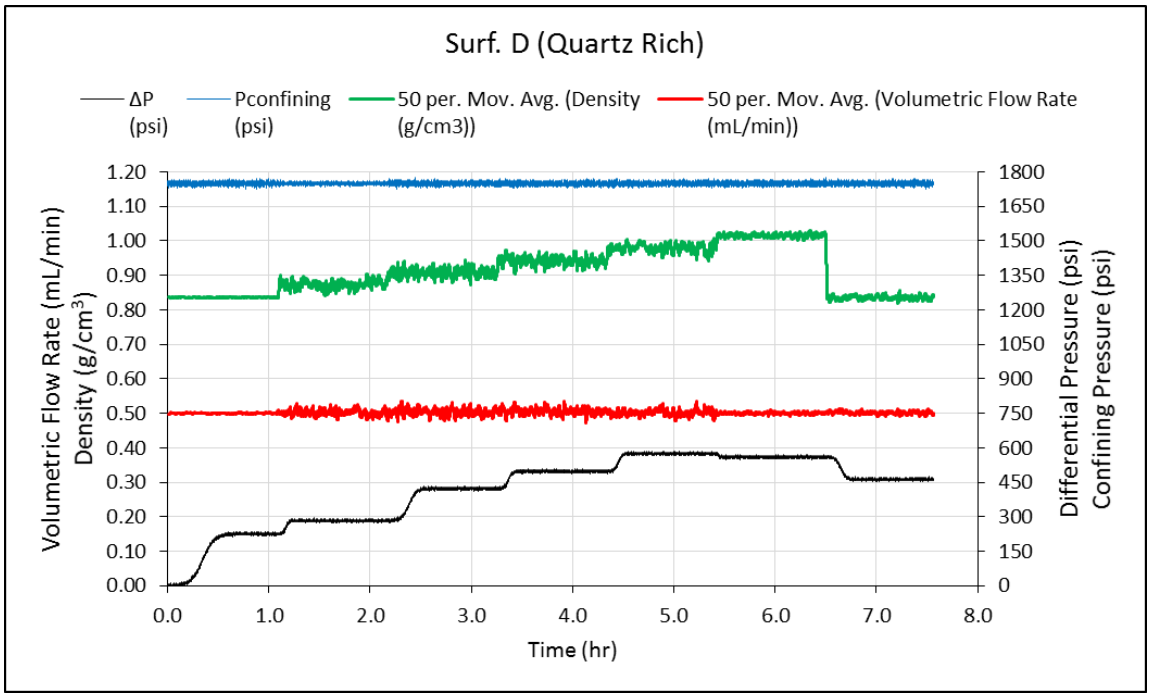

Fig. 3.9 – Recorded Data from Fracture Relative Permeability Test for Surf. D Quartz Rich Test Specimen Pairing.

Table 3.9 – Measured Fracture Relative Permeability Test Data for Surf. D Quartz Rich Test Specimen Pairing.

Surf. D (Quartz Rich) - Measured Data								
F_o	F_w	Q_{Total} (mL/min)	Q_{oil} (mL/min)	Q_{water} (mL/min)	P_{inlet} (psi)	ΔP_{ss} (psi)	P_{outlet} (psi)	P_{ave} (psi)
1.00	0.00	0.50	0.50	0.00	256	226	30	143
1.00	0.00	0.50	0.50	0.00	318	283	35	177
0.80	0.20	0.50	0.40	0.10	476	423	53	265
0.60	0.40	0.50	0.30	0.20	559	498	61	310
0.40	0.60	0.50	0.20	0.30	646	575	71	359
0.20	0.80	0.50	0.10	0.40	628	560	68	348
0.00	1.00	0.50	0.00	0.50	520	463	57	289

Table 3.10 – Calculated Fracture Relative Permeability Data for Surf. D Quartz Rich Test Specimen Pairing.

Surf. D (Quartz Rich) - Calculated Relative Permeability						
F_o	F_w	$S_{w\text{-}vol}$	K_{eo} (md)	K_{ew} (md)	K_{ro}	K_{rw}
1.00	0.00	0.00	247.79	0.00	1.00	0.00
1.00	0.00	0.16	187.58	0.00	0.76	0.00
0.80	0.20	0.42	90.11	20.29	0.36	0.08
0.60	0.40	0.54	54.82	34.47	0.22	0.14
0.40	0.60	0.65	30.29	44.78	0.12	0.18
0.20	0.80	0.75	15.70	61.30	0.06	0.25
0.00	1.00	0.87	0.00	92.68	0.00	0.37

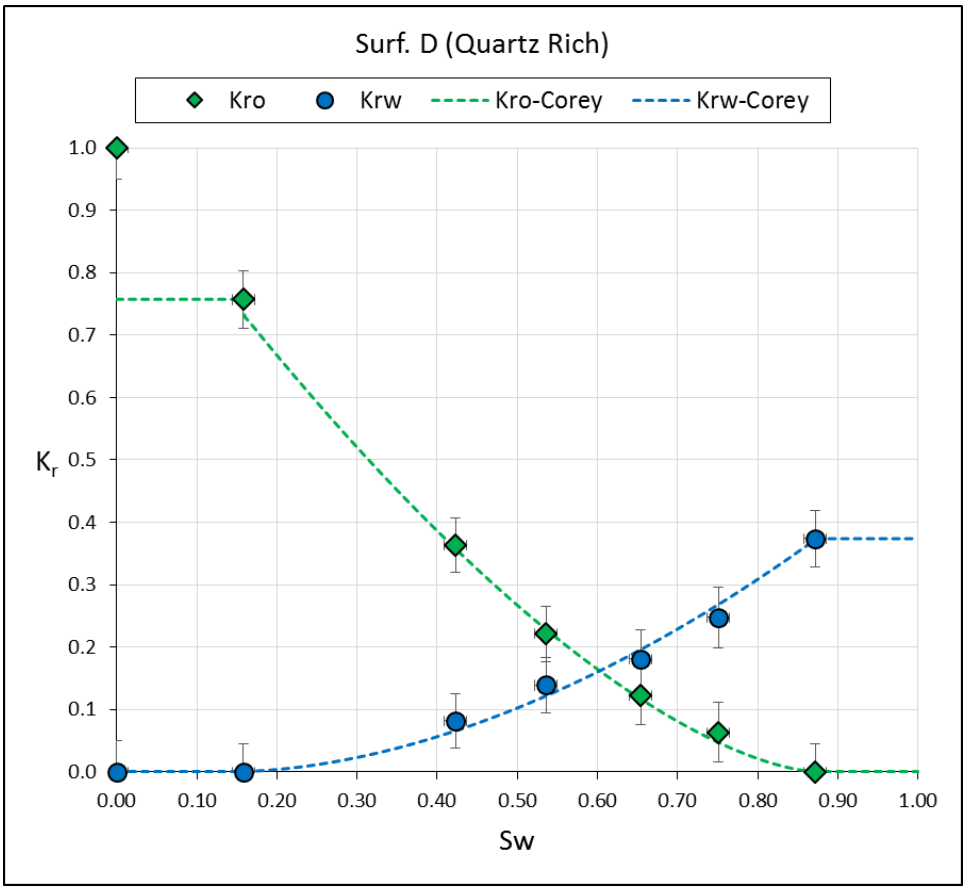

Fig. 3.10 – Calculated Fracture Relative Permeability Curve and Corey Fit for Surf. D Quartz Rich Test Specimen Pairing.

3.4 Carbonate Rich Sample Set Test Results

The carbonate rich samples were tested in five different experiments. The first test conducted with no surfactant is shown in **Fig. 3.11** and summarized in **Table 3.11**, and a summary of the calculated relative permeabilities are shown in **Table 3.12** and **Fig. 3.12**.

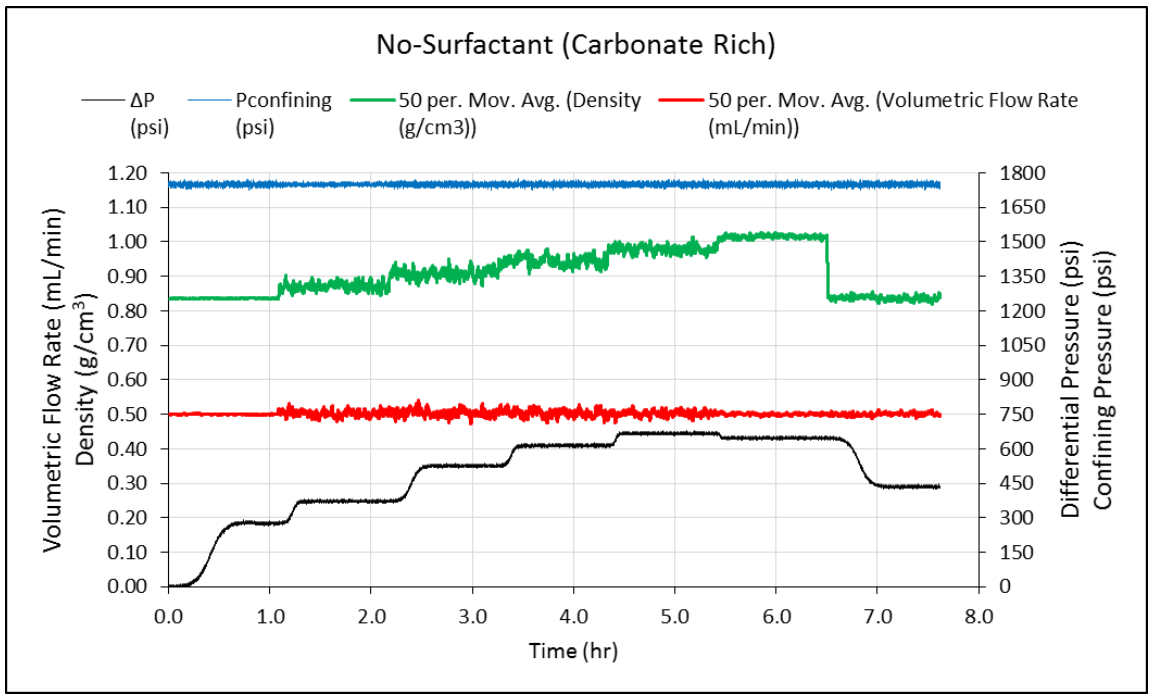

Fig. 3.11 – Recorded Data from Fracture Relative Permeability Test for No-Surfactant Carbonate Rich Test Specimen Pairing.

Table 3.11 – Measured Fracture Relative Permeability Test Data for No-Surfactant Carbonate Rich Test Specimen Pairing.

No-Surfactant (Carbonate Rich) - Measured Data								
F_o	F_w	Q_{Total} (mL/min)	Q_{oil} (mL/min)	Q_{water} (mL/min)	P_{inlet} (psi)	ΔP_{ss} (psi)	P_{outlet} (psi)	P_{ave} (psi)
1.00	0.00	0.50	0.50	0.00	312	276	36	174
1.00	0.00	0.50	0.50	0.00	419	372	47	233
0.80	0.20	0.50	0.40	0.10	590	526	64	327
0.60	0.40	0.50	0.30	0.20	691	614	77	384
0.40	0.60	0.50	0.20	0.30	749	667	82	415
0.20	0.80	0.50	0.10	0.40	726	647	79	403
0.00	1.00	0.50	0.00	0.50	488	435	53	271

Table 3.12 – Calculated Fracture Relative Permeability Data for No-Surfactant Carbonate Rich Test Specimen Pairing.

No-Surfactant (Carbonate Rich) - Calculated Relative Permeability						
F_o	F_w	$S_{w\text{-}vol}$	K_{eo} (md)	K_{ew} (md)	K_{ro}	K_{rw}
1.00	0.00	0.00	193.29	0.00	1.00	0.00
1.00	0.00	0.12	132.65	0.00	0.69	0.00
0.80	0.20	0.27	68.11	16.32	0.35	0.08
0.60	0.40	0.37	41.66	27.96	0.22	0.14
0.40	0.60	0.47	24.92	38.60	0.13	0.20
0.20	0.80	0.57	12.98	53.06	0.07	0.27
0.00	1.00	0.82	0.00	98.65	0.00	0.51

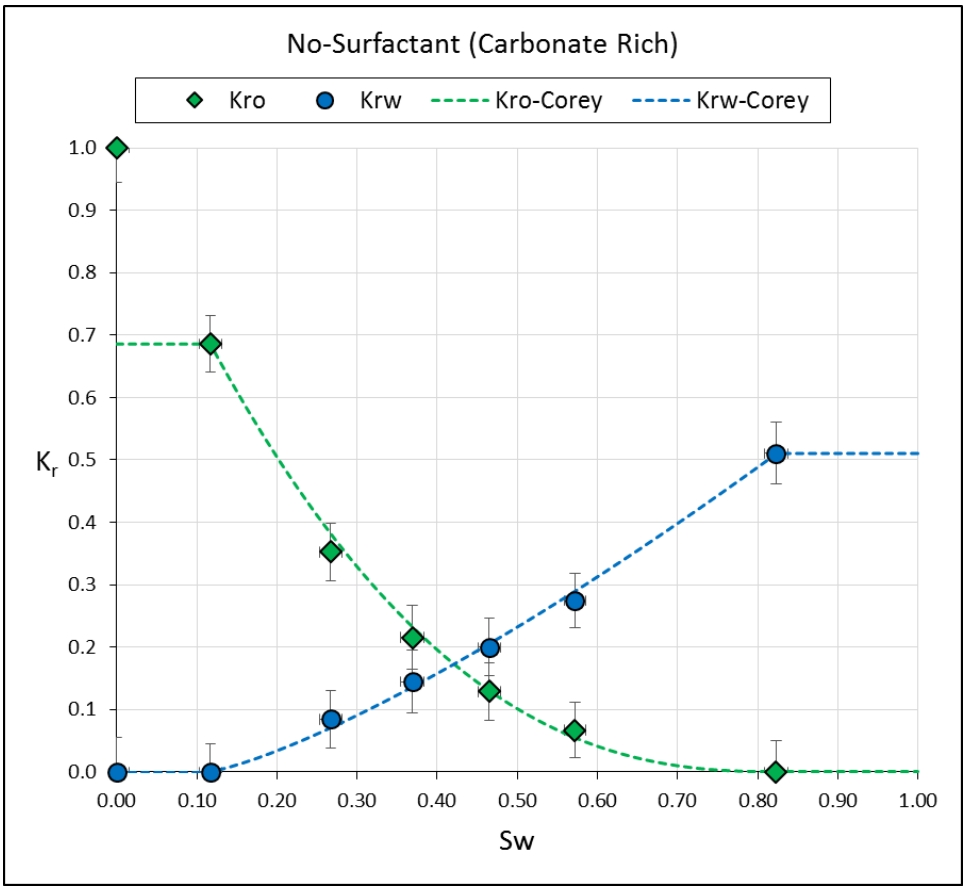

Fig. 3.12 – Calculated Fracture Relative Permeability Curve and Corey Fit for No-Surfactant Carbonate Rich Test Specimen Pairing.

The second experiment for the carbonate rich sample set was conducted using Surfactant A. The results are shown in **Fig. 3.13** and summarized in **Table 3.13**, and a summary of the calculated relative permeabilities are shown in **Table 3.14** and **Fig. 3.14**.

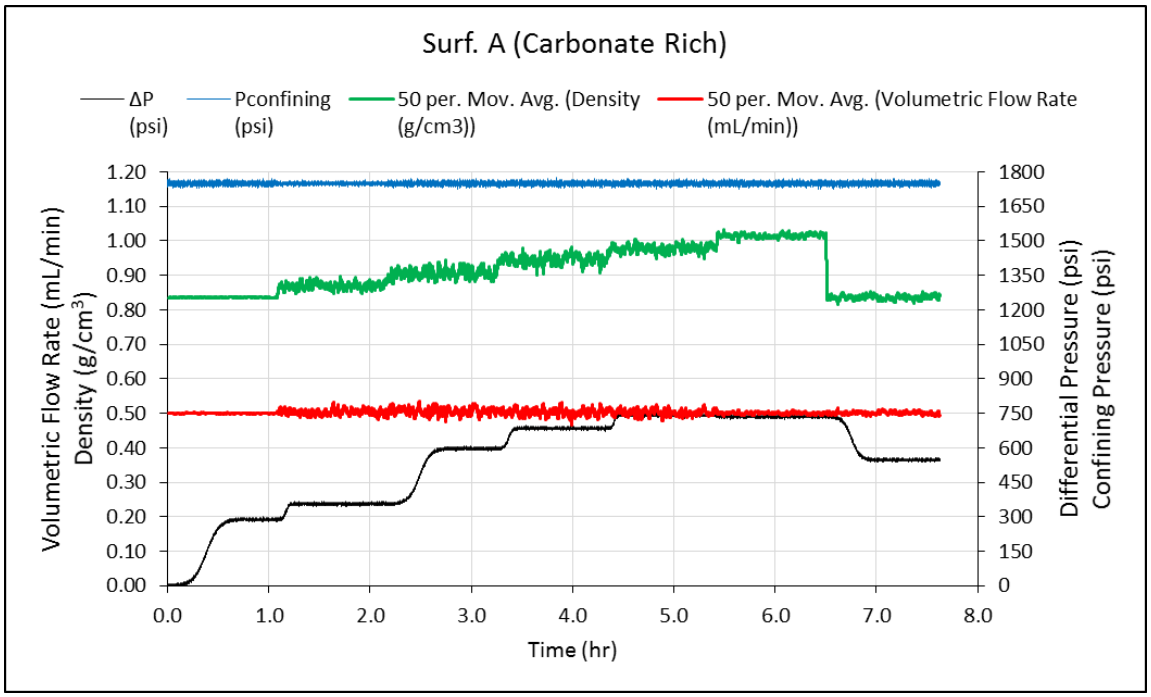

Fig. 3.13 – Recorded Data from Fracture Relative Permeability Test for Surf. A Carbonate Rich Test Specimen Pairing.

Table 3.13 – Measured Fracture Relative Permeability Test Data for Surf. A Carbonate Rich Test Specimen Pairing.

Surf. A (Carbonbate Rich) - Measured Data								
F_o	F_w	Q_{Total} (mL/min)	Q_{oil} (mL/min)	Q_{water} (mL/min)	P_{inlet} (psi)	ΔP_{ss} (psi)	P_{outlet} (psi)	P_{ave} (psi)
1.00	0.00	0.50	0.50	0.00	324	288	36	180
1.00	0.00	0.50	0.50	0.00	401	356	45	223
0.80	0.20	0.50	0.40	0.10	669	597	72	371
0.60	0.40	0.50	0.30	0.20	769	685	84	427
0.40	0.60	0.50	0.20	0.30	832	742	90	461
0.20	0.80	0.50	0.10	0.40	826	736	90	458
0.00	1.00	0.50	0.00	0.50	615	548	67	341

Table 3.14 – Calculated Fracture Relative Permeability Data for Surf. A Carbonate Rich Test Specimen Pairing.

Surf. A (Carbonate Rich) - Calculated Relative Permeability						
F_o	F_w	$S_{w\text{-}vol}$	K_{eo} (md)	K_{ew} (md)	K_{ro}	K_{rw}
1.00	0.00	0.00	183.42	0.00	1.00	0.00
1.00	0.00	0.11	140.28	0.00	0.76	0.00
0.80	0.20	0.39	57.76	14.38	0.31	0.08
0.60	0.40	0.49	36.09	25.06	0.20	0.14
0.40	0.60	0.58	21.65	34.70	0.12	0.19
0.20	0.80	0.68	10.93	46.64	0.06	0.25
0.00	1.00	0.86	0.00	78.31	0.00	0.43

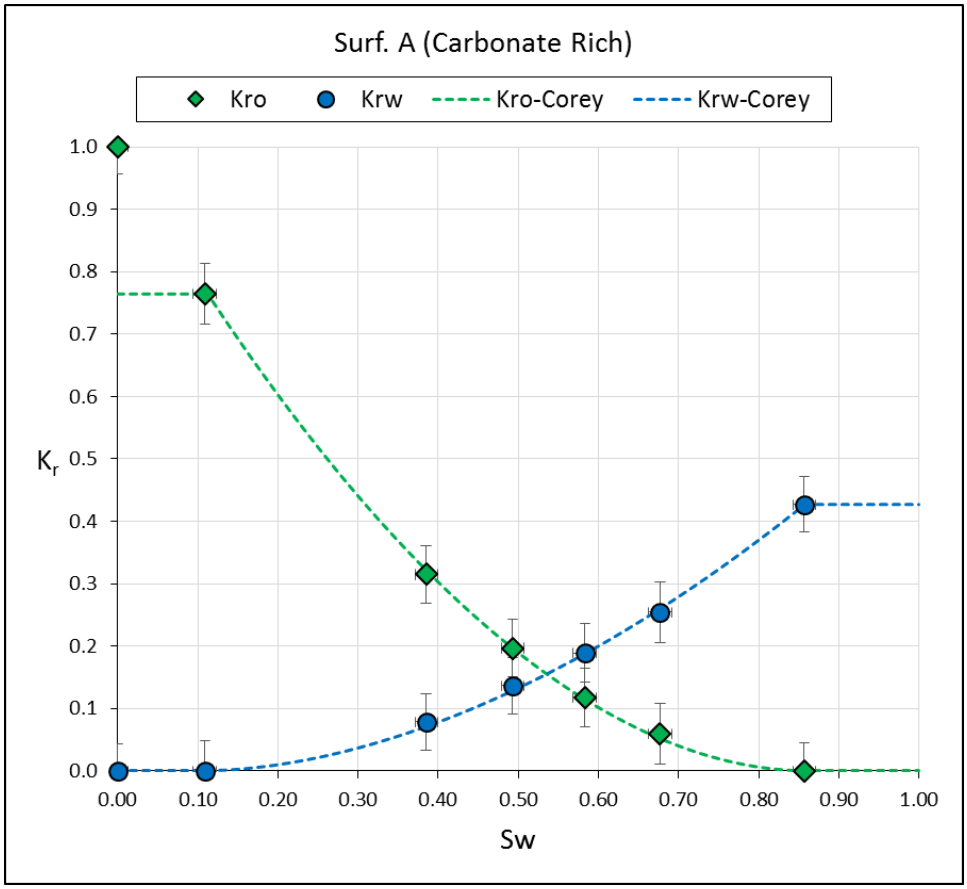

Fig. 3.14 – Calculated Fracture Relative Permeability Curve and Corey Fit for Surf. A Carbonate Rich Test Specimen Pairing.

The third experiment for the carbonate rich sample set was conducted using Surfactant B. The results are shown in **Fig. 3.15** and summarized in **Table 3.15**, and a summary of the calculated relative permeabilities are shown in **Table 3.16** and **Fig. 3.16**.

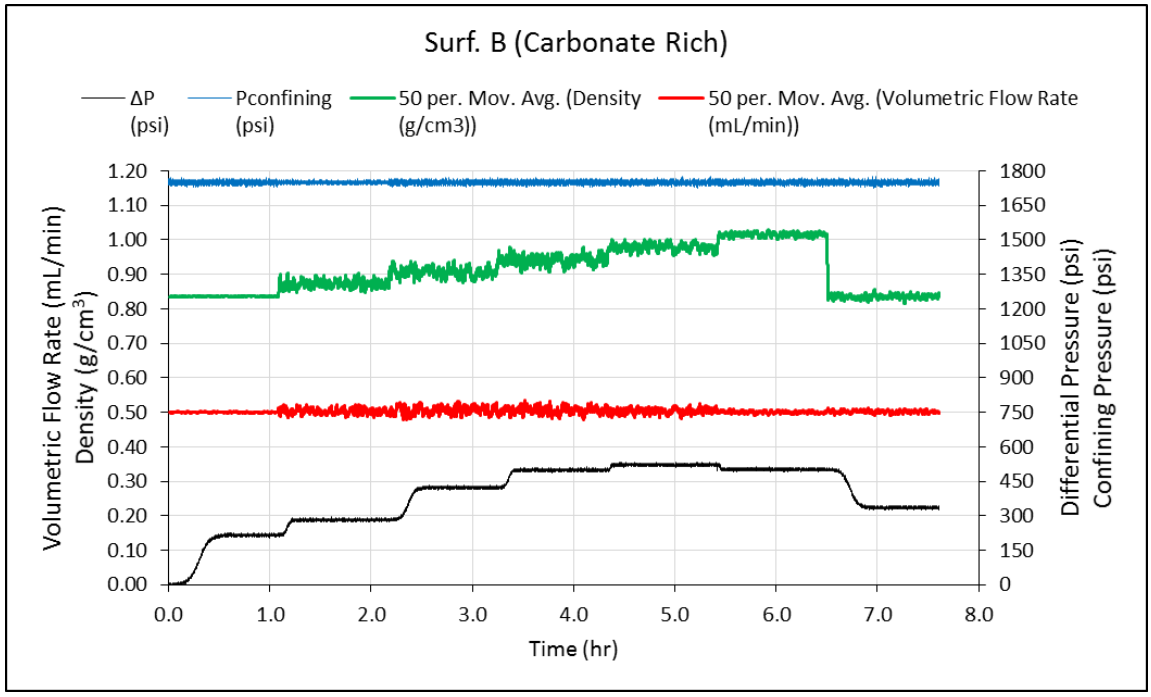

Fig. 3.15 – Recorded Data from Fracture Relative Permeability Test for Surf. B Carbonate Rich Test Specimen Pairing.

Table 3.15 – Measured Fracture Relative Permeability Test Data for Surf. B Carbonate Rich Test Specimen Pairing.

Surf. B (Carbonate Rich) - Measured Data								
F_o	F_w	Q_{Total} (mL/min)	Q_{oil} (mL/min)	Q_{water} (mL/min)	P_{inlet} (psi)	ΔP_{ss} (psi)	P_{outlet} (psi)	P_{ave} (psi)
1.00	0.00	0.50	0.50	0.00	244	216	28	136
1.00	0.00	0.50	0.50	0.00	319	282	37	178
0.80	0.20	0.50	0.40	0.10	476	423	53	265
0.60	0.40	0.50	0.30	0.20	560	499	61	311
0.40	0.60	0.50	0.20	0.30	586	522	64	325
0.20	0.80	0.50	0.10	0.40	565	502	63	314
0.00	1.00	0.50	0.00	0.50	377	336	41	209

Table 3.16 – Calculated Fracture Relative Permeability Data for Surf. B Carbonate Rich Test Specimen Pairing.

Surf. B (Carbonate Rich) - Calculated Relative Permeability						
F_o	F_w	$S_{w\text{-}vol}$	K_{eo} (md)	K_{ew} (md)	K_{ro}	K_{rw}
1.00	0.00	0.00	262.02	0.00	1.00	0.00
1.00	0.00	0.13	188.02	0.00	0.72	0.00
0.80	0.20	0.32	90.09	20.29	0.34	0.08
0.60	0.40	0.43	54.69	34.40	0.21	0.13
0.40	0.60	0.51	34.39	49.32	0.13	0.19
0.20	0.80	0.61	18.06	68.39	0.07	0.26
0.00	1.00	0.84	0.00	127.71	0.00	0.49

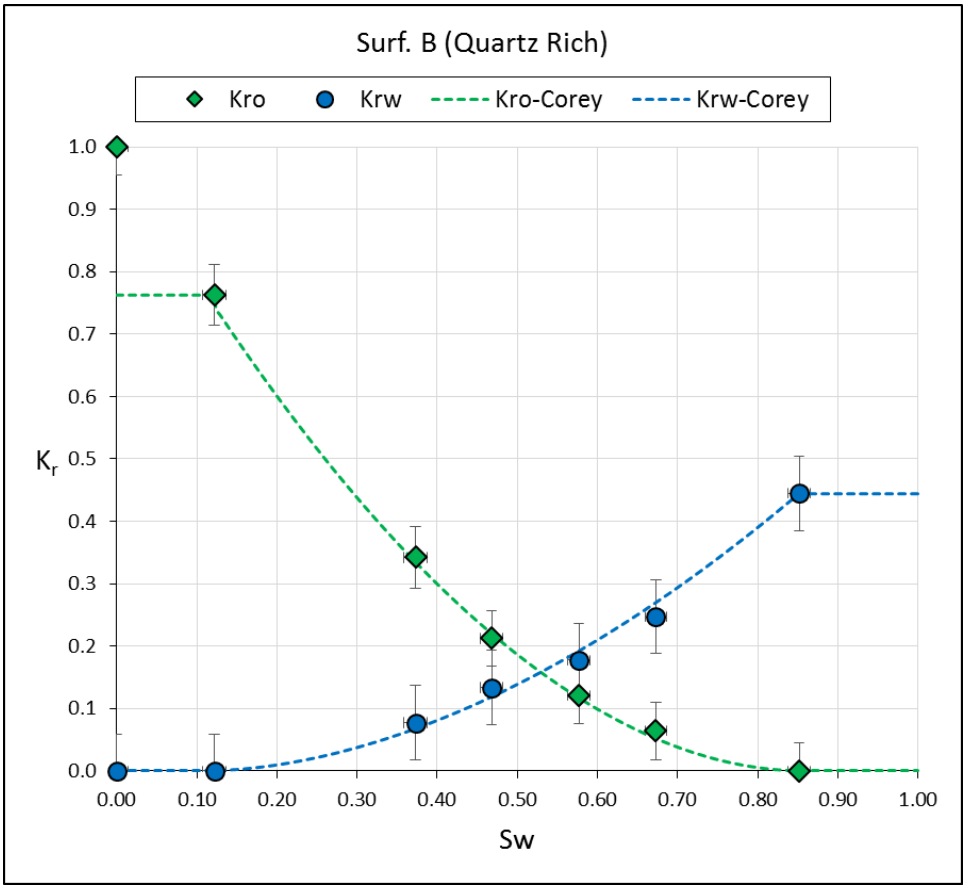

Fig. 3.16 – Calculated Fracture Relative Permeability Curve and Corey Fit for Surf. B Carbonate Rich Test Specimen Pairing.

The fourth experiment for the carbonate rich sample set was conducted using Surfactant C. The results are shown in **Fig. 3.17** and summarized in **Table 3.17**, and a summary of the calculated relative permeabilities are shown in **Table 3.18** and **Fig. 3.18**.

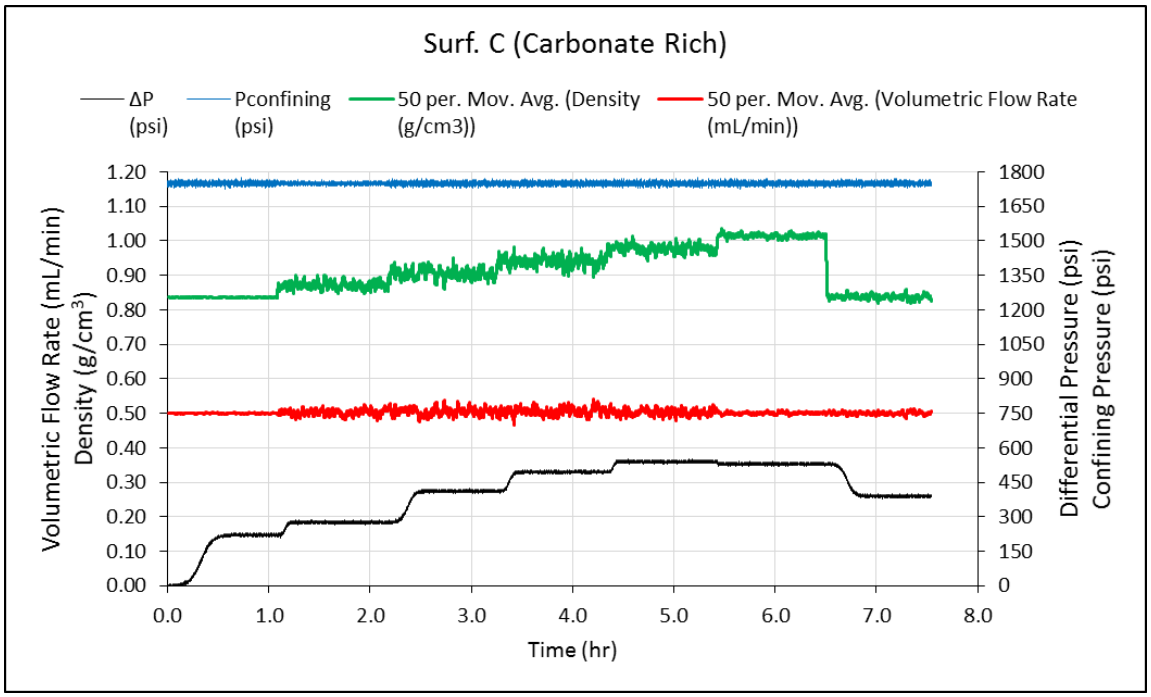

Fig. 3.17 – Recorded Data from Fracture Relative Permeability Test for Surf. C Carbonate Rich Test Specimen Pairing.

Table 3.17 – Measured Fracture Relative Permeability Test Data for Surf. C Carbonate Rich Test Specimen Pairing.

Surf. C (Carbonate Rich) - Measured Data								
F_o	F_w	Q_{Total} (mL/min)	Q_{oil} (mL/min)	Q_{water} (mL/min)	P_{inlet} (psi)	ΔP_{ss} (psi)	P_{outlet} (psi)	P_{ave} (psi)
1.00	0.00	0.50	0.50	0.00	249	221	28	138
1.00	0.00	0.50	0.50	0.00	312	276	36	174
0.80	0.20	0.50	0.40	0.10	464	412	52	258
0.60	0.40	0.50	0.30	0.20	555	495	60	307
0.40	0.60	0.50	0.20	0.30	606	540	66	336
0.20	0.80	0.50	0.10	0.40	595	530	65	330
0.00	1.00	0.50	0.00	0.50	438	390	48	243

Table 3.18 – Calculated Fracture Relative Permeability Data for Surf. C Carbonate Rich Test Specimen Pairing.

Surf. C (Carbonate Rich) - Calculated Relative Permeability						
F_o	F_w	$S_{w\text{-}vol}$	K_{eo} (md)	K_{ew} (md)	K_{ro}	K_{rw}
1.00	0.00	0.00	255.19	0.00	1.00	0.00
1.00	0.00	0.13	193.17	0.00	0.76	0.00
0.80	0.20	0.38	93.16	20.83	0.37	0.08
0.60	0.40	0.51	55.31	34.68	0.22	0.14
0.40	0.60	0.60	32.91	47.68	0.13	0.19
0.20	0.80	0.68	16.86	64.77	0.07	0.25
0.00	1.00	0.85	0.00	110.03	0.00	0.43

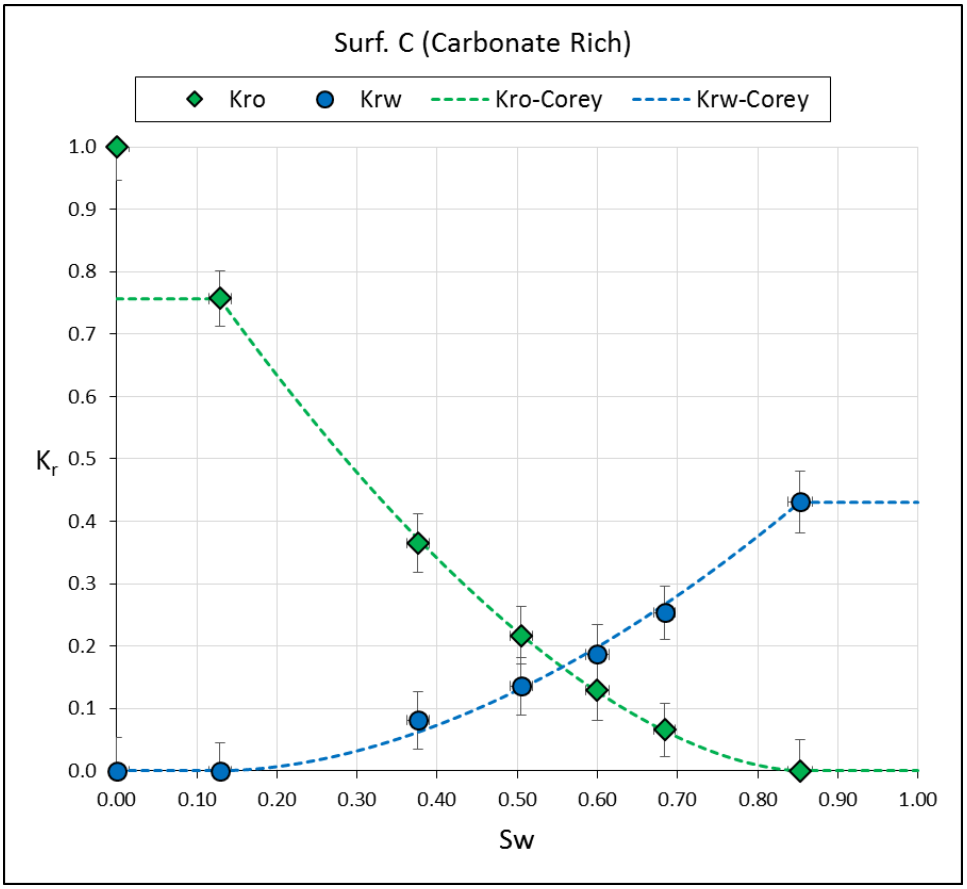

Fig. 3.18 – Calculated Fracture Relative Permeability Curve and Corey Fit for Surf. B Carbonate Rich Test Specimen Pairing.

The fifth experiment for the carbonate rich sample set was conducted using Surfactant D. The results are shown in **Fig. 3.19** and summarized in **Table 3.19**, and a summary of the calculated relative permeabilities are shown in **Table 3.20** and **Fig. 3.20**.

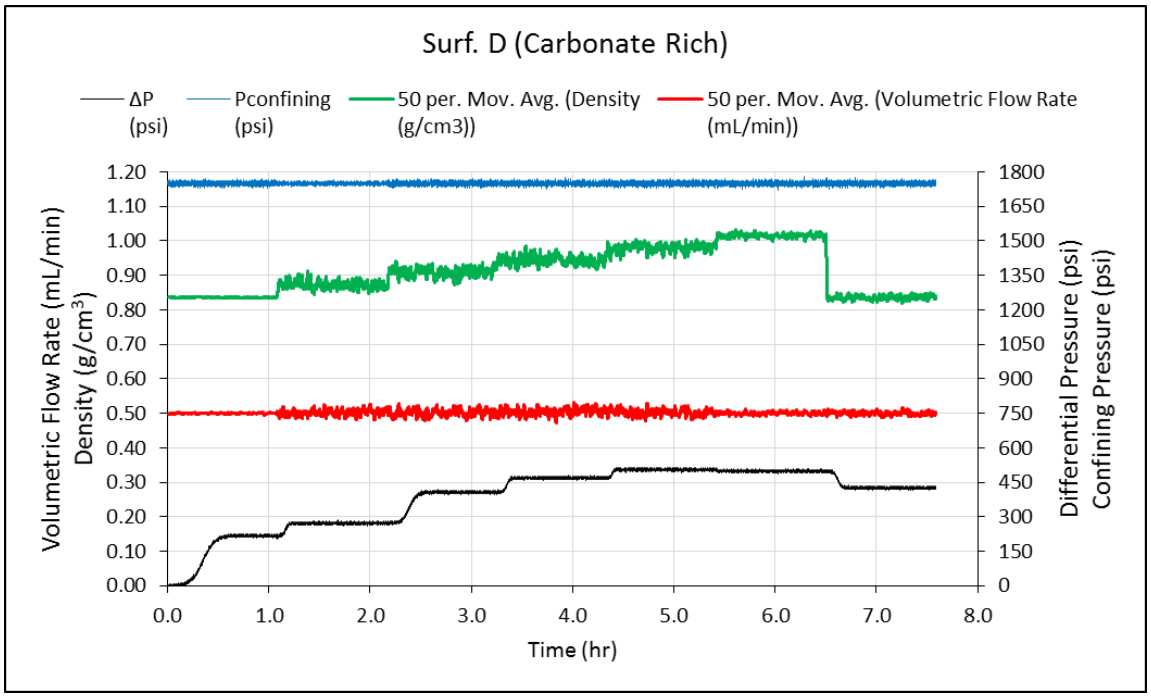

Fig. 3.19 – Recorded Data from Fracture Relative Permeability Test for Surf. D Carbonate Rich Test Specimen Pairing.

Table 3.19 – Measured Fracture Relative Permeability Test Data for Surf. D Carbonate Rich Test Specimen Pairing.

Surf. D (Carbonate Rich) - Measured Data								
F_o	F_w	Q_{Total} (mL/min)	Q_{oil} (mL/min)	Q_{water} (mL/min)	P_{inlet} (psi)	ΔP_{ss} (psi)	P_{outlet} (psi)	P_{ave} (psi)
1.00	0.00	0.50	0.50	0.00	246	218	28	137
1.00	0.00	0.50	0.50	0.00	307	272	35	171
0.80	0.20	0.50	0.40	0.10	456	407	49	253
0.60	0.40	0.50	0.30	0.20	527	469	58	293
0.40	0.60	0.50	0.20	0.30	567	505	62	314
0.20	0.80	0.50	0.10	0.40	559	499	60	310
0.00	1.00	0.50	0.00	0.50	478	426	52	265

Table 3.20 – Calculated Fracture Relative Permeability Data for Surf. D Carbonate Rich Test Specimen Pairing.

Surf. D (Carbonate Rich) - Calculated Relative Permeability						
F_o	F_w	$S_{w\text{-}vol}$	K_{eo} (md)	K_{ew} (md)	K_{ro}	K_{rw}
1.00	0.00	0.00	259.18	0.00	1.00	0.00
1.00	0.00	0.14	196.90	0.00	0.76	0.00
0.80	0.20	0.41	94.89	21.09	0.37	0.08
0.60	0.40	0.53	59.21	36.60	0.23	0.14
0.40	0.60	0.64	35.91	50.98	0.14	0.20
0.20	0.80	0.74	18.25	68.80	0.07	0.27
0.00	1.00	0.88	0.00	100.73	0.00	0.39

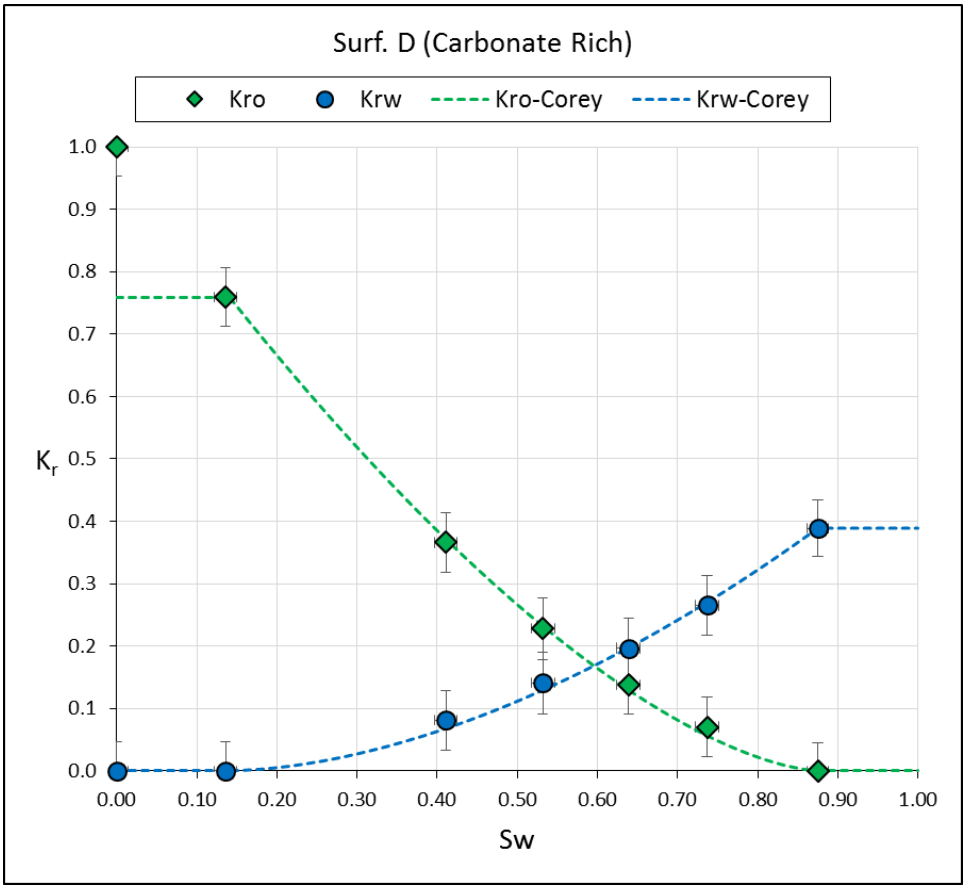

Fig. 3.20 – Calculated Fracture Relative Permeability Curve and Corey Fit for Surf. D Carbonate Rich Test Specimen Pairing.

3.5 Quartz Rich Test Results Summary and Discussion

The relative permeability test results for the quartz rich samples presented in Section 3.3 are summarized in this section. The fracture relative permeability endpoint saturations (namely the irreducible water saturation and the residual oil saturation), are plotted as a function of each fluid system properties (namely the product of the interfacial tension and the cosine of the contact angle), as shown in **Fig. 3.21**. It can be observed that there is an inverse relationship between the residual oil saturation and the product of the surfactant properties. The irreducible water saturation did not show a relationship to the fluid system properties.

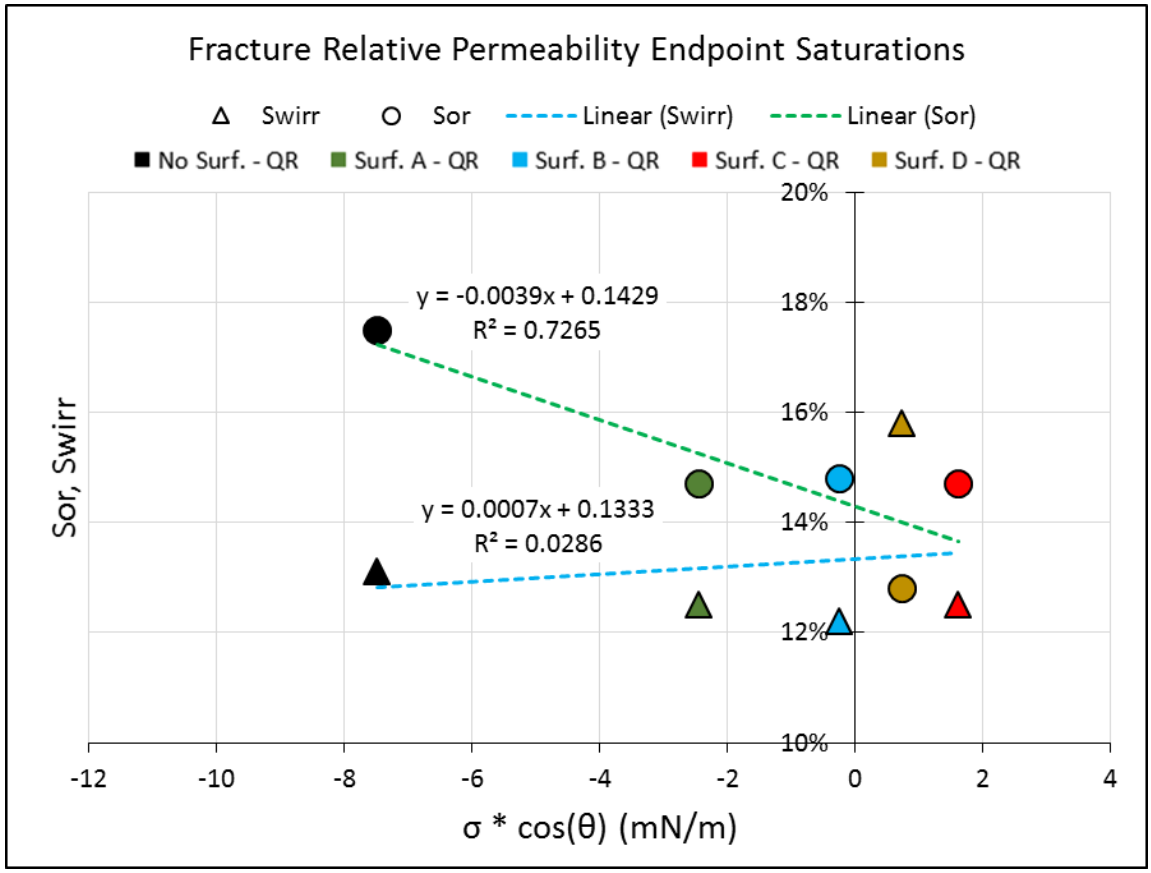

Fig. 3.21 – Quartz Rich Fracture Relative Permeability Endpoint Saturations Plotted as a Function of the Product of Interfacial Tension (σ) and the Cosine of Contact Angle (cos(θ)).

The fracture endpoint relative permeabilities (namely the relative permeability to oil at irreducible water saturation, and the relative permeability to water at residual oil saturation) are plotted as a function of each fluid system properties (namely the product of the interfacial tension and the cosine of the contact angle), as shown in **Fig. 3.22**.

It can be observed that the relative permeability to oil at irreducible water has a direct relationship to the product of the fluid system properties, while the relative permeability to water shows an inverse relationship to the same. An increase in the relative permeability to oil, and a decrease in the relative permeability to water is desirable for improving oil production as is further discussed in Section 5.

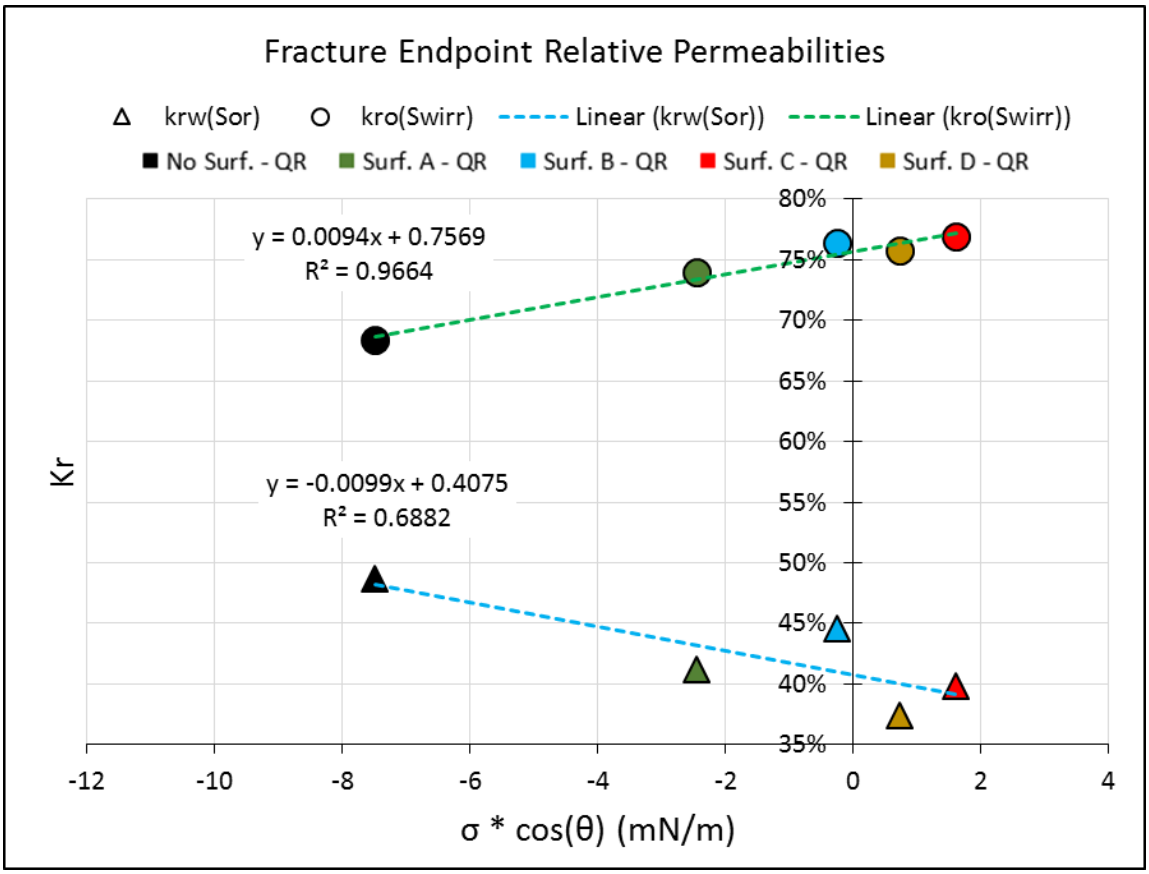

Fig. 3.22 – Quartz Rich Fracture Endpoint Relative Permeabilities Plotted as a Function of the Product of Interfacial Tension (σ) and the Cosine of Contact Angle (cos(θ)).

The fracture relative permeability crossing points (defined as the water saturation in the fracture at which the relative permeability to oil and the relative permeability to water have an equal value), are plotted as a function of the product of fluid system properties in **Fig. 3.23**. There is a direct relationship between the product of the fluid system properties and an increase in the relative permeability crossing points. An increase in crossing points indicates a change in wettability from oil-wet towards a water-wet system. Overall, a positively increasing product of fluid system properties (interfacial tension and cosine of contact angle), leads to an increase in relative permeability to oil, a decrease in relative permeability to water, and a decrease in residual oil saturation.

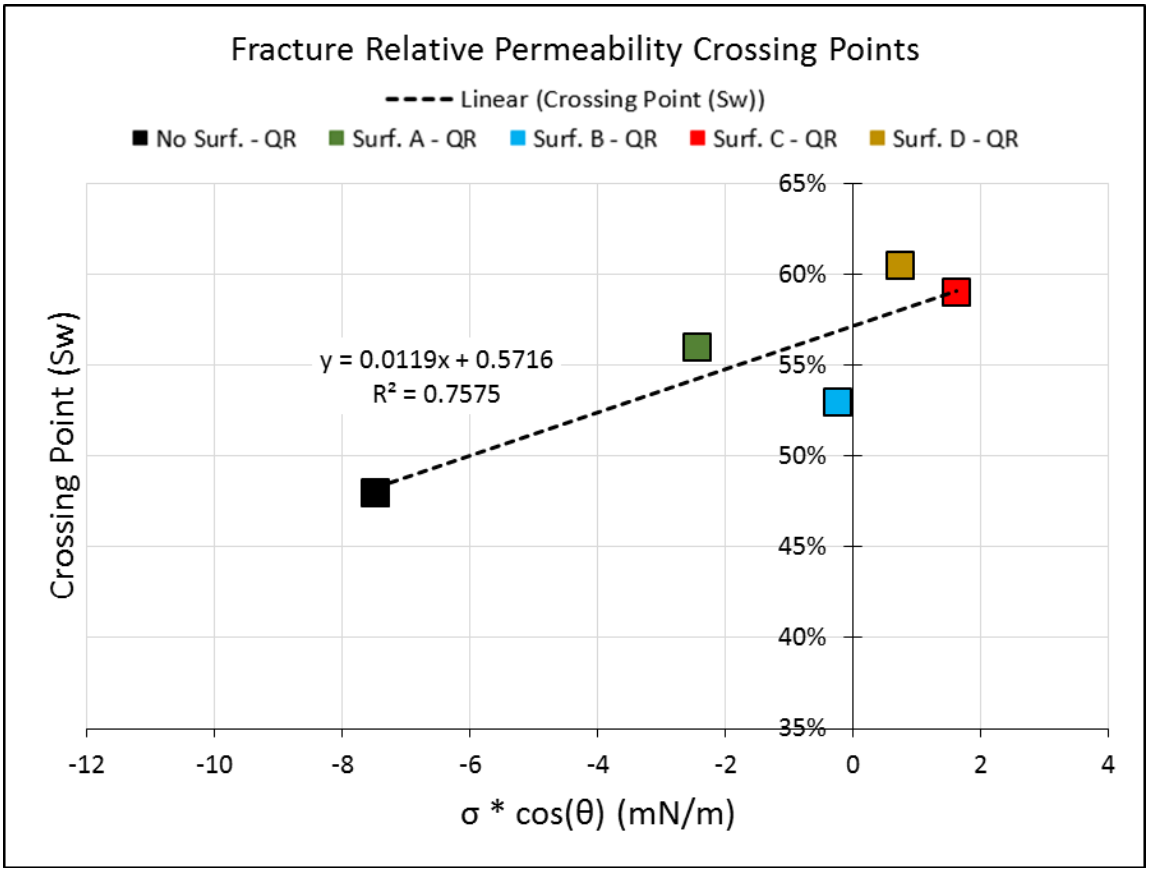

Fig. 3.23 – Quartz Rich Fracture Relative Permeability Crossing Points (Sw) Plotted as a Function of the Product of Interfacial Tension (σ) and the Cosine of Contact Angle (cos(θ)).

3.6 Carbonate Rich Test Results Summary and Discussion

The relative permeability test results for the carbonate rich samples presented in Section 3.4 are summarized in this section. The fracture relative permeability endpoint saturations are plotted as a function of each fluid system properties as shown in **Fig. 3.24**. Similarly to the quartz rich results, it can be observed that there is an inverse relationship between the residual oil saturation and the product of the surfactant properties. However, for the carbonate rich experiments, the irreducible water saturation showed a weak direct relationship to the product of fluid system properties.

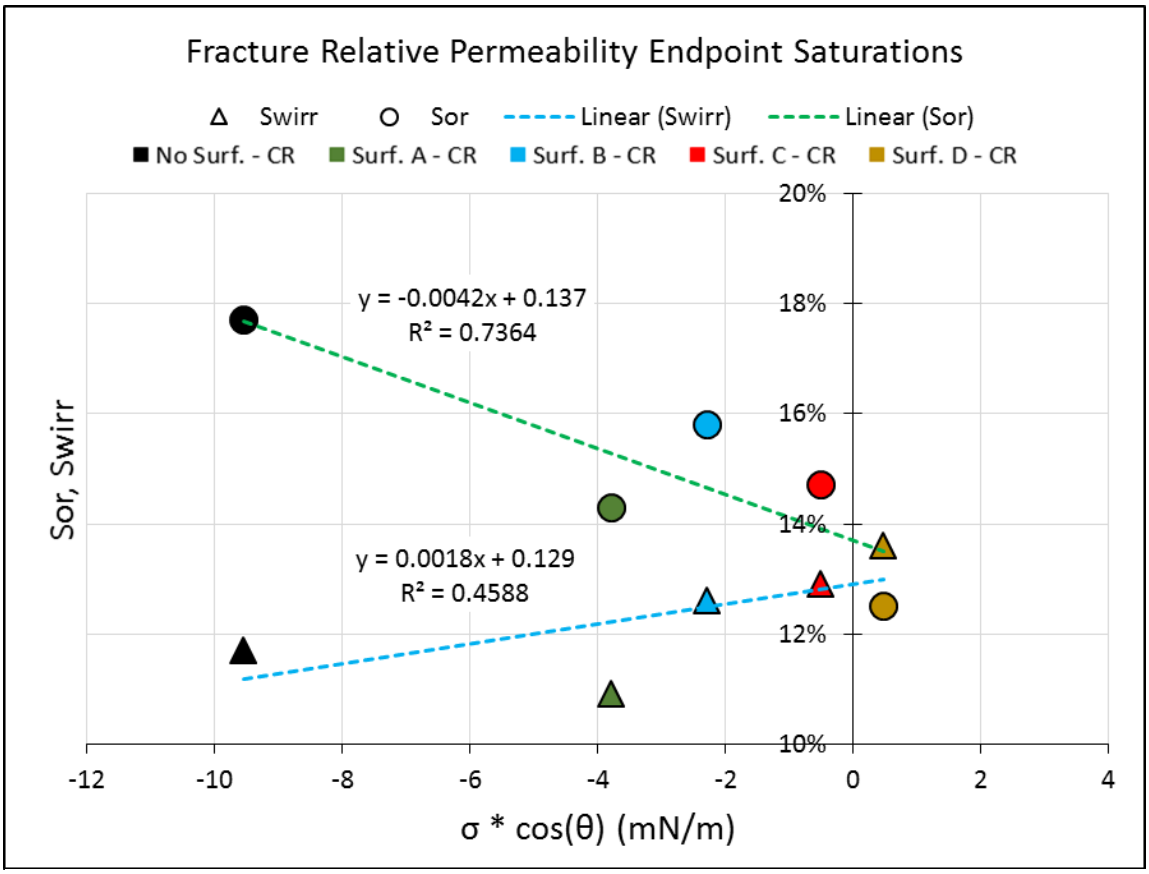

Fig. 3.24 – Carbonate Rich Fracture Relative Permeability Endpoint Saturations Plotted as a Function of the Product of Interfacial Tension (σ) and the Cosine of Contact Angle (cos(θ)).

As presented for the quartz rich experiments, the fracture endpoint relative permeabilities for the carbonate rich experiments are also plotted as a function of each fluid system properties as shown in **Fig. 3.25**. Similarly to the quartz rich results, the carbonate rich experiments also showed that the relative permeability to oil at irreducible water has a direct relationship to the product of the fluid system properties, while the relative permeability to water shows an inverse relationship to the same. The relationship between the endpoint relative permeabilities and the fluid system properties for the carbonate rich experiments is not as strong as in the quartz rich experiments, possibly due to the more oil-wet nature of the carbonate samples.

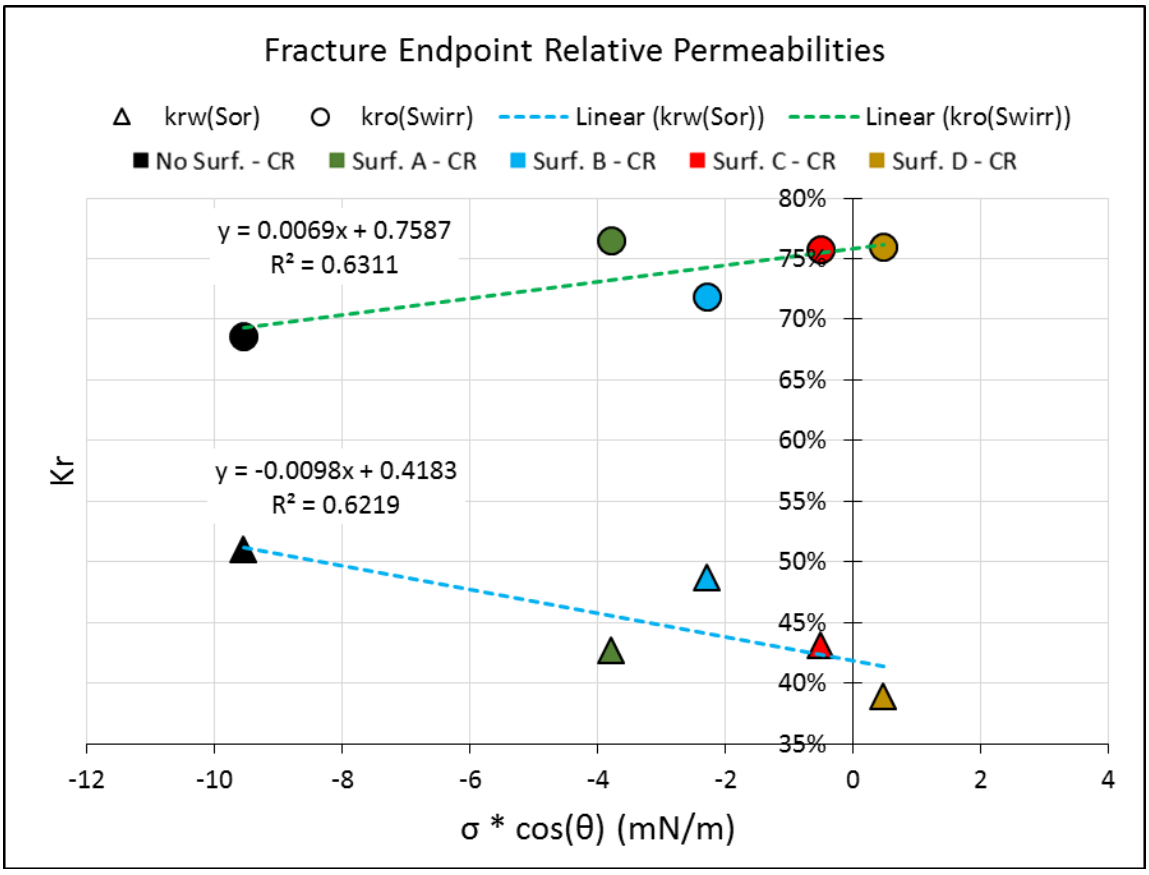

Fig. 3.25 – Carbonate Rich Fracture Endpoint Relative Permeabilities Plotted as a Function of the Product of Interfacial Tension (σ) and the Cosine of Contact Angle (cos(θ)).

Also as presented for the quartz rich experiments, the fracture relative permeability crossing points for the carbonate rich experiments are plotted as a function of the product of the fluid system properties in **Fig. 3.26**. It can be observed that there is a direct relationship between the product of the fluid system properties and an increase in the relative permeability crossing points. This direct relationship indicates that an increasing positive value of the product of interfacial tension and cosine of the contact angle will lead to a higher degree of wettability alteration, and subsequently improved relative permeability to oil as well as reduced residual oil saturation.

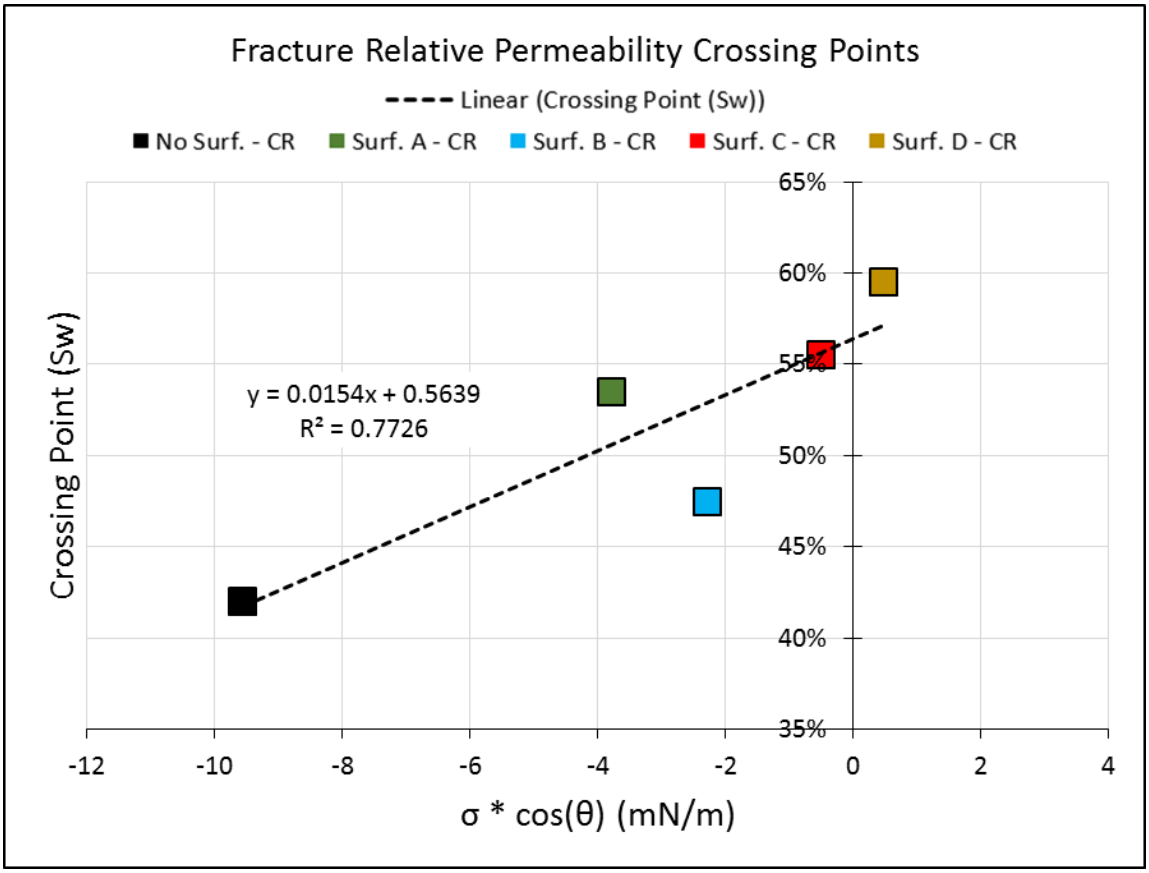

Fig. 3.26 – Carbonate Rich Fracture Relative Permeability Crossing Points (Sw) Plotted as a Function of the Product of Interfacial Tension (σ) and the Cosine of Contact Angle (cos(θ)).

4. NUMERICAL SIMULATION

4.1 Introduction

In order to better understand the oil-water relative permeability in fractures measured in this study, a numerical reservoir simulations was conducted using Eclipse Blackoil Reservoir Simulation (E100) (Schlumberger, version 2014.2).

The process of numerical reservoir modeling consists of discretizing the reservoir into distinct units in three dimensions, and calculating the progression of reservoir properties and fluids within each distinct unit through space at discrete time steps.

The main equation solved in the calculation of each time step and for each distinct reservoir unit division is the diffusivity equation. The diffusivity equation is obtained by applying mass balance over a control volume. The equation of motion (Darcy's Law) as well as the equation of state (PVT relations) are then combined with the mass balance equation to obtain the final form of the diffusivity equation. Additionally, a well model is applied at each element that contains a well serving as a source (producer) or a sink (injector).

Finally, there are several techniques to solve the resulting equations at each discrete reservoir unit division and each discrete time step. The three most prevalent techniques are Finite Difference Method (used in this numerical reservoir simulation), Boundary Element or Finite Element Method, and Streamline Simulation Method.

4.2 Simulation Domain

The Wofcamp formation from which the core test samples were obtained is a naturally fractured reservoir, containing two complementary natural fracture joint sets. It is important that all reservoir characteristics are properly represented within the model, to make the numerical reservoir simulation results relevant. For this purpose, it is important to describe the three main physical regions where flow is occurring and the scale differences between each region.

A conceptual representation of a horizontal wellbore with a set of five propped hydraulic fractures along with three distinct flow regions is illustrated in **Fig. 4.1**. The three main regions depicted are: (1) flow from matrix to unpropped fractures, (2) flow within unpropped fractures to a propped hydraulic fracture, and (3) flow within propped hydraulic fractures leading to the wellbore.

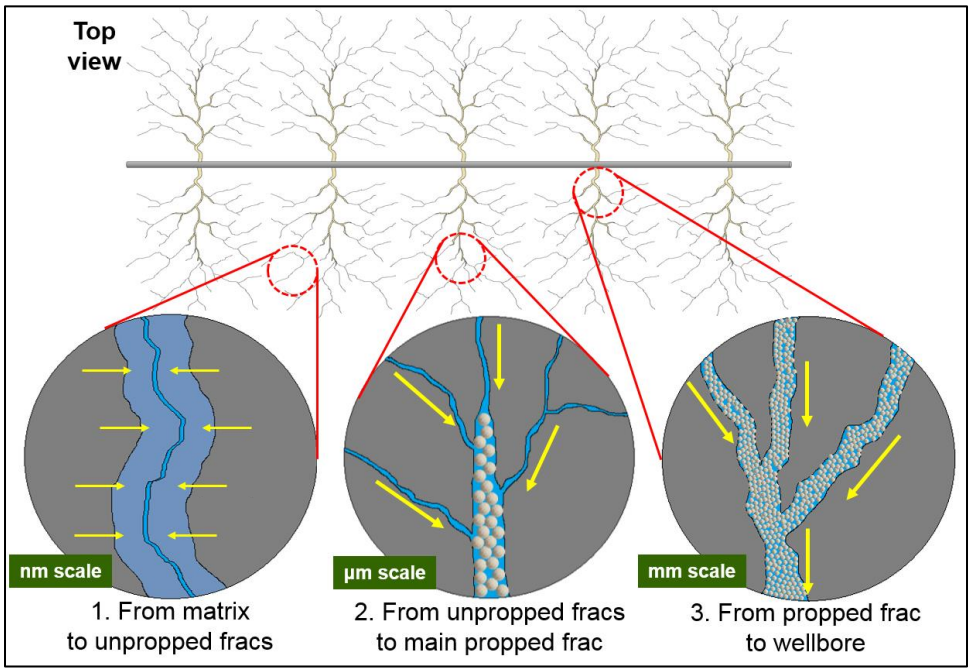

Fig. 4.1 – Conceptual Representation of Different Flow Regions Within a Stimulated Reservoir

The three conceptual flow regions described in **Fig. 4.1** were then modeled using representative dimensions for cells assigned to each region.

In order to simplify the numerical simulation, the orientation of the natural fractures was converted to a discrete fracture network which is orthogonal with respect to the horizontal wellbore, having a spacing of 6-ft between the primary set of natural fractures, and a spacing of 15-ft between the secondary set of natural fractures. The propped hydraulic fractures were modeled to be perpendicular to the wellbore and symmetrical. Both unpropped and propped fractures were explicitly modeled in order to capture the effects of fracture relative permeability in the model. The unpropped fractures were prescribed a fracture aperture of 0.00394 inch, a porosity of 16.75%, and a permeability of 200 millidarcy as measured from the experiments in Section 3. The propped fractures were prescribed a fracture aperture of 0.125 inch, a porosity of 35.50%, and a permeability of 50,000 millidarcy (propped fracture values were assumed).

The matrix permeability was prescribed for two distinct zones, namely the unmodified matrix permeability zone having a permeability of 40 nanodarcy, and the enhanced matrix permeability zone having a permeability of 400 nanodarcy (matrix permeability values were provided by Pioneer Natural Resources).

Due to the explicit modeling of the fractures, the smallest symmetrical section was chosen as the simulation domain shown in **Fig. 4.2**. This symmetry simulation section has a length of 15 feet, a width of 3 feet and a height of 10 feet, resulting in a total volume of 450 cubic feet.

As shown in **Fig. 4.2**, the symmetry simulation element contains a propped fracture, as well as both natural fracture joint sets represented in the form of the orthogonal discrete fracture network. Matrix which is in contact with either a propped fracture or a natural fracture was assigned to the enhanced matrix permeability zone having a depth of 6 inches from the contacting respective fracture (this depth was assumed to be the same for both propped and unpropped fractures). The summary of the physical properties used for each modeled region is shown in **Table 4.1**.

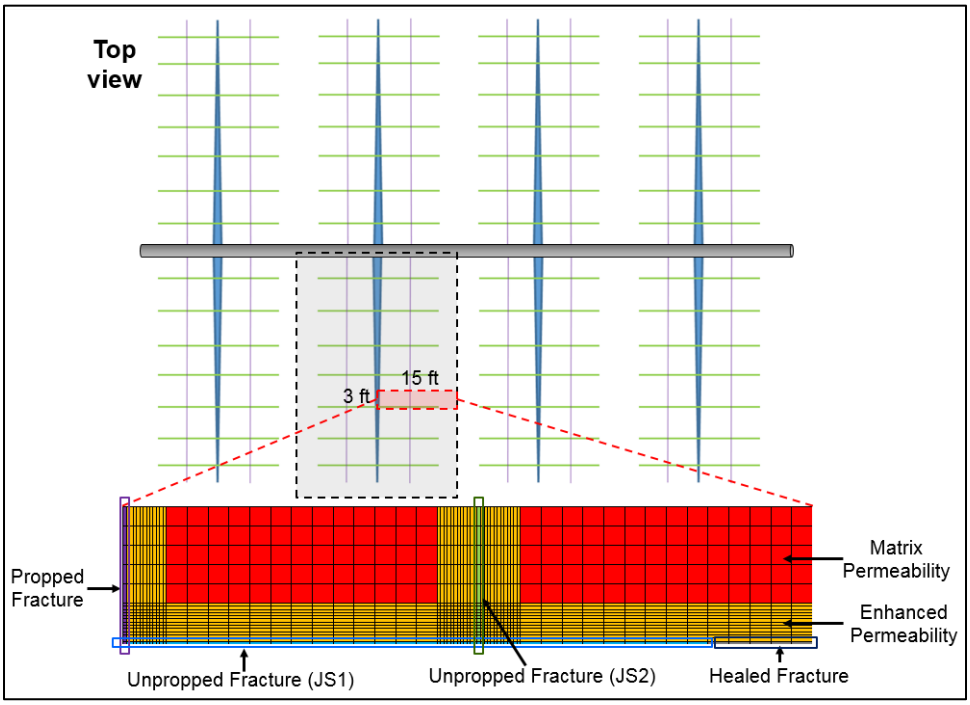

Fig. 4.2 – Conceptual Representation of the Domain for the Numerical Reservoir Simulation.

Table 4.1 – Summary of Physical Properties for each Simulation Region

Simulation Region	k	ϕ	Cell Width	C_f
Propped Fractures	50000 md	33.50 %	0.12500 in	520.8333 mD-ft
Unpropped Fractures	200 md	16.75 %	0.00394 in	0.0656 mD-ft
Enhanced Matrix	400 nd	9.20 %	0.50000 in	- -
Matrix	40 nd	9.20 %	6.00000 in	- -

4.3 Simulation Methodology

As mentioned before, the simulation domain has four regions: (1) propped hydraulic fracture region, (2) unpropped natural fracture joint set region, (3) enhanced permeability matrix region, and (4) matrix permeability region.

Each region is then assigned two sets of relative permeability values as a function of water saturation. The first set of relative permeabilities correspond to an oil-water system with no wettability alteration (no surfactant case), and the second set corresponds to the altered wettability state (corresponding to each of the four surfactant cases). These relative permeability values are comprised of tabulated data containing water relative permeability, and oil relative permeability, as a function of water saturation. The relative permeability tables used for the numerical reservoir simulation were generated with the results from the experimental measurements described in Section 3, and are included in the Appendix.

The numerical simulator then interpolates between each respective set of saturation tables based on surfactant concentration in each respective region. The surfactant concentration in the water phase is prescribed at the initialization of the model at the same concentration as used in the field and the experiments conducted in this study (1 gallon per thousand gallons of fluid), and subsequently calculated based on a surfactant adsorption function at each subsequent time step of the numerical simulation.

The following section describes the results of the numerical simulations.

4.4 Simulation Results

The results for the numerical reservoir simulation described in Section 4.2 and Section 4.3, are presented in this section. The simulation results are presented in the same manner as the experimental results from Section 3, which are presented in two categories: quartz rich results and carbonate rich results.

4.4.1 Quartz Rich Simulation Results

The quartz rich experimental results from Section 3.3 were used to generate five sets of relative permeability tables as a function of water saturation, as described in Section 4.3 and shown in Appendix. Each set of tabulated relative permeably data corresponds to each case: no-surfactant, Surf. A, Surf. B, Surf. C, and Surf. D.

The performance metrics chosen to be analyzed from the numerical reservoir simulation results are the 500-day cumulative oil production as well as the peak initial oil production rate.

The simulated 500-day cumulative oil production profile for each simulation case are plotted as shown in **Fig. 4.3**, and summarized in **Fig. 4.4**.

The simulated 500-day oil production rate profile for each simulation case was also plotted as shown in **Fig. 4.5**, and the peak oil production rate taken as the maximum production rate for each case is summarized in **Fig. 4.6**.

The simulated 500-day cumulative oil production for each simulated case is plotted as show in **Fig. 4.3**. As can be seen from **Fig. 4.3**, all simulation cases have a similar production profile; however, all simulated cases that contain a surfactant additive have higher oil production when compared to the no-surfactant case. The relative difference between each surfactant case and the no-surfactant case is plotted in **Fig. 4.4**.

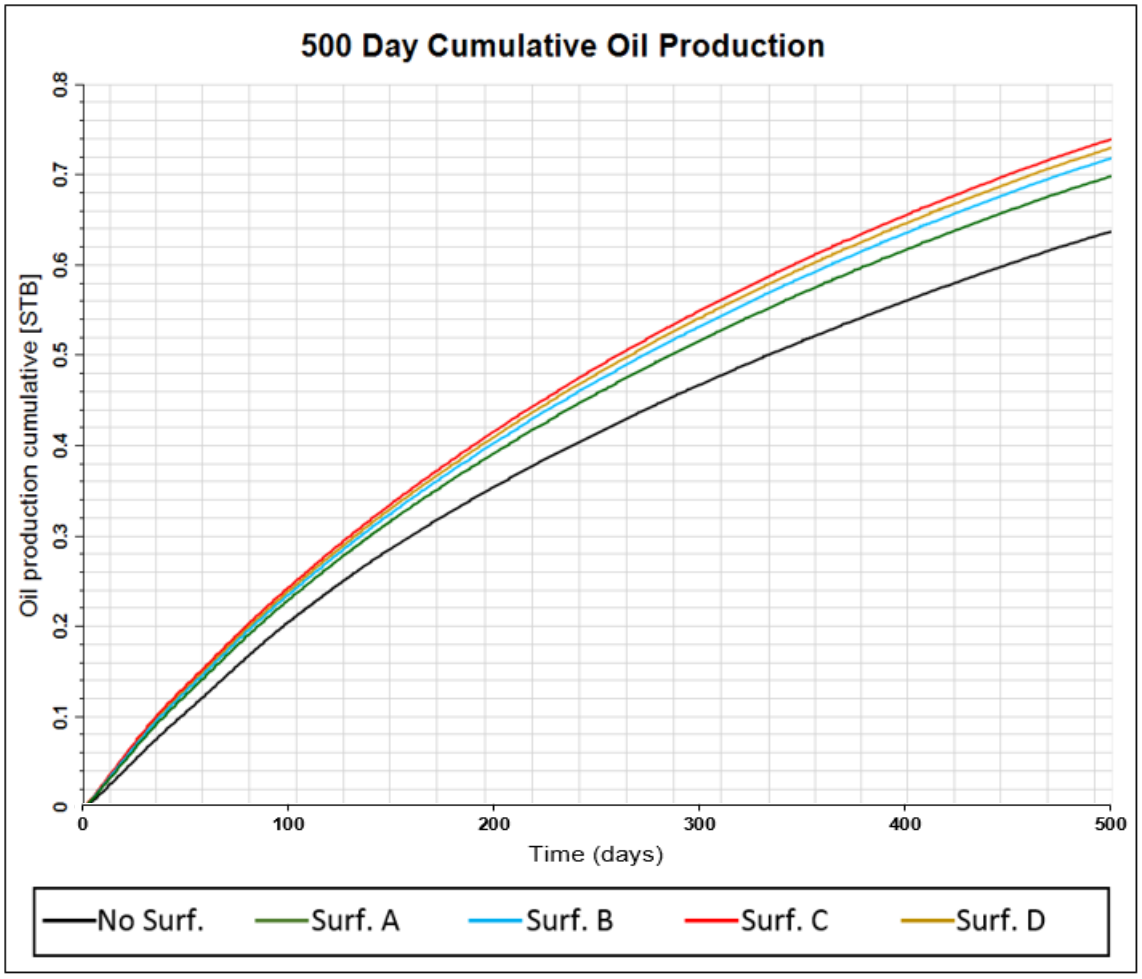

Fig. 4.3 – 500 Day Cumulative Oil Production from Quartz Rich Numerical Reservoir Simulations.

The simulated increase in 500-day cumulative oil production for each quartz rich surfactant case with respect to the no-surfactant case is shown in **Fig. 4.4**.

It can be observed that although all surfactant cases showed an improvement in the oil production, there is a clear difference amongst each individual surfactant additive. The highest oil production increase for the quartz rich simulations was obtained from the Surf. C surfactant additive, followed by Surf. D, Surf. B, and Surf. A in descending order.

The relationship between surfactant properties and the increase in oil production is further discussed in Section 4.4.3.

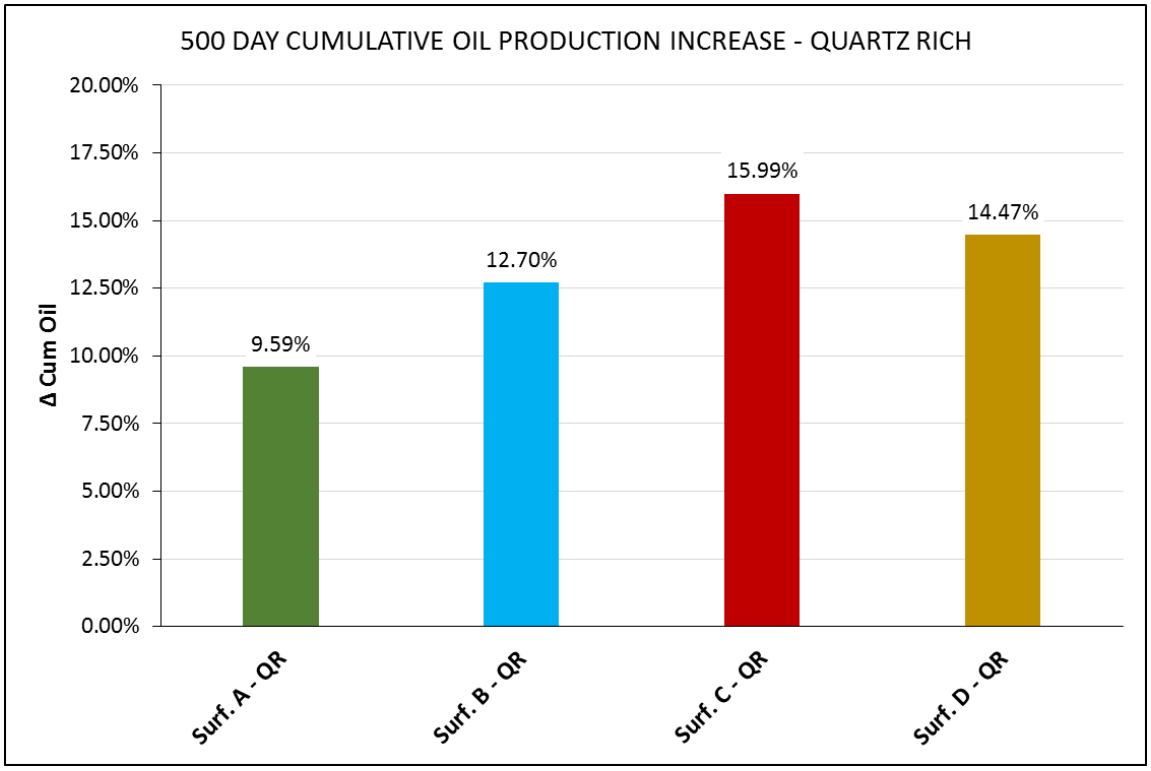

Fig. 4.4 – Increase in 500 Day Cumulative Oil Production from Quartz Rich Numerical Reservoir Simulations.

The simulated 500-day cumulative oil production rate for each simulated case is plotted as show in **Fig. 4.5**. As can be seen from **Fig. 4.5**, all simulation cases have a similar production rate profile; however, all simulated cases containing a surfactant additive had significantly greater oil production rates when compared to the no-surfactant case. It can also be observed that the greatest difference in production rates occurs during early production. To better see the relative difference between each simulated case, the peak oil production rate increase is shown in **Fig. 4.6**.

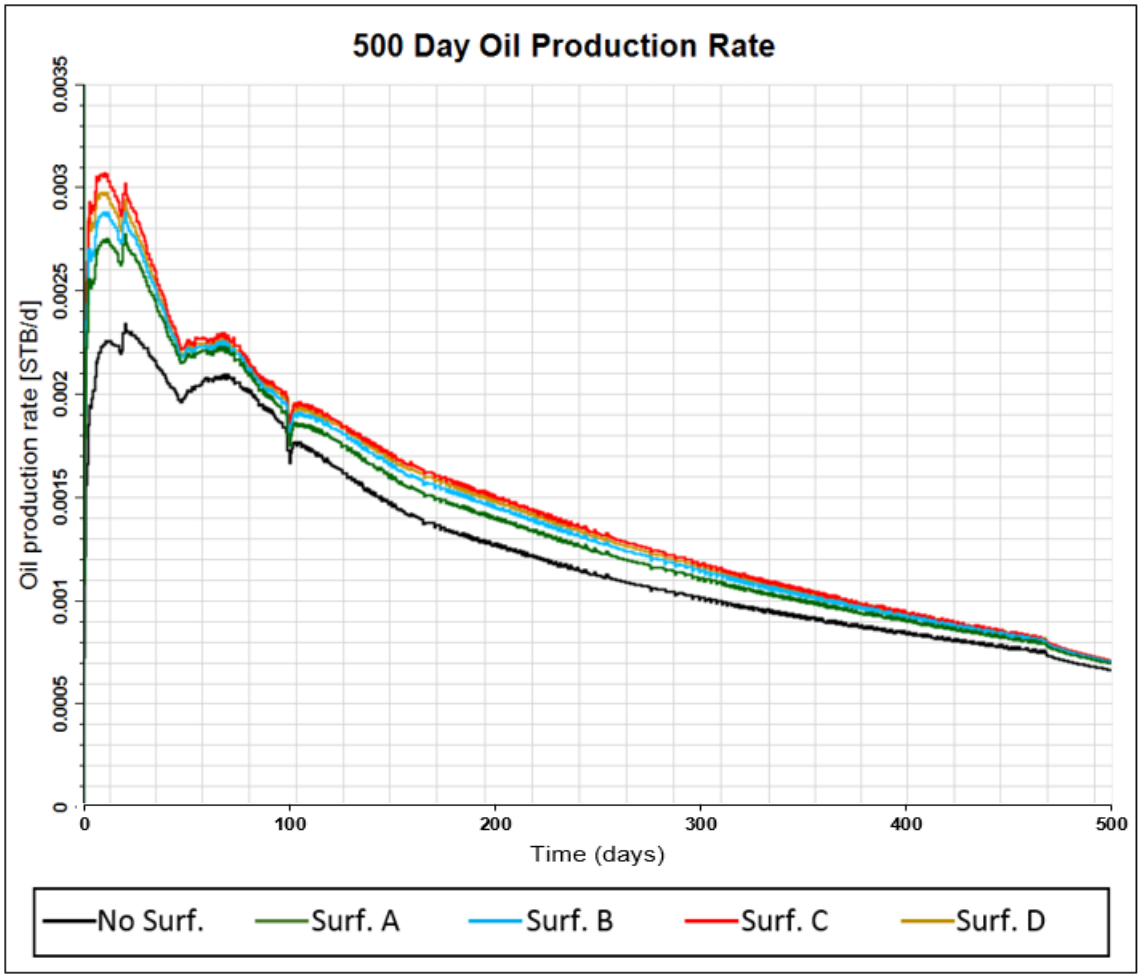

Fig. 4.5 – 500 Day Oil Production Rate from Quartz Rich Numerical Reservoir Simulations.

The increase in peak simulated oil production rate from **Fig. 4.5** for each surfactant additive case when compared to no-surfactant case is plotted in **Fig. 4.6**. The maximum oil production rate from all cases was selected as the peak reference, and the corresponding rate for the remaining cases was taken from the same date for comparison.

It can be observed that although all surfactant cases showed a significant improvement in peak oil production rate, there is a clear difference amongst each individual surfactant additive. Similarly to the cumulative oil production increase shown in **Fig. 4.4**, the highest peak oil production rate increase for the quartz rich simulations was obtained from the Surf. C surfactant additive, followed by Surf. D, Surf. B, and Surf. A in descending order.

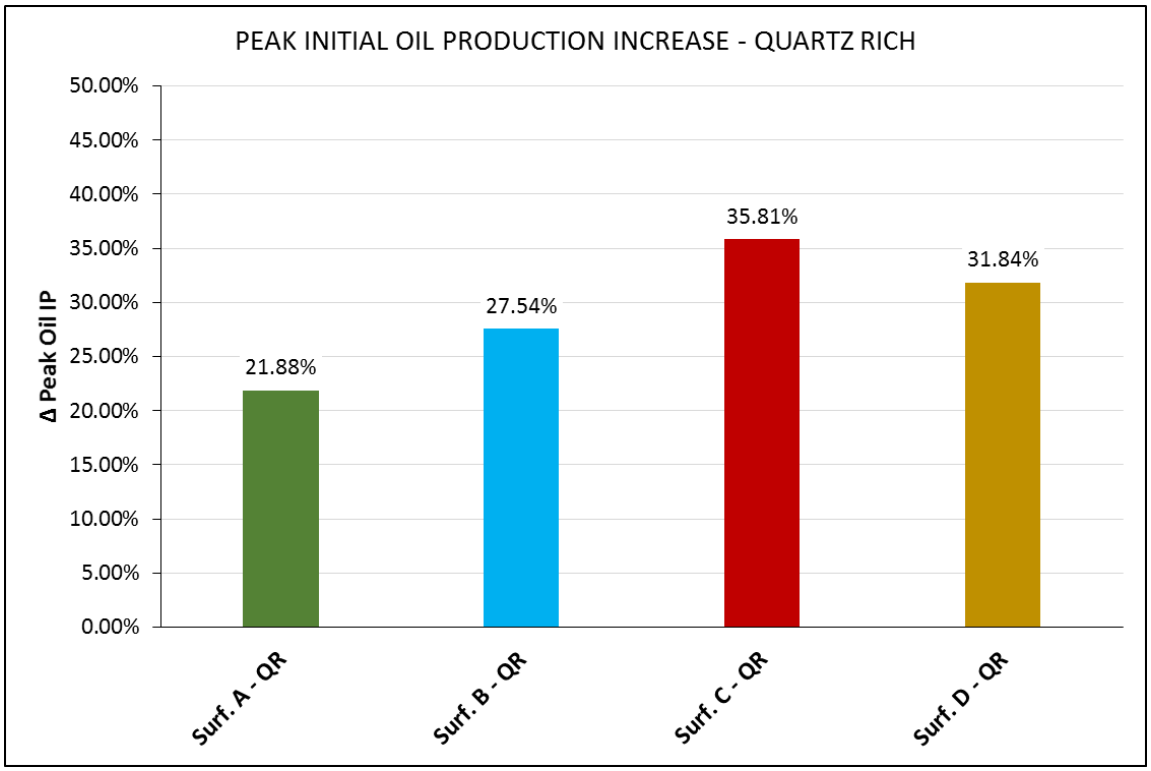

Fig. 4.6 – Increase in 500 Day Peak Initial Oil Production Rate from Quartz Rich Numerical Reservoir Simulations.

4.4.2 Carbonate Rich Simulation Results

Following the same presentation of the simulation results for the quartz rich simulations, the carbonate rich experimental results from Section 3.4 were also used to generate five sets of relative permeability tables as a function of water saturation, as described in Section 4.3. Each set of tabulated relative permeably data corresponds to each case tested: no-surfactant, Surf. A, Surf. B, Surf. C, and Surf. D.

The performance metrics chosen to be analyzed from the numerical reservoir simulation results are the 500-day cumulative oil production as well as the peak initial oil production rate, same as in the quartz rich simulations.

The simulated 500-day cumulative oil production profile for each simulation case are plotted as shown in **Fig. 4.7**, and summarized in **Fig. 4.8**.

The simulated 500-day oil production rate profile for each simulation case was also plotted as shown in **Fig. 4.9**, and the peak oil production rate taken as the maximum production rate for each case at the same date is summarized in **Fig. 4.10**.

Similarly to the quartz rich simulation results, the simulated 500-day cumulative oil production for each carbonate rich simulated case is plotted as show in **Fig. 4.7**. As can be seen from **Fig. 4.7**, all simulation cases have a similar production profile; however, all simulated cases containing a surfactant additive had higher oil production when compared to the no-surfactant case. The relative difference between each surfactant case and the no-surfactant case is plotted in **Fig. 4.8**.

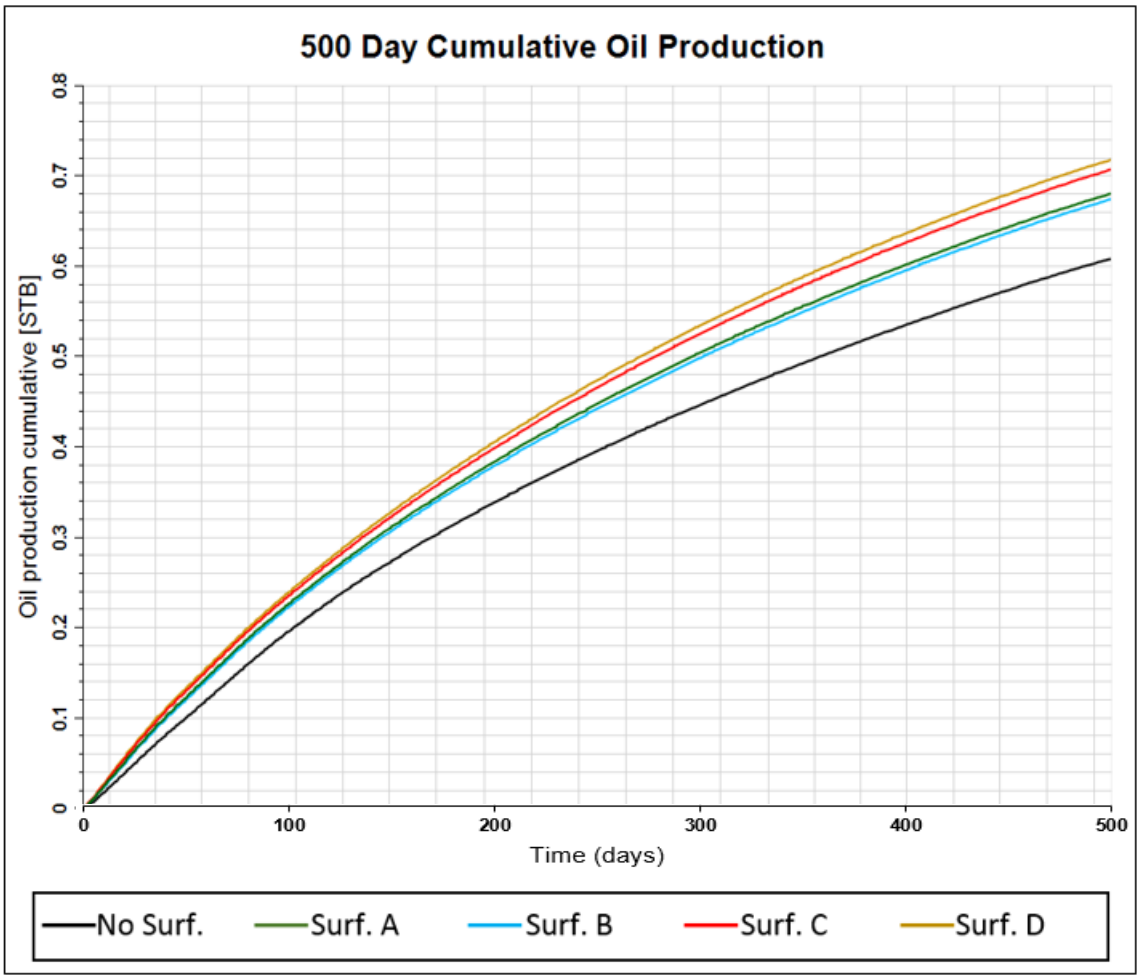

Fig. 4.7 – 500 Day Cumulative Oil Production from Carbonate Rich Numerical Reservoir Simulations.

The simulated increase in 500-day cumulative oil production for each carbonate rich surfactant case with respect to the no-surfactant case is shown in **Fig. 4.8**.

Similarly to the quartz rich simulation results, it can be observed that although all surfactant cases showed an improvement in oil production, there is a clear difference amongst each individual surfactant additive. The highest oil production increase for the carbonate rich simulations was obtained from the Surf. D surfactant additive, followed by Surf. C, Surf. A, and Surf. B in descending order.

The relationship between surfactant properties and the increase in oil production is further discussed in Section 4.4.4.

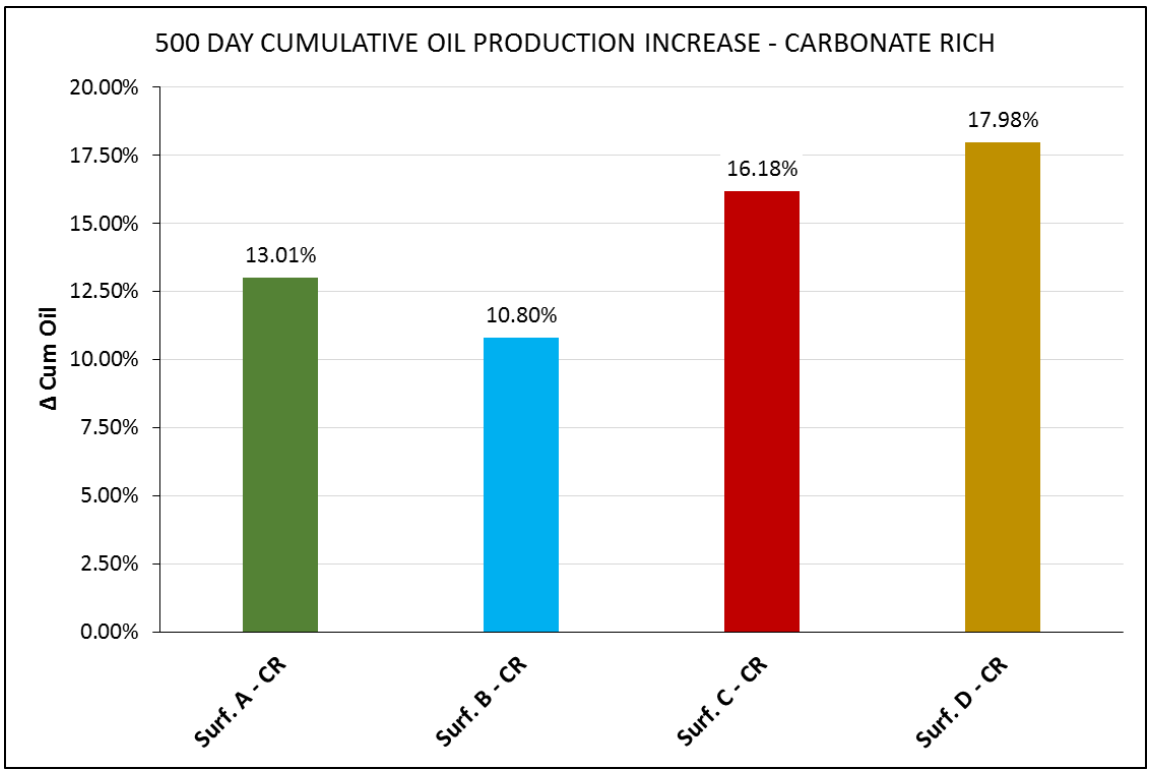

Fig. 4.8 – Increase in 500 Day Cumulative Oil Production from Carbonate Rich Numerical Reservoir Simulations.

The simulated 500-day cumulative oil production rate for each carbonate rich simulated case is plotted as show in **Fig. 4.9**. As can be seen from **Fig. 4.9**, all simulation cases have a similar production rate profile; however, all simulated cases containing a surfactant additive had higher oil production rates when compared to the no-surfactant case. It can also be observed that the greatest difference in production rates occurs during early production. To better see the relative difference between each simulated case, the peak oil production rate increase is shown in **Fig. 4.10**.

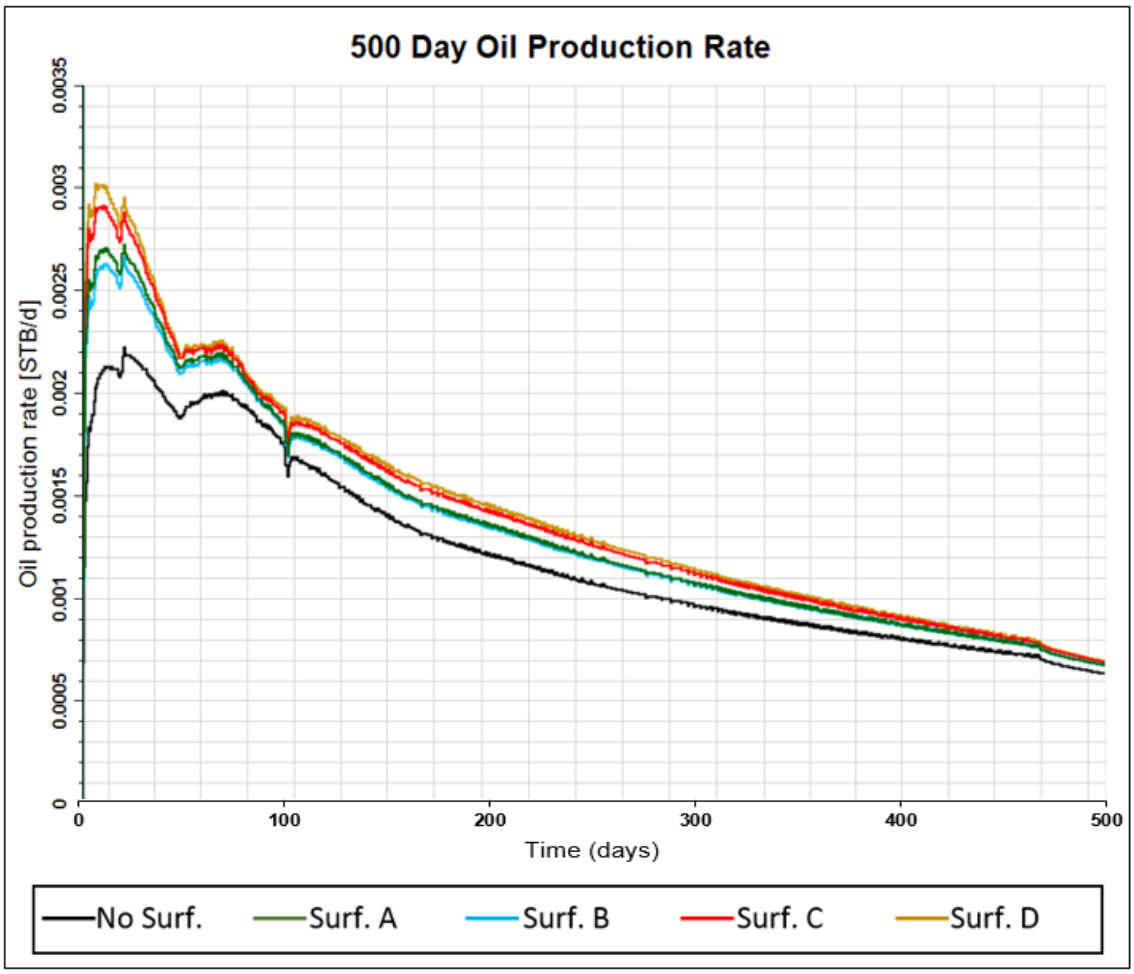

Fig. 4.9 – 500 Day Oil Production Rate from Carbonate Rich Numerical Reservoir Simulations.

The increase in peak simulated oil production rate from **Fig. 4.9** for each surfactant additive case when compared to no-surfactant case is plotted in **Fig. 4.10**. The maximum oil production rate from all cases was selected as the peak reference, and the corresponding rate for the remaining cases was taken from the same date for comparison.

It can be observed that although all surfactant cases showed a significant improvement in peak oil production rate, there is a clear difference amongst each individual surfactant additive. Similarly to the cumulative oil production increase shown in **Fig. 4.10**, the highest peak oil production rate increase for the carbonate rich simulations was obtained from the Surf. D surfactant additive, followed by Surf. C, Surf. A, and Surf. B in descending order.

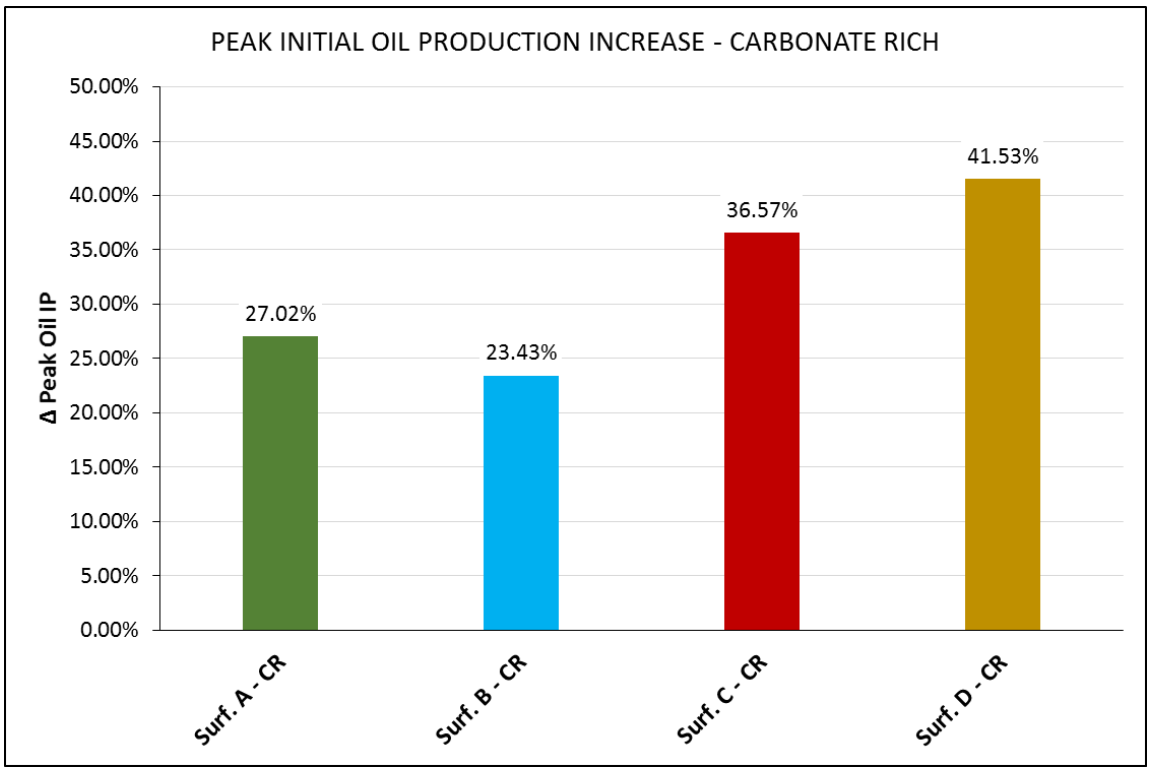

Fig. 4.10 – Increase in 500 Day Peak Initial Oil Production Rate from Carbonate Rich Numerical Reservoir Simulations.

4.4.3 Quartz Rich Simulation Results Summary and Discussion

The numerical simulation results for the quartz rich samples presented in Section 4.4.1 are summarized in this section. The simulated 500-day cumulative oil production and the peak oil production rate were plotted as a function of the contact angle, as shown in **Fig. 4.11**. It can be observed that there is an inverse relationship between both the cumulative oil production and peak oil production rate, and the contact angle of each fluid system. Therefore, it can be concluded that a lower contact angle (indicating a more water-wet system) is desirable for increased oil production.

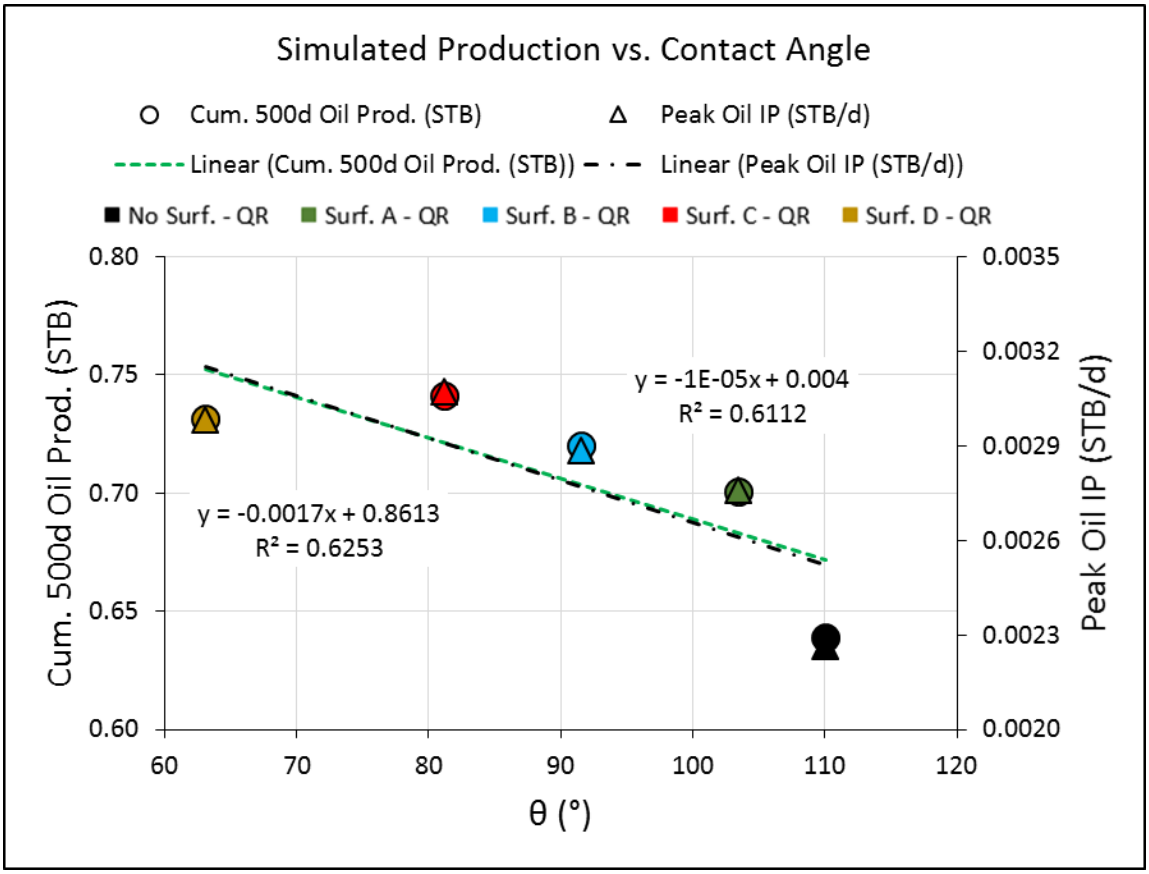

Fig. 4.11 – Quartz Rich Simulated 500 Day Cumulative Oil Production and Peak Initial Oil Production Rate Plotted as a Function of Surfactant Contact Angle (θ).

The simulated 500-day cumulative oil production and the peak oil production rate were also plotted as a function of the interfacial tension, as shown in **Fig. 4.12**. Similarly to the relationship found with respect to contact angle, both the simulated 500-day cumulative oil production and the peak oil production rate show an inverse relationship to the interfacial tension of each fluid system. Therefore, it can be concluded that a lower interfacial tension is also desirable for increased oil production.

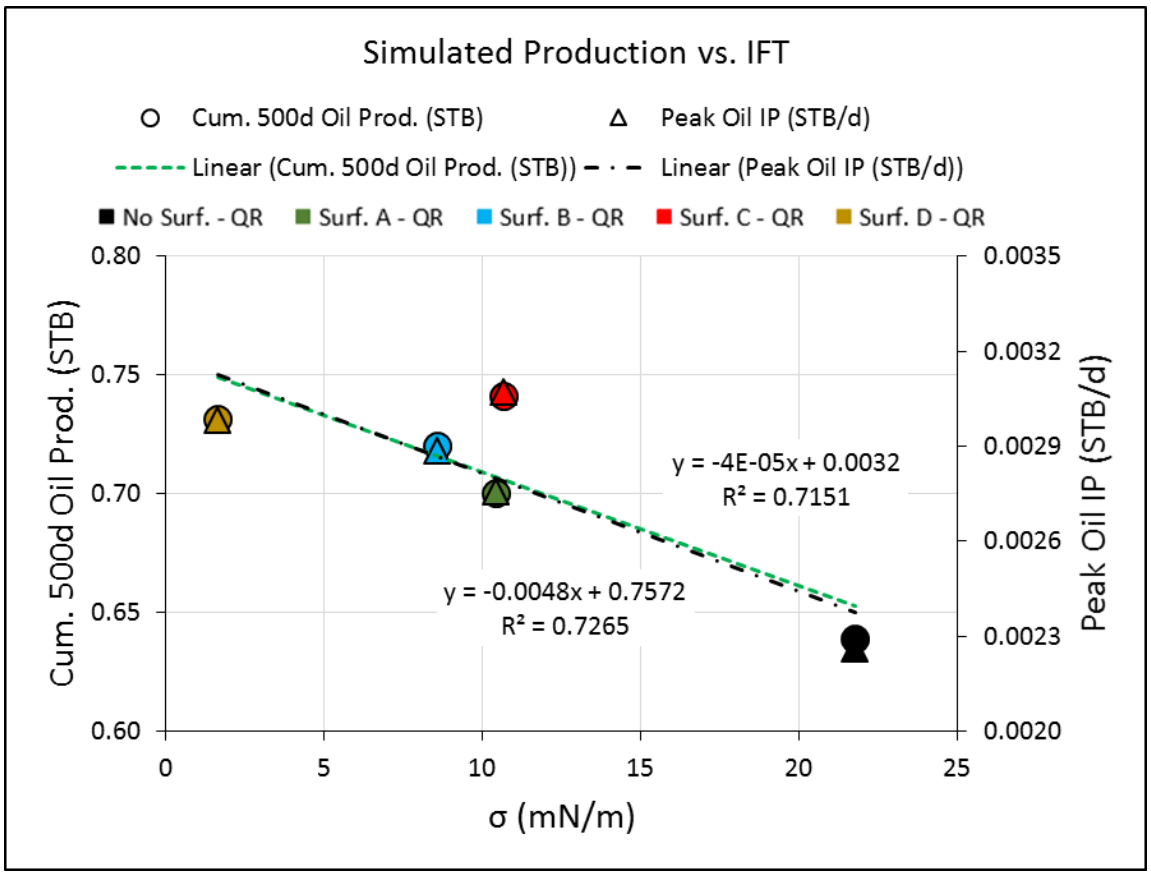

Fig. 4.12 – Quartz Rich Simulated 500 Day Cumulative Oil Production and Peak Initial Oil Production Rate Plotted as a Function of Oil-Water-Surfactant Interfacial Tension (σ).

Finally, the simulated 500-day cumulative oil production and the peak oil production rate were also plotted as a function of the product of interfacial tension and the cosine of contact angle, as shown in **Fig. 4.13**. In this case, it can be observed that there is a direct relationship between both the simulated 500-day cumulative oil production and the peak oil production rate with respect to the combined effect of interfacial tension and contact angle. Observing this combined effect of fluid system properties on the oil production behavior, it is clear the most desirable fluid system to be used as a fracturing fluid should include a surfactant which increases the product of interfacial tension and the cosine of the contact angle.

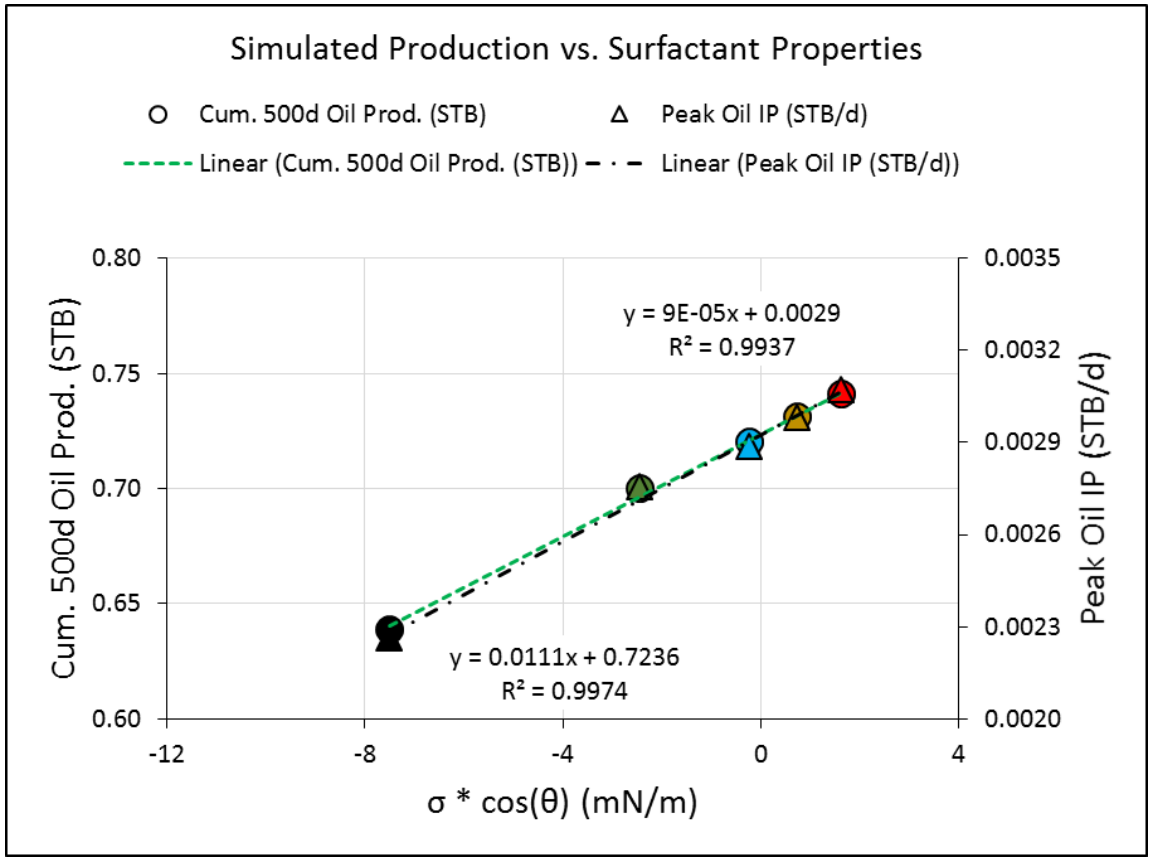

Fig. 4.13 – Quartz Rich Simulated 500 Day Cumulative Oil Production and Peak Initial Oil Production Rate Plotted as a Function of the Product of the Oil-Water-Surfactant Interfacial Tension (σ) and Surfactant Contact Angle (θ).

4.4.4 Carbonate Rich Simulation Results Summary and Discussion

The numerical simulation results for the quartz rich samples presented in Section 4.4.2 are summarized in this section. Similarly to the quartz rich simulation results, the simulated 500-day cumulative oil production and the peak oil production rate for the carbonate rich simulation results were plotted as a function of the contact angle, as shown in **Fig. 4.14**. The same inverse relationship between both the cumulative oil production and peak oil production rate, and the contact angle of each fluid system observed in the quartz rich simulation results was also observed in the carbonate rich simulation results, where decreasing contact angle leads to increased oil production.

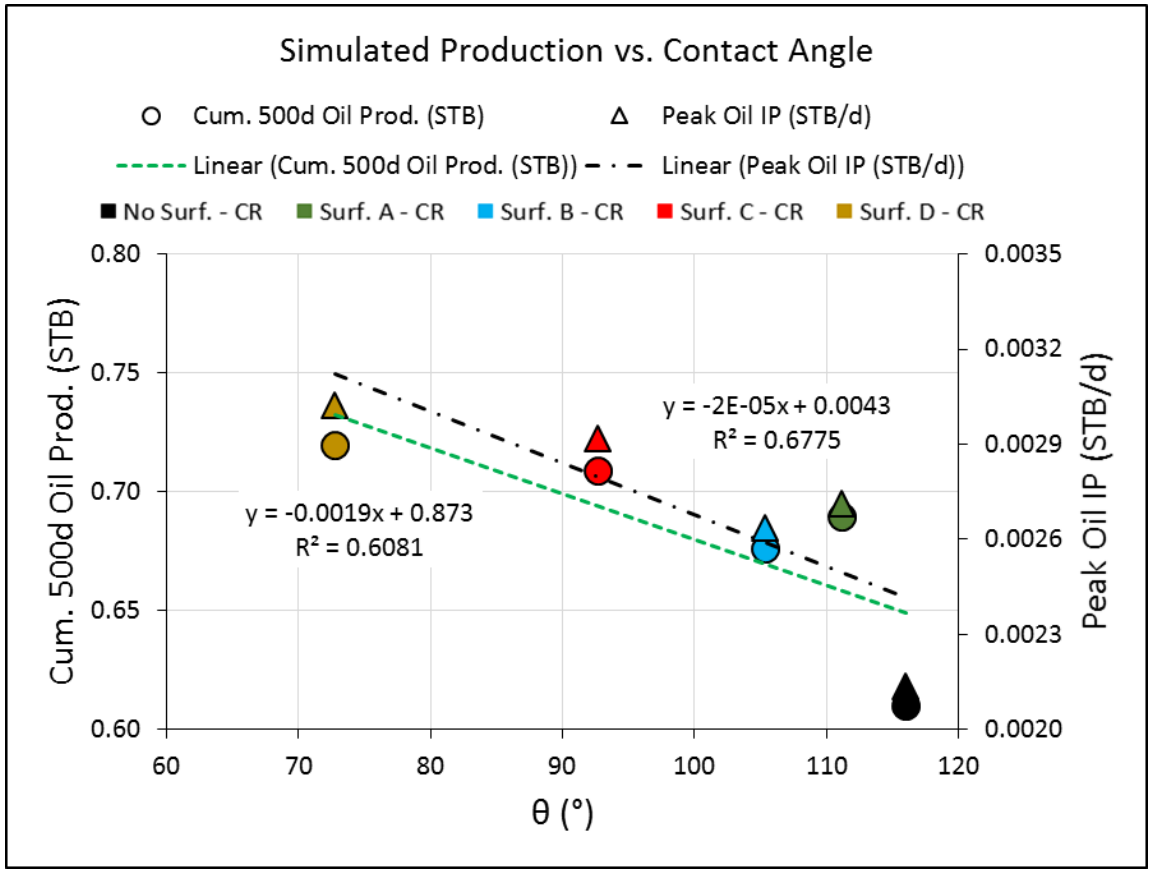

Fig. 4.14 – Carbonate Rich Simulated 500 Day Cumulative Oil Production and Peak Initial Oil Production Rate Plotted as a Function of Surfactant Contact Angle (θ).

The simulated 500-day cumulative oil production and the peak oil production rate for the carbonate rich simulations were also plotted as a function of the interfacial tension, as shown in **Fig. 4.15**. Again, the same inverse relationship found for the quartz rich simulation results between the simulated 500-day cumulative oil production and the peak oil production rate with respect to the interfacial tension, was also observed for the carbonate rich samples. Therefore, the same conclusion can be reached: a lower interfacial tension is desirable for increased oil production.

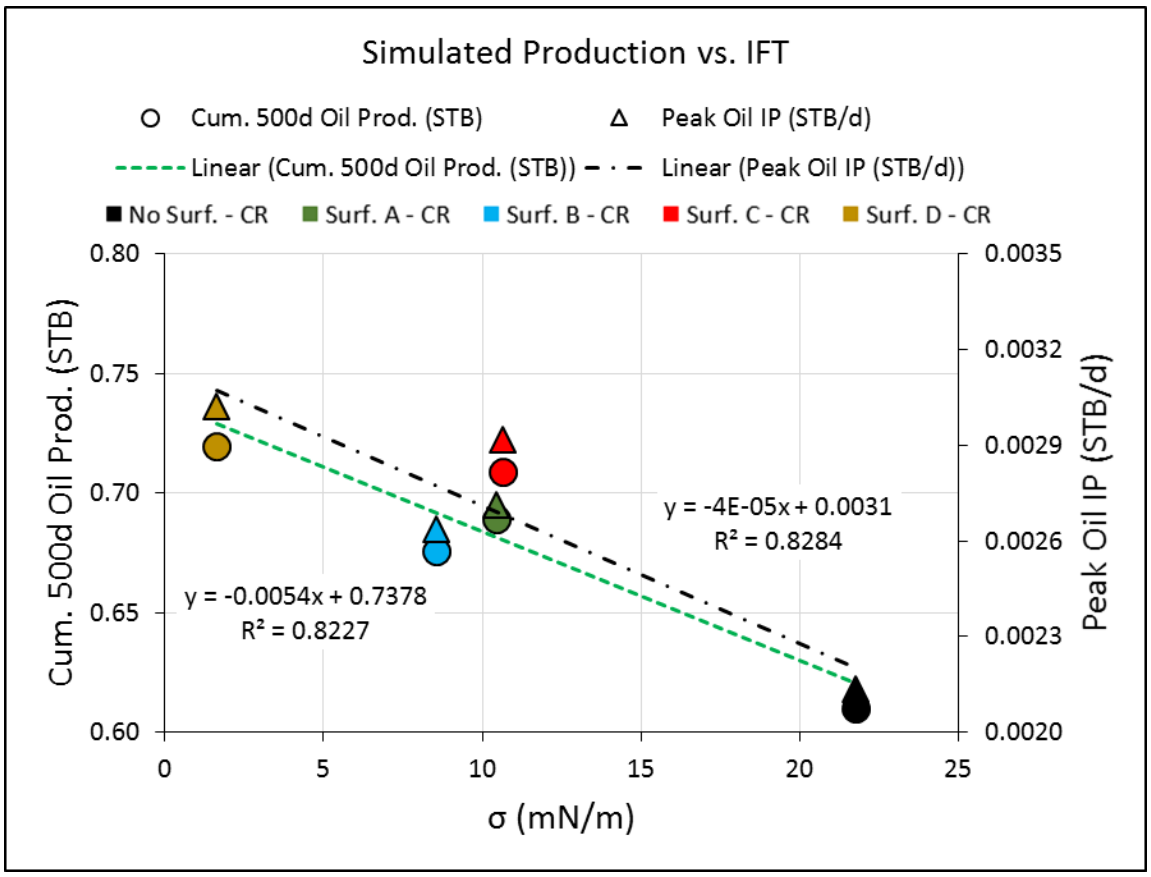

Fig. 4.15 – Carbonate Rich Simulated 500 Day Cumulative Oil Production and Peak Initial Oil Production Rate Plotted as a Function of Oil-Water-Surfactant Interfacial Tension (σ).

Finally, the simulated 500-day cumulative oil production and the peak oil production rate for the carbonate rich simulation results were also plotted as a function of the product of interfacial tension and the cosine of contact angle, as shown in **Fig. 4.16**. Again, the same direct relationship found for the quartz rich simulation results between the simulated 500-day cumulative oil production and the peak oil production rate with respect to the product of interfacial tension and cosine of contact angle, was also observed for the carbonate rich samples. Therefore, the same conclusion can be reached: the most desirable fluid system to be used as a fracturing fluid should include a surfactant which increases the product of interfacial tension and the cosine of the contact angle.

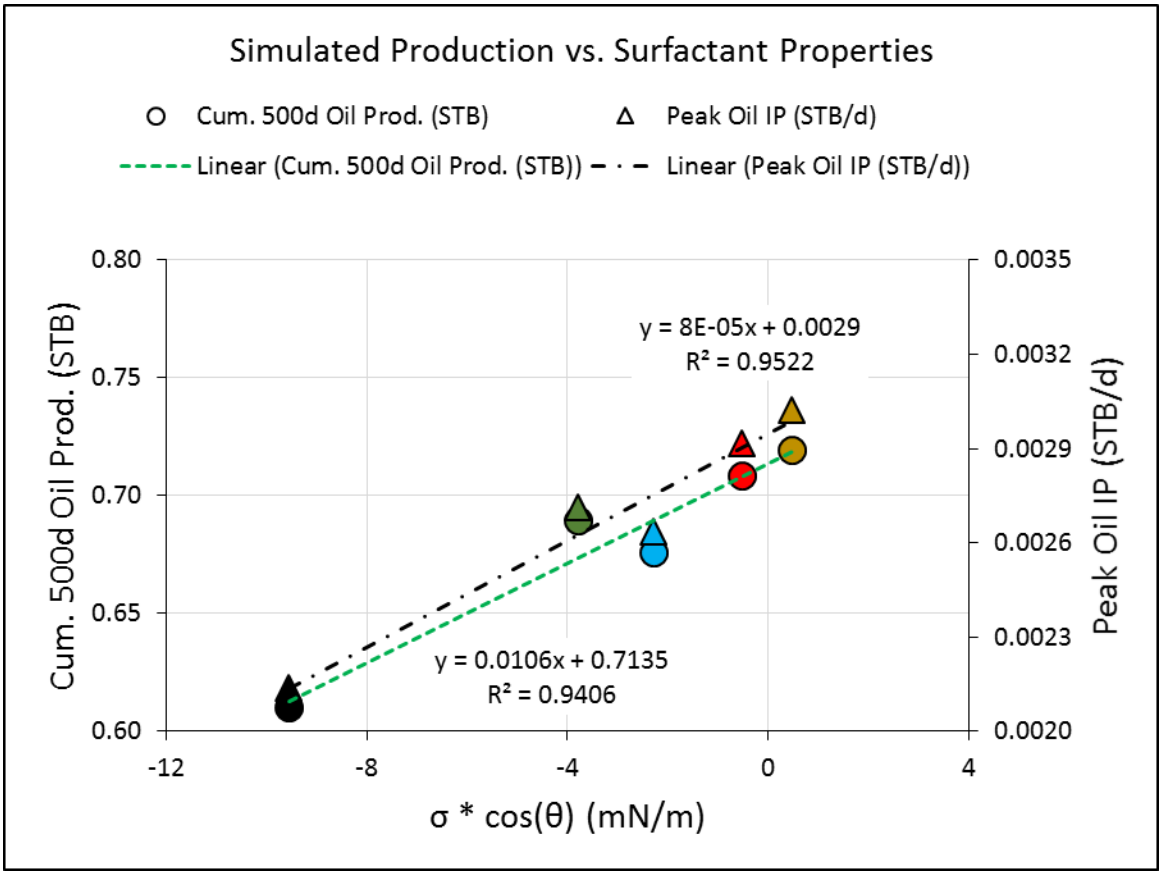

Fig. 4.16 – Carbonate Rich Simulated 500 Day Cumulative Oil Production and Peak Initial Oil Production Rate Plotted as a Function of the Product of the Oil-Water-Surfactant Interfacial Tension (σ) and Surfactant Contact Angle (θ).

4.5 Numerical Simulation Results Upscaling

As was described in Section 4.2, the simulation domain comprised the smallest symmetrical section within the conceptual stimulated reservoir volume of a horizontal well. The simulation results of this symmetrical section (both 500-day cumulative oil production and peak oil production rate) can be scaled to a full well by simply multiplying the results by the number of symmetry sections contained in the aforementioned full well.

An example of the calculation procedure for upscaling the simulated production from the symmetrical section (simulation domain) is presented in **Table 4.2**. In order to determine the number of symmetry sections contained in a specific well, the following dimensions must first be defined: lateral length (L), hydraulic fracture height (h_f), hydraulic fracture half-length (x_f), and perforation cluster spacing. The total number of hydraulic fractures is determined by dividing the lateral length by the cluster spacing. The hydraulic fracture surface area is determined by multiplying the height by two half-lengths. Finally, the well scale production is determined by multiplying the number of symmetry sections contained in each hydraulic fracture area by two (either side of the fracture), and then by their respective simulation result.

Table 4.2 – Example of Upscaling for Surf. D Carbonate Rich Simulation Results

WELL SCALE	Lateral Length (L)	7,000	ft
	Hydraulic Fracture Height (h_f)	100	ft
	Hydraulic Fracture Half-Length (x_f)	200	ft
	Cluster Spacing	50	ft
	Total Hydraulic Fractures	137	
	HF Surface Area	40,000	ft^2
	Number of Symmetry Sections	366,013	
	Simulated Peak Oil IP / Symmetry Section	0.003020	STB/d
	Simulated 500 Day Cum. Oil. Prod. / Symmetry Section	0.719470	STB
	Well Scale Peak Oil Production	**1,105**	**STB/d**
	Well Scale 500 Day Cumulative Oil Production	**263,335**	**STB**

5. UNDERSTANDING ENHANCED OIL RECOVERY MECHANISMS WITH SURFACTANTS

5.1 Introduction

All experimental and simulation results presented in prior sections of this study were presented in two groups: quartz rich and carbonate rich. Both groups of experimental data as well as simulation results tested five different cases respectively, for a total of ten different combinations of mineralogy and fluid systems.

The experimental results discussed in Sections 3.3 and 3.4, as well as the relationships between the measured relative permeabilities and the fluid system properties discussed in Sections 3.5 and 3.6 are summarized in Section 5.2. The results from all ten relative permeability experiments and their relationship to fluid system properties are summarized together in order to view the global trends for all cases.

The simulation results discussed in Sections 4.4.1 and 4.4.2, as well as the relationships between the simulated 500-day cumulative oil production and peak oil production rate with respect to the fluid system properties discussed in Sections 4.4.3 and 4.4.4 are summarized in Section 5.3. The results from all ten simulation and their relationship to fluid system properties are also summarized together in order to view the global trends for all cases.

5.2 Surfactant Effects on the Oil-Water Relative Permeability in Fractures

The results from the oil-water relative permeability measurements in fractures, which are described in Section 3.3 and Section 3.4, as well as a summary of the surfactant property measurements described in Section 2.3.3 are summarized in **Table 5.1**.

The contact angle as well as the oil-water interfacial tension for all cases of brine solution and test specimen mineralogy were measured in Section 2.3.3. The three columns under the subheading of Fluid Test Results in **Table 5.1** list the summary of the Contact Angle (θ), Oil-Water Interfacial Tension (σ), and the product of the Interfacial Tension and the Cosine of Contact Angle ($\sigma * \cos\theta$).A summary of the oil-water relative permeability tests in fractures as described in Section 3.3 and Section 3.4, are shown under the subheading Fracture Relative Permeability Test Results in **Table 5.1**. Summarized herein are the saturation endpoints (S_{wirr}, S_{or}), relative permeability endpoints ($k_{ro(Swirr)}$, $k_{rw(Sor)}$), and crossing points.

Table 5.1 – Summary of Surfactant Measurements, Resulting Fracture Relative Permeability Endpoint Saturations and Endpoint Relative Permeabilities.

		Fluids Tests Results			Fracture Relative Permeability Tests Resutls				
Surfactant	Core Sample	θ (°)	σ (mN/m)	σ * cos(θ) (mN/m)	S_{wirr}	S_{or}	$k_{ro(Swirr)}$	$k_{rw(Sor)}$	Crossing Point (Sw)
Frac Water - QR	Sample 5	110.10	21.78	-7.48	13.1%	17.5%	68.3%	48.6%	48.0%
Frac Water - CR	Sample 7A	116.00	21.78	-9.55	11.7%	17.7%	68.6%	51.0%	42.0%
Surf. A - QR	Sample 10	103.50	10.45	-2.44	12.5%	14.7%	73.9%	41.2%	56.0%
Surf. A - CR	Sample 7B	111.15	10.45	-3.77	10.9%	14.3%	76.5%	42.7%	53.5%
Surf. B - QR	Sample 3	91.55	8.58	-0.23	12.2%	14.8%	76.3%	44.5%	53.0%
Surf. B - CR	Sample 2	105.35	8.58	-2.27	12.6%	15.8%	71.8%	48.7%	47.5%
Surf. C - QR	Sample 4	81.25	10.68	1.62	12.5%	14.7%	76.9%	39.8%	59.0%
Surf. C - CR	Sample 1	92.70	10.68	-0.50	12.9%	14.7%	75.7%	43.1%	55.5%
Surf. D - QR	Sample 8	63.10	1.65	0.75	15.8%	12.8%	75.7%	37.4%	60.5%
Surf. D - CR	Sample 6	72.75	1.65	0.49	13.6%	12.5%	76.0%	38.9%	59.5%

Fracture relative permeability endpoint saturations (S_{wirr}, S_{or}) were plotted as a function of the product of the interfacial tension and the cosine of the contact angle ($\sigma * \cos\theta$), as shown in **Fig. 5.1**.

It can be observed that there is an inverse relationship between the fracture residual oil saturation (S_{or}) and the product of interfacial tension and cosine of contact angle ($\sigma * \cos\theta$). Furthermore, it can be observed there is a direct relationship, however weaker, between the fracture irreducible water saturation (S_{wirr}) and the product of interfacial tension and cosine of contact angle ($\sigma * \cos\theta$).

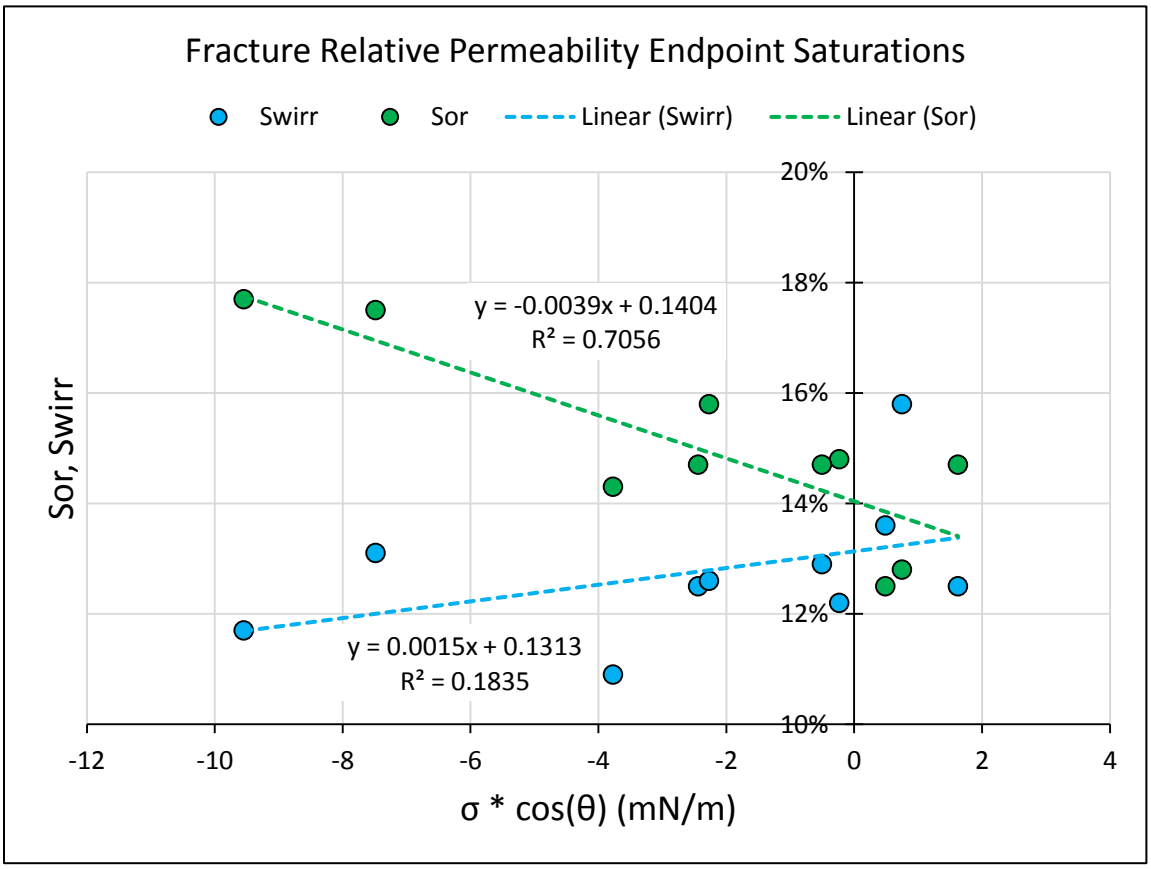

Fig. 5.1 – Fracture Relative Permeability Endpoint Saturations Plotted as a Function of the Product of Interfacial Tension (σ) and the Cosine of Contact Angle (cos(θ)).

Fracture relative permeability for oil at irreducible water saturation ($k_{ro(S_{wirr})}$) and for water at residual oil saturation ($k_{rw(S_{or})}$) were plotted as a function of the product of the interfacial tension and the cosine of the contact angle ($\sigma * \cos\theta$) as shown in **Fig. 5.2**. In this case, it can be observed that there is a direct linear relationship between the relative permeability for oil at irreducible water saturation ($k_{ro(S_{wirr})}$), and an inverse linear relationship between the relative permeability for water at residual oil saturation ($k_{rw(S_{or})}$), with product of interfacial tension and cosine of contact angle ($\sigma * \cos\theta$) respectively.

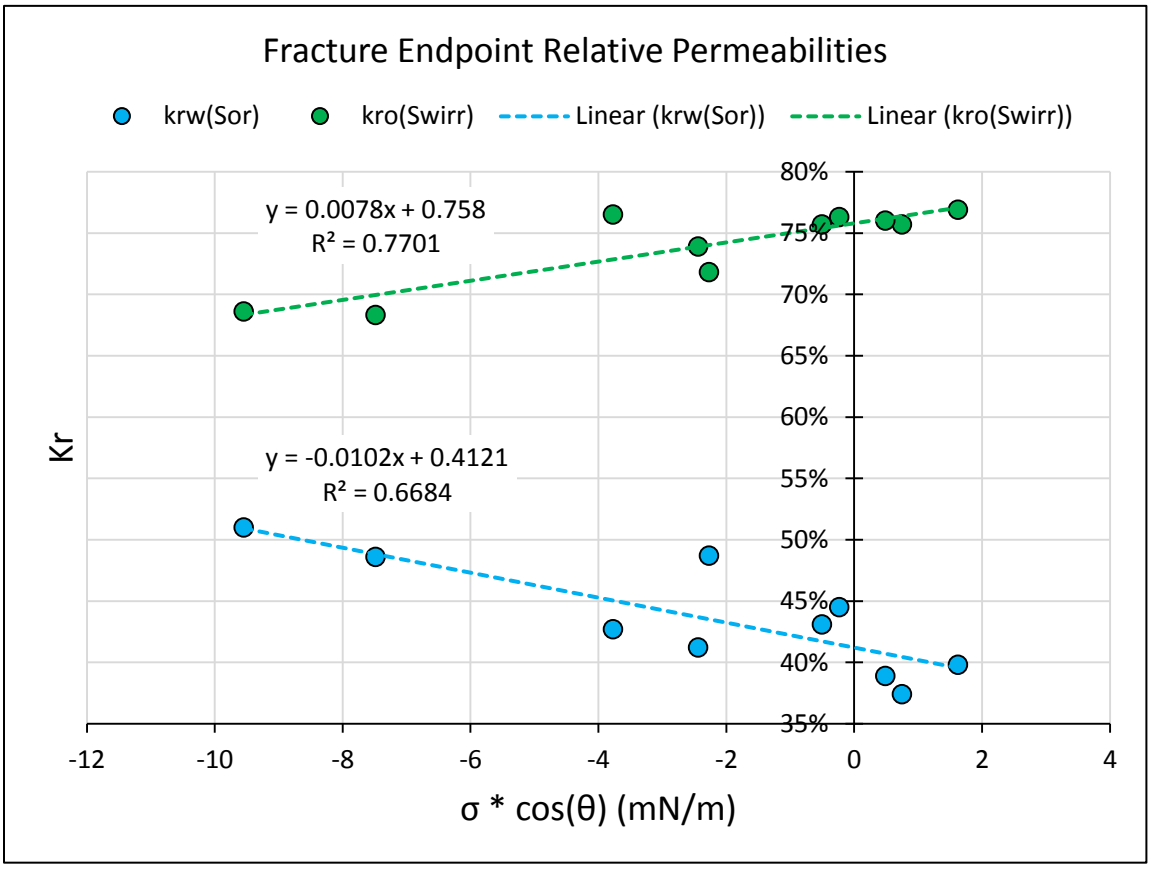

Fig. 5.2 – Fracture Endpoint Relative Permeabilities Plotted as a Function of the Product of Interfacial Tension (σ) and the Cosine of Contact Angle (cos(θ)).

Fracture relative permeability curve crossing points ($S_{w-crossing}$) were plotted as a function of the product of the interfacial tension and the cosine of the contact angle ($\sigma * \cos\theta$) as shown in **Fig. 5.3**. It can be observed that there is a direct linear relationship between the relative permeability crossing points and the product of interfacial tension and cosine of contact angle ($\sigma * \cos\theta$).

In summary, given the trends observed in this section and shown in **Figs. 5.1**, **5.2**, and **5.3**, maximizing the value of the product of interfacial tension and cosine of contact angle ($\sigma * \cos\theta$) will lead to a more water wet system ($S_{w-crossing} > 50\%$).

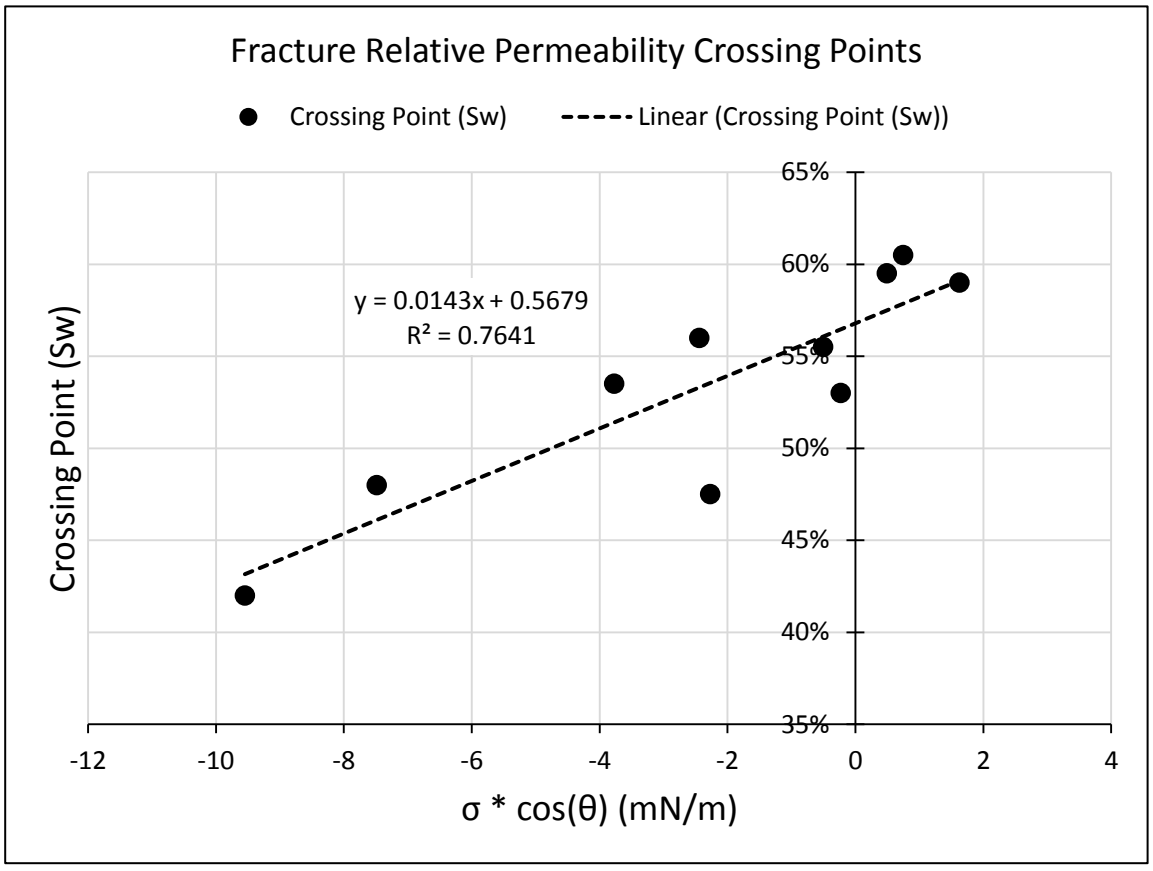

Fig. 5.3 – Fracture Relative Permeability Crossing Points (Sw) Plotted as a Function of the Product of Interfacial Tension and the Cosine of Contact Angle (σ *cos(θ)).

5.3 Surfactant Effects on Simulated Oil Production

The numerical reservoir simulations were conducted for each combination of quartz rich samples, carbonate rich samples, and brine with or without surfactants (no-surfactant, Surf. A, Surf. B, Surf. C, and Surf. D). The numerical reservoir simulation results presented in this summary section are presented as an average of both quartz rich and carbonate rich results in order to present a more complete picture of the potential performance benefits of each respective surfactant additive and its relationship to increased simulated cumulative oil production as well as increased simulated initial oil production across both types of mineralogy sets.

A summary of the simulated 500 day cumulative oil production data is tabulated in **Table 5.2**. The relative increase in cumulative oil production with respect to a No-Surfactant case is tabulated in **Table 5.2** and **Fig. 5.4**.

A summary of the simulated 500 day oil production rate data is tabulated in **Table 5.3**. The relative increase in oil production rate with respect to a No-Surfactant case is tabulated in **Table 5.3** and **Fig. 5.5**.

It can be observed from both the average cumulative oil production data as well as the average oil production rate data that the surfactant additives' performance indicate that Surf. A and Surf. B have an average improvement of about 11% in cumulative oil production, while Surf. C and Surf. D have an improvement around 16%. Similarly, Surf. A and Surf. B show an improvement in peak oil production rate around 25%, while Suf. C and Surf. D showed an improvement around 36%.

Table 5.2 – Summary of Numerical Reservoir Simulation Cumulative Oil Production

SIMULATED CUMULATIVE OIL PRODUCTION DATA SUMMARY					
Source	**Surfactant**	**500 Day Cum Oil Production (STB)**	**Δ 500 Day Cum Oil Production**	**Δ 500 Day Cum Oil Production (Average)**	**Δ 500 Day Cum Oil Production (Std. Dev.)**
TAMU Study	Frac Water - QR	0.6389	0.00%	0.00%	0.00%
TAMU Study	Frac Water - CR	0.6098	0.00%		
TAMU Study	Surf. A - QR	0.7001	9.59%	11.30%	2.42%
TAMU Study	Surf. A - CR	0.6891	13.01%		
TAMU Study	Surf. B - QR	0.7200	12.70%	11.75%	1.35%
TAMU Study	Surf. B - CR	0.6756	10.80%		
TAMU Study	Surf. C - QR	0.7410	15.99%	16.09%	0.14%
TAMU Study	Surf. C - CR	0.7085	16.18%		
TAMU Study	Surf. D - QR	0.7313	14.47%	16.23%	2.48%
TAMU Study	Surf. D - CR	0.7195	17.98%		

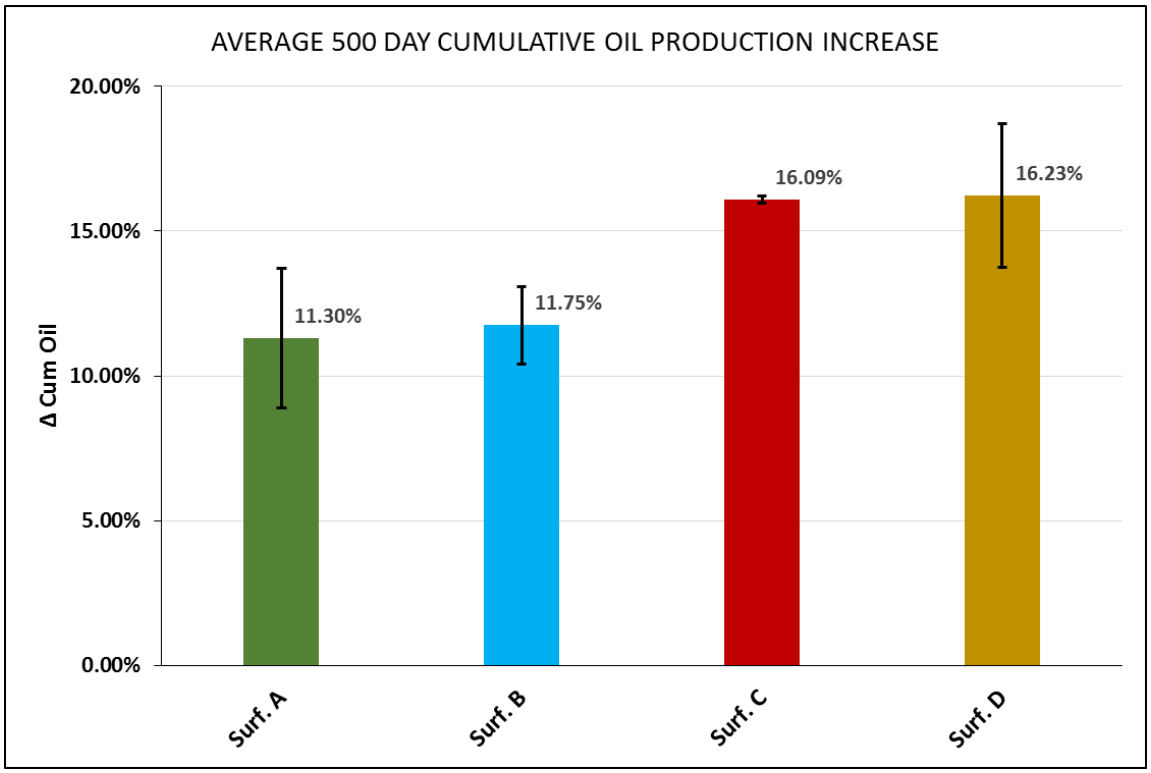

Fig. 5.4 – Average Increase in 500 Day Cumulative Oil Production from Numerical Reservoir Simulations for both Quartz Rich and Carbonate Rich Cases.

Table 5.3 – Summary of Numerical Reservoir Simulation Initial Oil Production Rate

SIMULATED PEAK INITIAL OIL PRODUCTION RATE SUMMARY					
Source	**Surfactant**	**Peak Oil IP (STB/d)**	**Δ Peak Oil IP**	**Δ Peak Oil IP (Average)**	**Δ Peak Oil IP (Std. Dev.)**
TAMU Study	Frac Water - QR	0.0023	0.00%	0.00%	0.00%
TAMU Study	Frac Water - CR	0.0021	0.00%		
TAMU Study	Surf. A - QR	0.0028	21.88%	24.45%	3.64%
TAMU Study	Surf. A - CR	0.0027	27.02%		
TAMU Study	Surf. B - QR	0.0029	27.54%	25.49%	2.91%
TAMU Study	Surf. B - CR	0.0026	23.43%		
TAMU Study	Surf. C - QR	0.0031	35.81%	36.19%	0.53%
TAMU Study	Surf. C - CR	0.0029	36.57%		
TAMU Study	Surf. D - QR	0.0030	31.84%	36.68%	6.85%
TAMU Study	Surf. D - CR	0.0030	41.53%		

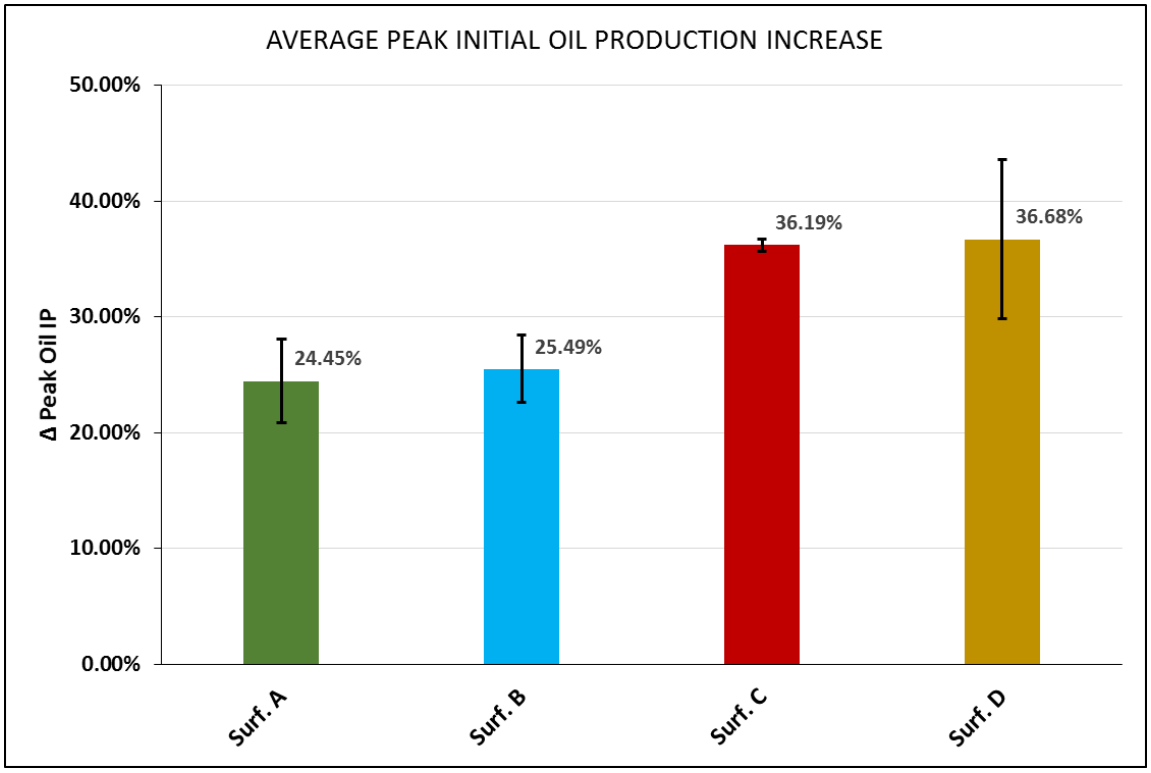

Fig. 5.5 – Average Increase in 500 Day Peak Initial Oil Production Rate from Numerical Reservoir Simulations for both Quartz Rich and Carbonate Rich Cases.

To better understand the relationship between the physical characteristics of the fluid system, the resulting performance metrics from the numerical simulation results (i.e. cumulative production and initial production rate) where plotted as a function of the surfactant properties (i.e. contact angle, interfacial tension, and the product of the two).

The simulated 500-day cumulative oil production and peak oil production rate are plotted as a function of contact angle (θ), as shown in **Fig. 5.6**. It can be observed that a change in wettability leading to a water wet system (decreasing θ) leads to increased cumulative oil production as well as increased oil initial production rate.

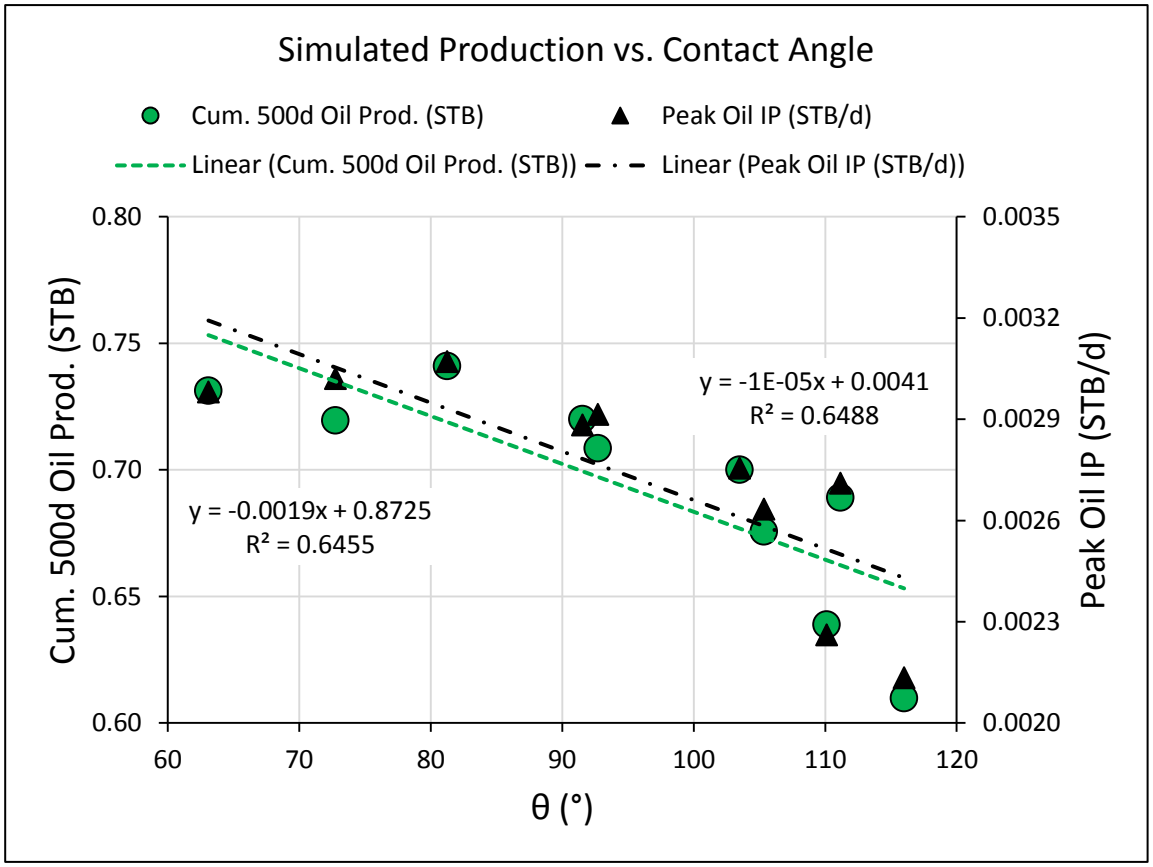

Fig. 5.6 – Simulated 500 Day Cumulative Oil Production and Peak Initial Oil Production Rate Plotted as a Function of Surfactant Contact Angle (θ).

The simulated 500-day cumulative oil production and peak oil production rate are plotted as a function of interfacial tension (σ), as shown in **Fig. 5.7**. Similarly to the relationship with contact angle, it can be observed that a reduction in interfacial tension (decreasing σ) leads to increased cumulative oil production as well as increased oil initial production rate. It is also important to observe the fact that there are four groupings of data points with respect to the interfacial tension values, and this is due to the five systems tested, namely no-surfactant ($\sigma = \sim 22\ mN/m$), Surf. A and Surf. C ($\sigma = \sim 11\ mN/m$), Surf. B ($\sigma = \sim 9\ mN/m$), and Surf. D ($\sigma = \sim 2\ mN/m$).

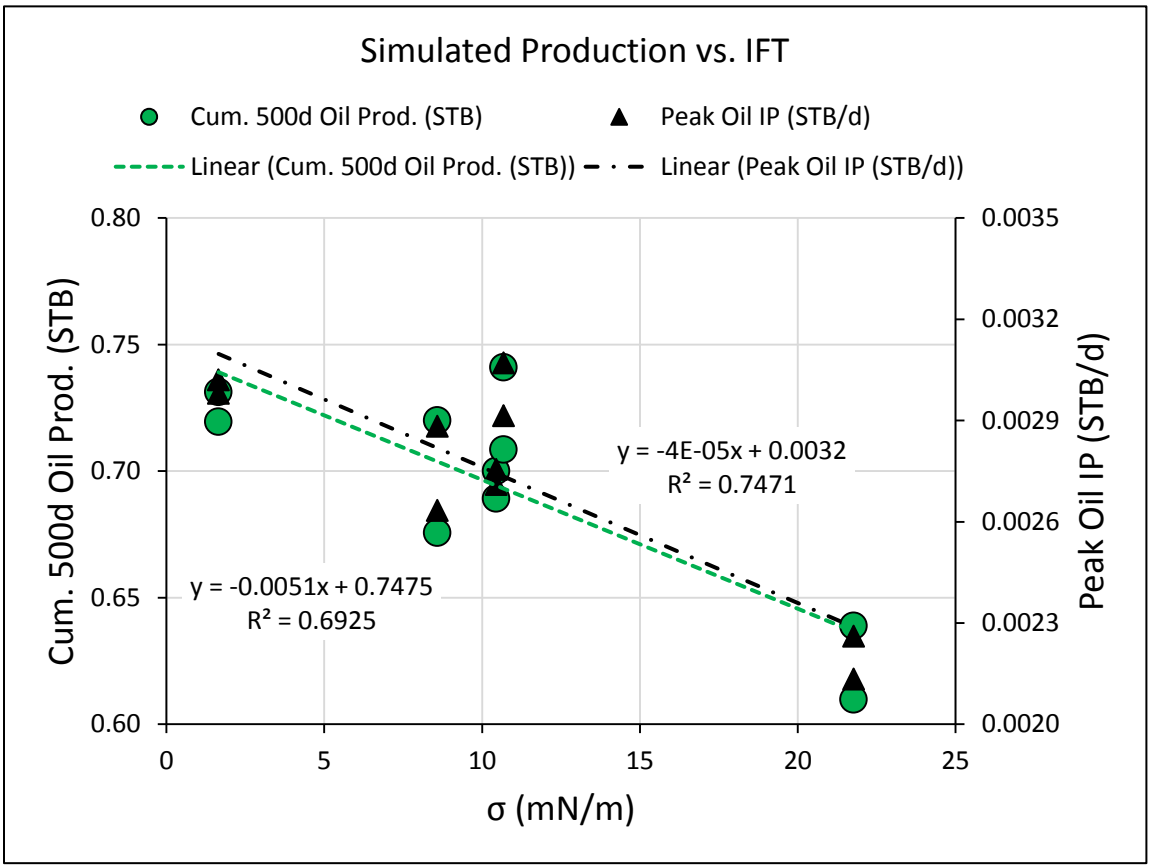

Fig. 5.7 – Simulated 500 Day Cumulative Oil Production and Peak Initial Oil Production Rate Plotted as a Function of Oil-Water-Surfactant Interfacial Tension (σ).

Finally, the simulated 500-day cumulative oil production and peak oil production rate are plotted as a function of the product of interfacial tension and the cosine of contact angle ($\sigma * \cos\theta$), as shown in **Fig. 5.8**. It can clearly be observed that there is a strong correlation between the product of the surfactant systems physical properties and both an increase in cumulative oil production and peak initial oil production rate. The coefficient of determination (R^2 value) between the 500-day cumulative oil production and the peak oil production rate, as a function of the product of interfacial tension and cosine of the contact angle was 0.95 and 0.97 respectively, indicating a high degree of correlation.

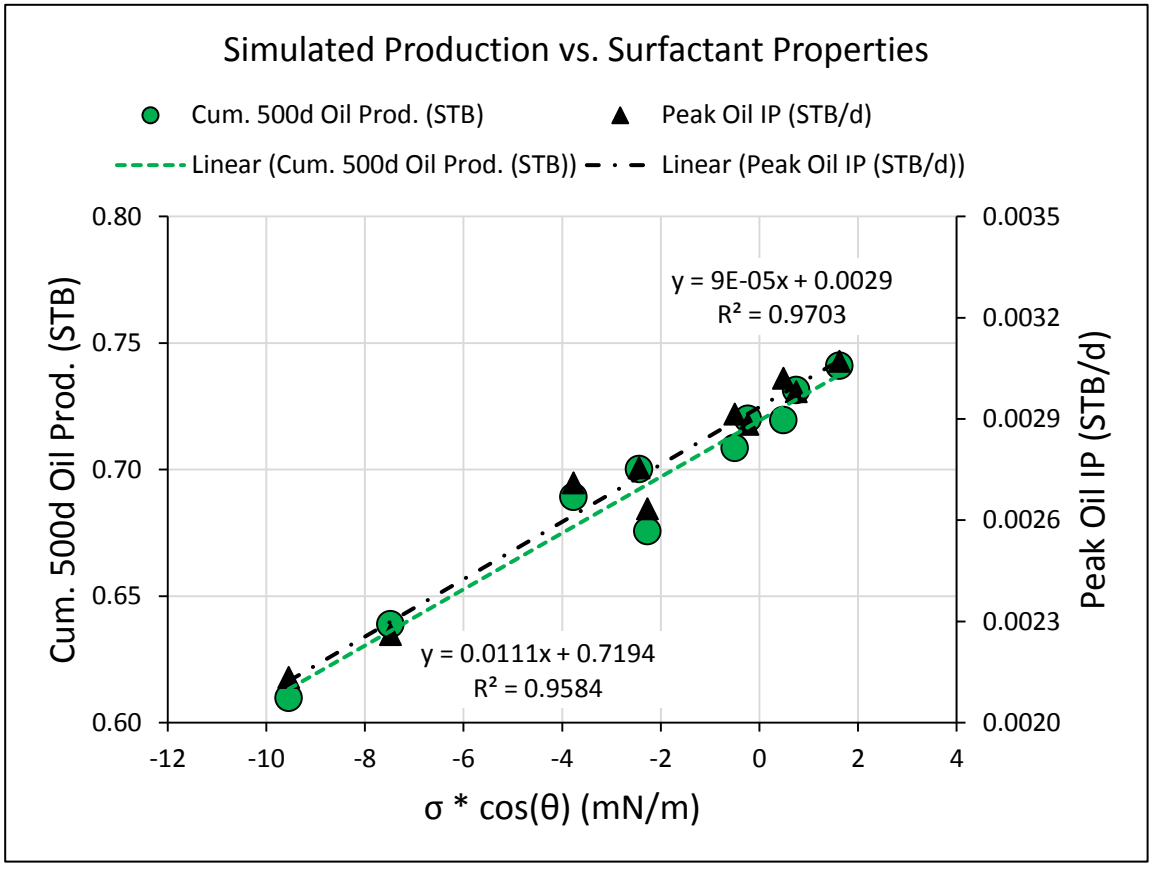

Fig. 5.8 – Simulated 500 Day Cumulative Oil Production and Peak Initial Oil Production Rate Plotted as a Function of the Product of the Oil-Water-Surfactant Interfacial Tension (σ) and Surfactant Contact Angle (θ).

6. CONCLUSIONS AND RECOMMENDATIONS

6.1 Conclusions

Fluid systems with additives that change the wettability of the fracture surface from an oil-wet wettability to a water-wet wettability (decreasing θ) have been shown result in higher oil relative permeability and lower water relative permeability in fractures.

It was also shown that there is a strong relationship between a decreased oil-water interfacial tension (decreasing σ) and favorable oil-water relative permeability behavior in fractures (higher relative permeability to oil and lower relative permeability to water).

This favorable change in the oi-water relative permeability behavior in fractures has also been shown to lead to increased simulated oil production, both cumulative oil production as well as oil initial production rate.

It is important to note that the effects of the contact angle reduction and the interfacial tension reduction should not be considered independently, as each wettability alteration additive presents a unique combination of resulting contact angle reduction and interfacial tension reduction depending on the specific rock type and formation oil to which it is exposed. Therefore, it is important to consider the combined effect of both physical properties in order to analyze the resulting change in oil-water relative permeability in fractures as well as the potential effect of this change on the oil production from any given reservoir. The product of $\sigma * \cos\theta$ was found to have the strongest positive relationship to improving the relative permeability to oil in fractures as well as the strongest positive relationship to improved simulated oil production.

6.2 Recommendations and Future Work

This study was constrained to ten test samples due to core sample availably. It is clear from the mineralogy results from each test sample that there is a large variation in mineralogy between each sample, and this variation in mineralogy will certainly lead to differences in contact angle along the fracture surface. In order to allow for a more robust comparison between surfactant additives, it is recommended that test plugs from same core intervals be used for each surfactant test in order to eliminate any variations in test conditions between each material being evaluated. A comparative study could be conducted using outcrop material if available for the specific formation of interest.

Furthermore, the use of full diameter core (or large outcrop samples) as a test specimen would allow a much larger fracture area to be tested. A larger fracture area would capture a more representative mineralogy distribution as well as fracture roughness characteristics that might have a strong impact on the measurement of the oil-water relative permeability.

It would also be optimal to use preserved core as the test specimen rather than using unpreserved core. Using preserved core would allow direct testing of the core samples under connate wettability conditions rather than having to condition the core in formation oil which could lead to an artificially strongly oil-wet wettability, resulting in potentially exaggerated effects from the surfactant additives.

The final recommendation is to use an aluminum Hassler type core holder in order to be able to CT scan the test specimen during testing, thereby allowing more accurate determination of in-situ fracture saturations.

REFERENCES

Abaci, S., Edwards, J., and Whittaker, B. 1992. Relative Permeability Measurements for Two Phase Flow in Unconsolidated Sands. *Mine water and the environment* **11** (2): 11-26.

Aguilera, R. 1982. Relative Permeability Concepts for Predicting the Performance of Naturally Fractured Reservoirs. *Journal of Canadian Petroleum Technology* **21** (05).

Akin, S. 2001. Estimation of Fracture Relative Permeabilities from Unsteady State Corefloods. *Journal of Petroleum Science and Engineering* **30** (1): 1-14.

Brooks, R.H. and Corey, A.T. 1966. Properties of Porous Media Affecting Fluid Flow. *Journal of the Irrigation and Drainage Division* **92** (2): 61-90.

Darcy, H. 1856. Les Fontaines Publique De La Ville De Dijon. *Dalmont, Paris* **647**.

de la Porte, J.J., Kossack, C.A., and Zimmerman, R.W. 2005. The Effect of Fracture Relative Permeabilities and Capillary Pressures on the Numerical Simulation of Naturally Fractured Reservoirs. In *SPE annual technical conference and exhibition*: Society of Petroleum Engineers.

Diomampo, G., Chen, C.-Y., Li, K., and Horne, R.N. 2001. Relative Permeability through Fractures. In *Proc. 27 th Workshop on Geothermal Reservoir Engineering*:28-30.

Economides, M.J., Hill, A.D., Ehlig-Economides, C., and Zhu, D. 2012. *Petroleum Production Systems*. New Jersey: Pearson Education, Inc. Original edition.

Erarslan, N. and Williams, D.J. 2012. Experimental, Numerical and Analytical Studies on Tensile Strength of Rocks. *International Journal of Rock Mechanics and Mining Sciences* **49**: 21-30.

Gilman, J.R. and Kazemi, H. 1983. Improvements in Simulation of Naturally Fractured Reservoirs. *Society of Petroleum Engineers Journal* **23** (04): 695-707.

Glover, P. 2010. Relative Permeability. In *Formation Evaluation Msc Course Notes*.

Honarpour, M. and Mahmood, S. 1988. Relative-Permeability Measurements: An Overview. *Journal of petroleum technology* **40** (08): 963-966.

Huo, D. and Benson, S.M. 2016. Experimental Investigation of Stress-Dependency of Relative Permeability in Rock Fractures. *Transport in Porous Media*: 1-24.

Izadi, M., Shadizadeh, S.R., and Moradi, S. 2012. Experimentally Measurements of Relative Permeability in Fractured Core. *International Journal of Science & Emerging Technologies* **3** (2).

Johnson, E., Bossler, D., and Naumann, V. 1959. Calculation of Relative Permeability from Displacement Experiments. *PETROLEUM TRANSACTIONS, AIME* **216**: 370-372.

Kasiri, N. 2011. Fracture Relative Permeability Revisited. *World oil* **232** (10).

Morris, J. and Pyrak-Nolte, L. 1999. Fracture Network Geometry and Relative Permeability. In *Vail Rocks 1999, The 37th US Symposium on Rock Mechanics (USRMS)*: American Rock Mechanics Association.

Mungan, N. 1972. Relative Permeability Measurements Using Reservoir Fluids. *Society of Petroleum Engineers Journal* **12** (05): 398-402.

Muskat, M., Wyckoff, R., Botset, H., and Meres, M. 1937. Flow of Gas-Liquid Mixtures through Sands. *Transactions of the AIME* **123** (01): 69-96.

Pan, X., Wong, R., and Maini, B. 1996. Steady State Two-Phase in a Smooth Parallel Fracture. In *Annual Technical Meeting*: Petroleum Society of Canada.

Pieters, D. and Graves, R. 1994. Fracture Relative Permeability: Linear or Non-Linear Function of Saturation. In *International Petroleum Conference and Exhibition of Mexico*: Society of Petroleum Engineers.

Richardson, J., Kerver, J., Hafford, J., and Osoba, J. 1952. Laboratory Determination of Relative Permeability. *Journal of Petroleum Technology* **4** (08): 187-196.

Romm, E. 1966. Flow Characteristics of Fractured Rocks. *Nedra, Moscow* **283**.

Rossen, W. and Kumar, A.T. 1992. Single-and Two-Phase Flow in Natural Fractures. In *SPE Annual Technical Conference and Exhibition*: Society of Petroleum Engineers.

Sakurai, K., Watanabe, N., Ishibashi, T., Tsuchiya, N., Ohsaki, Y., Tamagawa, T., and Yagi, M. 2013. Oil-Water Relative Permeability Curves for Fractures in Granite and Limestone at Different Intrinsic Permeabilities. In *19th Formation Evaluation Symposium of Japan*: Society of Petrophysicists and Well-Log Analysts.

Speyer, N., Li, K., and Home, R. 2007. Experimental Measurement of Two-Phase Relative Permeability in Vertical Fractures. Paper presented at the Thirty-Second Workshop on Geothermal Reservoir Engineering Stanford University, Stanford, California, January 22-24, 2007. DOI: SGP-TR-183.

Tsang, Y. 1989. On Two-Phase Relative Permeability and Capillary Pressure of Rough-Walled Rock Fractures. *Lawrence Berkeley National Laboratory*.

Welge, H.J. 1952. A Simplified Method for Computing Oil Recovery by Gas or Water Drive. DOI: 10.2118/124-G

White, F.M. 2011. *Fluid Mechanics*: McGraw Hill. Original edition.

APPENDIX

Table A.1 – Summary of Generalized Brooks-Corey correlation Endpoint and Corey Exponent Values for Oil-Water Relative Permeability Curves in Fractures.

	Corey Model Summary for All Cases							
	Quartz Rich Core				Carbonate Rich Core			
No-Surfactant	Kro		Krw		Kro		Krw	
	$K_{ro\text{-}Swmin}$	1.000	$K_{rw\text{-}Sorw}$	0.486	$K_{ro\text{-}Swmin}$	1.000	$K_{rw\text{-}Sorw}$	0.509
	$S_{w\,max}$	1.000	$S_{w\,max}$	1.000	$S_{w\,max}$	1.000	$S_{w\,max}$	1.000
	S_{orw}	0.175	S_{orw}	0.175	S_{orw}	1.000	S_{orw}	1.000
	S_{wi}	0.000	S_{wcr}	0.131	S_{wi}	0.000	S_{wcr}	0.110
	C_o	2.200	C_w	1.720	C_o	2.450	C_w	1.300
Surf. A	Kro		Krw		Kro		Krw	
	$K_{ro\text{-}Swmin}$	1.000	$K_{rw\text{-}Sorw}$	0.411	$K_{ro\text{-}Swmin}$	1.000	$K_{rw\text{-}Sorw}$	0.426
	$S_{w\,max}$	1.000	$S_{w\,max}$	1.000	$S_{w\,max}$	1.000	$S_{w\,max}$	1.000
	S_{orw}	0.147	S_{orw}	0.147	S_{orw}	0.143	S_{orw}	0.143
	S_{wi}	0.000	S_{wcr}	0.134	S_{wi}	0.000	S_{wcr}	0.110
	C_o	1.800	C_w	2.000	C_o	1.900	C_w	1.800
Surf. B	Kro		Krw		Kro		Krw	
	$K_{ro\text{-}Swmin}$	1.000	$K_{rw\text{-}Sorw}$	0.446	$K_{ro\text{-}Swmin}$	1.000	$K_{rw\text{-}Sorw}$	0.485
	$S_{w\,max}$	1.000	$S_{w\,max}$	1.000	$S_{w\,max}$	1.000	$S_{w\,max}$	1.000
	S_{orw}	0.148	S_{orw}	0.148	S_{orw}	0.158	S_{orw}	0.158
	S_{wi}	0.000	S_{wcr}	0.115	S_{wi}	0.000	S_{wcr}	0.115
	C_o	1.900	C_w	1.800	C_o	2.200	C_w	1.600
Surf. C	Kro		Krw		Kro		Krw	
	$K_{ro\text{-}Swmin}$	1.000	$K_{rw\text{-}Sorw}$	0.399	$K_{ro\text{-}Swmin}$	1.000	$K_{rw\text{-}Sorw}$	0.432
	$S_{w\,max}$	1.000	$S_{w\,max}$	1.000	$S_{w\,max}$	1.000	$S_{w\,max}$	1.000
	S_{orw}	0.147	S_{orw}	0.147	S_{orw}	0.147	S_{orw}	0.147
	S_{wi}	0.000	S_{wcr}	0.134	S_{wi}	0.000	S_{wcr}	0.131
	C_o	1.550	C_w	2.000	C_o	1.700	C_w	1.800
Surf. D	Kro		Krw		Kro		Krw	
	$K_{ro\text{-}Swmin}$	1.000	$K_{rw\text{-}Sorw}$	0.373	$K_{ro\text{-}Swmin}$	1.000	$K_{rw\text{-}Sorw}$	0.389
	$S_{w\,max}$	1.000	$S_{w\,max}$	1.000	$S_{w\,max}$	1.000	$S_{w\,max}$	1.000
	S_{orw}	0.128	S_{orw}	0.128	S_{orw}	0.125	S_{orw}	0.125
	S_{wi}	0.000	S_{wcr}	0.147	S_{wi}	0.000	S_{wcr}	0.141
	C_o	1.550	C_w	1.800	C_o	1.560	C_w	1.750

Table A.2 – Relative Permeability Table for No Surfactant Quartz Rich Case

No Surf (QR)		
Swat	**Krw**	**Krow**
0.1310	0.0000	0.6828
0.1452	0.0006	0.6533
0.1593	0.0020	0.6237
0.1735	0.0040	0.5949
0.1877	0.0065	0.5668
0.2018	0.0096	0.5395
0.2160	0.0131	0.5129
0.2301	0.0171	0.4870
0.2443	0.0215	0.4618
0.2585	0.0263	0.4374
0.2726	0.0316	0.4137
0.2868	0.0372	0.3907
0.3010	0.0432	0.3685
0.3151	0.0496	0.3469
0.3293	0.0563	0.3261
0.3434	0.0634	0.3059
0.3576	0.0708	0.2865
0.3718	0.0786	0.2677
0.3859	0.0868	0.2497
0.4001	0.0952	0.2323
0.4143	0.1040	0.2156
0.4284	0.1131	0.1996
0.4426	0.1225	0.1842
0.4568	0.1323	0.1696
0.4709	0.1423	0.1555
0.4851	0.1527	0.1422
0.4992	0.1633	0.1295
0.5134	0.1743	0.1174
0.5276	0.1855	0.1060
0.5417	0.1970	0.0952
0.5559	0.2089	0.0850
0.5701	0.2210	0.0755
0.5842	0.2334	0.0666
0.5984	0.2461	0.0583
0.6126	0.2591	0.0506
0.6267	0.2723	0.0434
0.6409	0.2858	0.0369
0.6550	0.2996	0.0309
0.6692	0.3137	0.0256
0.6834	0.3280	0.0207
0.6975	0.3426	0.0164
0.7117	0.3575	0.0127
0.7259	0.3726	0.0095
0.7400	0.3880	0.0067
0.7542	0.4036	0.0045
0.7683	0.4195	0.0028
0.7825	0.4357	0.0015
0.7967	0.4521	0.0006
0.8108	0.4688	0.0001
0.8250	0.4857	0.0000

Table A.3 – Relative Permeability Table for No Surfactant Carbonate Rich Case

No Surf (CR)		
Swat	**Krw**	**Krow**
0.1170	0.0000	0.6863
0.1314	0.0053	0.6530
0.1458	0.0104	0.6202
0.1602	0.0162	0.5883
0.1746	0.0225	0.5575
0.1890	0.0292	0.5276
0.2034	0.0363	0.4987
0.2179	0.0437	0.4708
0.2323	0.0515	0.4438
0.2467	0.0595	0.4177
0.2611	0.0678	0.3926
0.2755	0.0763	0.3684
0.2899	0.0850	0.3451
0.3043	0.0940	0.3227
0.3187	0.1032	0.3012
0.3331	0.1125	0.2805
0.3475	0.1221	0.2607
0.3619	0.1318	0.2418
0.3763	0.1416	0.2237
0.3908	0.1517	0.2064
0.4052	0.1619	0.1900
0.4196	0.1722	0.1743
0.4340	0.1827	0.1595
0.4484	0.1934	0.1454
0.4628	0.2041	0.1321
0.4772	0.2150	0.1195
0.4916	0.2261	0.1077
0.5060	0.2372	0.0966
0.5204	0.2485	0.0862
0.5348	0.2599	0.0765
0.5492	0.2714	0.0674
0.5637	0.2830	0.0591
0.5781	0.2948	0.0513
0.5925	0.3066	0.0443
0.6069	0.3186	0.0378
0.6213	0.3307	0.0319
0.6357	0.3428	0.0266
0.6501	0.3551	0.0219
0.6645	0.3675	0.0177
0.6789	0.3799	0.0140
0.6933	0.3925	0.0108
0.7077	0.4051	0.0081
0.7221	0.4179	0.0058
0.7366	0.4307	0.0040
0.7510	0.4436	0.0026
0.7654	0.4566	0.0015
0.7798	0.4697	0.0007
0.7942	0.4829	0.0003
0.8086	0.4961	0.0000
0.8230	0.5104	0.0000

Table A.4 – Relative Permeability Table for Surf. A Quartz Rich Case

Surf. A (QR)		
Swat	**Krw**	**Krow**
0.1250	0.0000	0.7391
0.1399	0.0000	0.7245
0.1547	0.0003	0.6975
0.1696	0.0010	0.6710
0.1844	0.0020	0.6450
0.1993	0.0034	0.6194
0.2141	0.0051	0.5943
0.2290	0.0072	0.5697
0.2439	0.0096	0.5455
0.2587	0.0124	0.5218
0.2736	0.0155	0.4985
0.2884	0.0189	0.4758
0.3033	0.0228	0.4535
0.3181	0.0269	0.4316
0.3330	0.0315	0.4103
0.3479	0.0363	0.3894
0.3627	0.0415	0.3691
0.3776	0.0471	0.3492
0.3924	0.0530	0.3298
0.4073	0.0593	0.3109
0.4221	0.0659	0.2925
0.4370	0.0729	0.2746
0.4519	0.0802	0.2572
0.4667	0.0879	0.2403
0.4816	0.0959	0.2239
0.4964	0.1043	0.2080
0.5113	0.1131	0.1927
0.5261	0.1221	0.1779
0.5410	0.1316	0.1636
0.5559	0.1413	0.1498
0.5707	0.1515	0.1366
0.5856	0.1620	0.1240
0.6004	0.1728	0.1118
0.6153	0.1840	0.1003
0.6301	0.1955	0.0893
0.6450	0.2074	0.0789
0.6599	0.2196	0.0690
0.6747	0.2322	0.0597
0.6896	0.2451	0.0511
0.7044	0.2584	0.0430
0.7193	0.2721	0.0356
0.7341	0.2861	0.0288
0.7490	0.3004	0.0226
0.7639	0.3151	0.0172
0.7787	0.3301	0.0124
0.7936	0.3455	0.0083
0.8084	0.3613	0.0049
0.8233	0.3773	0.0024
0.8381	0.3938	0.0007
0.8530	0.4115	0.0000

Table A.5 – Relative Permeability Table for Surf. A Carbonate Rich Case

Surf. A (CR)		
Swat	**Krw**	**Krow**
0.1090	0.0000	0.7648
0.1243	0.0003	0.7426
0.1395	0.0013	0.7134
0.1548	0.0027	0.6849
0.1701	0.0046	0.6569
0.1853	0.0069	0.6294
0.2006	0.0096	0.6025
0.2159	0.0127	0.5762
0.2311	0.0161	0.5504
0.2464	0.0200	0.5252
0.2617	0.0242	0.5005
0.2769	0.0287	0.4764
0.2922	0.0336	0.4529
0.3074	0.0389	0.4299
0.3227	0.0445	0.4075
0.3380	0.0504	0.3856
0.3532	0.0566	0.3644
0.3685	0.0631	0.3437
0.3838	0.0700	0.3236
0.3990	0.0772	0.3040
0.4143	0.0847	0.2851
0.4296	0.0925	0.2667
0.4448	0.1006	0.2489
0.4601	0.1090	0.2316
0.4754	0.1177	0.2150
0.4906	0.1267	0.1990
0.5059	0.1360	0.1835
0.5212	0.1456	0.1686
0.5364	0.1555	0.1544
0.5517	0.1656	0.1407
0.5670	0.1761	0.1276
0.5822	0.1868	0.1152
0.5975	0.1978	0.1033
0.6128	0.2091	0.0921
0.6280	0.2206	0.0815
0.6433	0.2325	0.0715
0.6586	0.2446	0.0621
0.6738	0.2570	0.0533
0.6891	0.2697	0.0452
0.7043	0.2826	0.0377
0.7196	0.2958	0.0309
0.7349	0.3092	0.0247
0.7501	0.3230	0.0191
0.7654	0.3370	0.0143
0.7807	0.3512	0.0101
0.7959	0.3658	0.0066
0.8112	0.3805	0.0038
0.8265	0.3956	0.0018
0.8417	0.4109	0.0005
0.8570	0.4269	0.0000

Table A.6 – Relative Permeability Table for Surf. B Quartz Rich Case

Surf. B (QR)		
Swat	**Krw**	**Krow**
0.1220	0.0000	0.7631
0.1369	0.0008	0.7169
0.1518	0.0020	0.6888
0.1667	0.0037	0.6612
0.1816	0.0059	0.6342
0.1965	0.0085	0.6077
0.2114	0.0114	0.5817
0.2263	0.0148	0.5563
0.2412	0.0186	0.5314
0.2561	0.0227	0.5070
0.2710	0.0272	0.4832
0.2859	0.0321	0.4599
0.3008	0.0373	0.4372
0.3157	0.0428	0.4150
0.3306	0.0487	0.3934
0.3455	0.0550	0.3723
0.3604	0.0615	0.3518
0.3753	0.0684	0.3318
0.3902	0.0756	0.3124
0.4051	0.0832	0.2935
0.4200	0.0910	0.2752
0.4349	0.0992	0.2575
0.4498	0.1076	0.2403
0.4647	0.1164	0.2236
0.4796	0.1255	0.2076
0.4944	0.1349	0.1921
0.5093	0.1445	0.1772
0.5242	0.1545	0.1628
0.5391	0.1648	0.1490
0.5540	0.1754	0.1359
0.5689	0.1862	0.1232
0.5838	0.1974	0.1112
0.5987	0.2088	0.0998
0.6136	0.2205	0.0889
0.6285	0.2325	0.0786
0.6434	0.2448	0.0690
0.6583	0.2574	0.0599
0.6732	0.2702	0.0515
0.6881	0.2833	0.0436
0.7030	0.2967	0.0364
0.7179	0.3104	0.0298
0.7328	0.3243	0.0238
0.7477	0.3385	0.0185
0.7626	0.3530	0.0138
0.7775	0.3678	0.0098
0.7924	0.3828	0.0064
0.8073	0.3981	0.0037
0.8222	0.4136	0.0017
0.8371	0.4294	0.0005
0.8520	0.4455	0.0000

Table A.7 – Relative Permeability Table for Surf. B Carbonate Rich Case

Surf. B (CR)		
Swat	**Krw**	**Krow**
0.1260	0.0000	0.7176
0.1406	0.0023	0.6690
0.1552	0.0047	0.6387
0.1698	0.0078	0.6092
0.1844	0.0113	0.5804
0.1991	0.0154	0.5524
0.2137	0.0199	0.5252
0.2283	0.0248	0.4987
0.2429	0.0301	0.4729
0.2575	0.0358	0.4479
0.2721	0.0418	0.4237
0.2867	0.0482	0.4001
0.3013	0.0550	0.3773
0.3160	0.0620	0.3553
0.3306	0.0694	0.3339
0.3452	0.0771	0.3133
0.3598	0.0850	0.2934
0.3744	0.0933	0.2742
0.3890	0.1019	0.2557
0.4036	0.1107	0.2379
0.4182	0.1198	0.2208
0.4329	0.1292	0.2044
0.4475	0.1388	0.1887
0.4621	0.1487	0.1736
0.4767	0.1588	0.1593
0.4913	0.1692	0.1456
0.5059	0.1798	0.1326
0.5205	0.1907	0.1202
0.5351	0.2018	0.1085
0.5498	0.2132	0.0975
0.5644	0.2248	0.0871
0.5790	0.2366	0.0773
0.5936	0.2486	0.0682
0.6082	0.2609	0.0597
0.6228	0.2733	0.0518
0.6374	0.2860	0.0445
0.6520	0.2989	0.0378
0.6667	0.3121	0.0317
0.6813	0.3254	0.0262
0.6959	0.3389	0.0212
0.7105	0.3527	0.0168
0.7251	0.3666	0.0130
0.7397	0.3808	0.0097
0.7543	0.3951	0.0069
0.7689	0.4097	0.0046
0.7836	0.4244	0.0028
0.7982	0.4393	0.0015
0.8128	0.4545	0.0006
0.8274	0.4698	0.0001
0.8420	0.4874	0.0000

Table A.8 – Relative Permeability Table for Surf. C Quartz Rich Case

Surf. C (QR)		
Swat	**Krw**	**Krow**
0.1250	0.0000	0.7689
0.1399	0.0000	0.7576
0.1547	0.0003	0.7333
0.1696	0.0010	0.7093
0.1844	0.0020	0.6855
0.1993	0.0033	0.6620
0.2141	0.0050	0.6389
0.2290	0.0070	0.6160
0.2439	0.0093	0.5934
0.2587	0.0120	0.5711
0.2736	0.0151	0.5491
0.2884	0.0184	0.5275
0.3033	0.0221	0.5061
0.3181	0.0262	0.4851
0.3330	0.0306	0.4643
0.3479	0.0353	0.4439
0.3627	0.0404	0.4239
0.3776	0.0458	0.4041
0.3924	0.0516	0.3847
0.4073	0.0577	0.3657
0.4221	0.0642	0.3469
0.4370	0.0709	0.3286
0.4519	0.0781	0.3106
0.4667	0.0855	0.2929
0.4816	0.0933	0.2756
0.4964	0.1015	0.2587
0.5113	0.1100	0.2422
0.5261	0.1188	0.2261
0.5410	0.1280	0.2104
0.5559	0.1375	0.1950
0.5707	0.1474	0.1801
0.5856	0.1576	0.1657
0.6004	0.1681	0.1516
0.6153	0.1790	0.1380
0.6301	0.1902	0.1249
0.6450	0.2018	0.1122
0.6599	0.2137	0.1000
0.6747	0.2259	0.0884
0.6896	0.2385	0.0772
0.7044	0.2514	0.0666
0.7193	0.2647	0.0566
0.7341	0.2783	0.0471
0.7490	0.2923	0.0383
0.7639	0.3065	0.0302
0.7787	0.3212	0.0227
0.7936	0.3362	0.0161
0.8084	0.3515	0.0103
0.8233	0.3671	0.0055
0.8381	0.3831	0.0019
0.8530	0.3978	0.0000

Table A.9 – Relative Permeability Table for Surf. C Carbonate Rich Case

Surf. C (CR)		
Swat	**Krw**	**Krow**
0.1290	0.0000	0.7570
0.1438	0.0003	0.7307
0.1586	0.0012	0.7050
0.1733	0.0026	0.6797
0.1881	0.0045	0.6547
0.2029	0.0068	0.6302
0.2177	0.0095	0.6060
0.2324	0.0126	0.5823
0.2472	0.0161	0.5589
0.2620	0.0200	0.5359
0.2768	0.0242	0.5134
0.2915	0.0288	0.4912
0.3063	0.0338	0.4694
0.3211	0.0391	0.4480
0.3359	0.0447	0.4271
0.3506	0.0507	0.4066
0.3654	0.0570	0.3864
0.3802	0.0636	0.3667
0.3950	0.0706	0.3475
0.4097	0.0779	0.3286
0.4245	0.0854	0.3102
0.4393	0.0933	0.2923
0.4541	0.1016	0.2747
0.4688	0.1101	0.2577
0.4836	0.1189	0.2410
0.4984	0.1280	0.2249
0.5132	0.1374	0.2092
0.5279	0.1471	0.1940
0.5427	0.1571	0.1792
0.5575	0.1674	0.1650
0.5723	0.1780	0.1512
0.5870	0.1889	0.1379
0.6018	0.2000	0.1251
0.6166	0.2115	0.1129
0.6314	0.2232	0.1011
0.6461	0.2352	0.0900
0.6609	0.2475	0.0793
0.6757	0.2601	0.0692
0.6905	0.2729	0.0597
0.7052	0.2860	0.0508
0.7200	0.2994	0.0424
0.7348	0.3130	0.0347
0.7496	0.3270	0.0277
0.7643	0.3411	0.0213
0.7791	0.3556	0.0156
0.7939	0.3703	0.0107
0.8087	0.3853	0.0066
0.8234	0.4006	0.0033
0.8382	0.4161	0.0010
0.8530	0.4312	0.0000

Table A.10 – Relative Permeability Table for Surf. D Quartz Rich Case

Surf. D (QR)		
Swat	**Krw**	**Krow**
0.1580	0.0000	0.7570
0.1726	0.0009	0.7105
0.1871	0.0020	0.6877
0.2017	0.0036	0.6651
0.2163	0.0054	0.6428
0.2309	0.0077	0.6208
0.2454	0.0102	0.5991
0.2600	0.0131	0.5776
0.2746	0.0163	0.5565
0.2891	0.0198	0.5356
0.3037	0.0236	0.5150
0.3183	0.0278	0.4946
0.3329	0.0321	0.4746
0.3474	0.0368	0.4549
0.3620	0.0418	0.4354
0.3766	0.0470	0.4163
0.3911	0.0525	0.3975
0.4057	0.0583	0.3790
0.4203	0.0643	0.3608
0.4349	0.0707	0.3429
0.4494	0.0772	0.3253
0.4640	0.0841	0.3081
0.4786	0.0911	0.2912
0.4931	0.0985	0.2747
0.5077	0.1061	0.2585
0.5223	0.1139	0.2426
0.5369	0.1220	0.2271
0.5514	0.1303	0.2120
0.5660	0.1389	0.1973
0.5806	0.1477	0.1829
0.5951	0.1567	0.1689
0.6097	0.1660	0.1553
0.6243	0.1756	0.1422
0.6389	0.1853	0.1294
0.6534	0.1953	0.1171
0.6680	0.2056	0.1052
0.6826	0.2160	0.0938
0.6971	0.2267	0.0829
0.7117	0.2376	0.0724
0.7263	0.2488	0.0625
0.7409	0.2602	0.0531
0.7554	0.2718	0.0442
0.7700	0.2836	0.0359
0.7846	0.2957	0.0283
0.7991	0.3079	0.0213
0.8137	0.3204	0.0151
0.8283	0.3331	0.0097
0.8429	0.3461	0.0052
0.8574	0.3592	0.0018
0.8720	0.3740	0.0000

Table A.11 – Relative Permeability Table for Surf. D Carbonate Rich Case

Surf. D (CR)		
Swat	**Krw**	**Krow**
0.1360	0.0000	0.7597
0.1511	0.0002	0.7440
0.1662	0.0011	0.7200
0.1812	0.0024	0.6962
0.1963	0.0042	0.6728
0.2114	0.0064	0.6496
0.2265	0.0090	0.6267
0.2416	0.0120	0.6041
0.2567	0.0153	0.5818
0.2717	0.0190	0.5598
0.2868	0.0230	0.5382
0.3019	0.0273	0.5168
0.3170	0.0319	0.4957
0.3321	0.0369	0.4750
0.3471	0.0421	0.4546
0.3622	0.0476	0.4345
0.3773	0.0535	0.4147
0.3924	0.0596	0.3953
0.4075	0.0660	0.3762
0.4226	0.0726	0.3574
0.4376	0.0796	0.3390
0.4527	0.0868	0.3209
0.4678	0.0943	0.3032
0.4829	0.1020	0.2859
0.4980	0.1100	0.2689
0.5130	0.1183	0.2523
0.5281	0.1268	0.2361
0.5432	0.1356	0.2203
0.5583	0.1446	0.2049
0.5734	0.1539	0.1899
0.5884	0.1634	0.1753
0.6035	0.1732	0.1611
0.6186	0.1832	0.1473
0.6337	0.1934	0.1341
0.6488	0.2039	0.1212
0.6639	0.2146	0.1088
0.6789	0.2255	0.0970
0.6940	0.2367	0.0856
0.7091	0.2481	0.0747
0.7242	0.2598	0.0644
0.7393	0.2716	0.0546
0.7543	0.2837	0.0455
0.7694	0.2961	0.0369
0.7845	0.3086	0.0290
0.7996	0.3214	0.0218
0.8147	0.3344	0.0154
0.8298	0.3476	0.0098
0.8448	0.3610	0.0052
0.8599	0.3746	0.0018
0.8750	0.3885	0.0000